THE UNIVERSITY OF CHICAGO

COHERENCE OF SPIN QUBITS AND SIMULATION OF SPIN-OPTO-MECHANICAL DEVICE MODES IN SILICON CARBIDE

A DISSERTATION SUBMITTED TO

THE FACULTY OF THE DIVISION OF THE PHYSICAL SCIENCES

IN CANDIDACY FOR THE DEGREE OF

DOCTOR OF PHILOSOPHY

DEPARTMENT OF PHYSICS

BY

JOSEPH PARKER BLANTON

CHICAGO, ILLINOIS

MARCH 2025

Table of Contents

List of Figures

Acknowledgments

I would like to recognize the support and contributions from those that helped me along the way towards creating this thesis and completing the work presented herein.

I want to thank my advisor, David Awschalom, for providing me the opportunity to work in his laboratory and providing unparalleled guidance and perspective at all stages of my Ph.D. journey here at the University of Chicago. He helped me navigate my way through a series of projects and kept me from avoiding pitfalls as I learned the intricacies of experimental and computational research of silicon carbide electron spins. He provided an unyielding confidence in the importance of my research, even in times it was difficult for me to see it. I also want to thank him and the other members of my committee, Aashish Clerk, Supratik Guha, and Sidney Nagel, for their support and feedback throughout my graduate process.

I cannot thank enough the many mentors I had at different stages of my Ph.D. for providing their time and expertise when collaborating on projects. Sam Whitely offered to show me the ropes when I needed to join a lab my first month at UChicago to start an experimental class. He taught me the importance of uncompromised cleanliness and attention to detail while teaching me cleanroom fabrication procedures. During that first year, Kevin Miao also was eager to show me how to operate the gargantuan experimental setup that is the optics and electronics we use to study our divacancy samples. Kevin became a partner in crime after helping me decide what research direction to choose for the divacancy. He taught me the ins and outs of publishing in a peer reviewed journal while being locked out of the lab due to COVID quarantine mandates. Yeghishe Tsaturyan became an invaluable mentor in mechanical and optical cavity structures, and also offered incredible advice on best research practices and how to approach my future career as a

scientist. I will always remember fondly our adventures as we troubleshot divacancy measurements during COVID lockdown shifts while discussing each other's research goals and how we could combine them in a hybrid quantum system architecture.

I also want to say thank you to all the other amazing labmates in the Awschalom lab that made the experience one I will never forget. The group of experienced grad students, Chris Anderson, Alex Crook, Alexandre Bourassa, Sam Whitely, and Kevin Miao, that made up the silicon carbide research effort when I joined offered an abundance of guidance and friendship in my early years. Many thanks also to the silicon carbide team during my later years of Cyrus Zeledon, Swathi Chandrika, and Yeghishe Tsaturyan for providing an awesome environment to pursue new research ideas and create strong friendships along the way. Also huge thank you to all my Awschalom lab colleagues I did not have the pleasure of working closely with on other projects who were always willing to help or offer advice during my years as a fellow denizen of the windowless LL2 hallways of ERC.

I want to give a big thank you to all my classmates and professors in the physics department that jumpstarted my academic journey. Shout out to those that shared in the years of board games and intramural sports during my time here. And lastly, thank you to my friends and family for supporting me throughout this journey. Their encouragement helped make this thesis a reality.

Abstract

The emerging fields of quantum computation and communication offer many advantages to existing technologies. Quantum systems developed to realize these advantages face challenges such as decoherence or poor coupling to other systems. These problems can be tackled using spin qubits found in crystallographic defects in silicon carbide (SiC). The divacancy defect in the 4H polytype of SiC is composed of an electron-spin system with fast electromagnetic and optical control housed in a technologically mature semiconductor. This thesis will discuss a pair of results that position the divacancy as a strong candidate for inclusion in hybrid quantum systems or for long-distance entanglement generation. The first result is an experimental demonstration of enhancing the coherence of a qubit composed of a single divacancy's ground-state spin levels by enhancing its natural insensitivity to environmental noise. The application of a continuous microwave-frequency drive leads to a measurement of the qubit's inhomogeneous dephasing time in a decoherence protected subspace to be >22 milliseconds with an accompanying Hahn-echo coherence of >64 milliseconds. The second result constitutes the design and simulation of a hybrid optomechanical resonator to address a single divacancy in a monolithic cavity design that could preserve the divacancy's optical and spin properties. We estimate >150x enhancement of the divacancy's emission rate via coupling to the simulated optical cavity modes. We also estimate the optomechanical cavity to have quantum cooperativity >1000 from feasible device parameters, well above the threshold for operation at its quantum groundstate. This could enable a proposed scheme to store emitted near-infrared divacancy photons as mechanical excitations before reading them out at telecom wavelengths for transmission over low-loss optical fiber infrastructure.

Chapter 1

INTRODUCTION

The ability to communicate with nearly anyone across the globe using modern telecommunication infrastructure is one of humanity's greatest achievements. Today, a combination of telephone lines, fiber optic networks, short- and long-wave radio, and satellites are employed to send information between different parties. Among these networks, the internet, or *world wide web*, is the bedrock of modern technology due to its ability to enable fast, high-volume data packet exchange between the powerful computers of today. Back in the 1960s, Thomas Merrill and Lawrence Roberts connected a computer in Massachusetts to one in California, which would be the first computer link in "ARPANET," the predecessor to the internet as we know it. Over the 60 years since ARPANET, processing speeds and memory sizes used by computers increased dramatically, so, in tandem, similar advancements in information transfer needed to occur. By 1991, through work by Emmanuel Desurvire and David Payne, signals sent through electrical cables were superseded by erbium-doped optical fibers with in-line amplifiers of the telecom photons carrying information. Modern optical fiber infrastructure boasts transfer rates of hundreds of gigabits per second over many hundreds of telecom wavelength channels to keep up with the information flux demands. Today though, computers are entering a potentially new paradigm, one where information will be represented by exploiting quantum effects, a departure from several decades of purely classical information theory. This shift from classical to quantum computing means the ability to transfer delicate quantum information at scale, with high through-put, and at the right wavelengths to utilize the fiber optic infrastructure already in place.

Quantum information science is the study of systems whose quantum mechanical properties can be manipulated to store and process information [1] in analogous ways to classical bits found in conventional computer chips. Developing a computing architecture that exploits the full potential of these quantum bits, or "qubits," could have numerous applications, including studying material properties [2], molecular medicine design [3], and new cryptographic safeguards [4]. Exponential speedups in computing time for certain algorithms are a key goal of quantum computing, such as Shor's algorithm [5]. Yet, demonstrating a "quantum advantage" over classical super computers remains a challenging task experimentally due to the fragile and short-lived nature of quantum states. Put simply, the longer a qubit can maintain its "coherence," or lifetime, during an experiment, the more logic operations can be performed on that qubit, and a quantum processor built from those qubits can be more powerful. There are thus tradeoffs between shorter coherence and more control that must be considered, as more control channels leads to shorter qubit lifetimes. Only a few experiments so far have reached the quantum advantage milestone as of 2025, including a 53-qubit superconducting processor [6] and a photonic qubit system performing Gaussian boson sampling [7]. The current landscape of what systems will make the best quantum processors is still very much in the air. The analogous system of silicon transistors for classical computers has not been found yet. Many other quantum systems are still being considered as potential qubits each with their own unique properties.

Besides scaling quantum computation, quantum communication channels must be developed as well. This process is accomplished by entangling a "stationary qubit" with a pulse that can travel over long distances, called a "flying qubit". Entanglement, a term coined in a paper by Schrödinger in 1935 [8], maps the quantum state of one particle onto another, and if they are separated, a measurement on either particle can reveal the original quantum state encoded.

Transmission of a quantum state was experimentally accomplished for qubits for the first time in 2013 using electron spin qubits in diamond emitting visible light photons that traveled a distance of 3 m [9] using photons of visible wavelengths. The major problem is that to be able to do entanglement over the mature, low-loss optical fiber networks utilized by classical communication protocols, qubits must be encoded at telecom frequencies. Frequency conversion can introduce severe attenuation and many additional loss channels. This severely limits the options of candidate systems for quantum computing or computation and has led to a thrust to create hybrid quantum systems [10] that find efficient ways to connect existing qubit systems operating at vastly different energies such as exploiting non-linear optical properties. The other way is to develop quantum "transducers" that bridge the energy gap between two established systems, such as coupling the mechanical motion of two systems to enable quantum state transmission. A summary of the criteria for a system, or set of interconnected systems, that could provide a platform for quantum computation and communication that addresses the concerns we have mentioned was laid out by DiVincenzo in 2000 [11]. In this thesis, we will narrow our scope to two of those criteria: extend the coherence of qubits and provide an interface between stationary and flying qubits.

For enhancing coherence properties, we will be studying solid-state semiconductor qubit systems composed of naturally occurring, atom-like spin states in lattice defects. The first such defect shown to have properties necessary for qubit applications was the nitrogen vacancy center defect [12], and in the more than twenty years since, an abundance of other defect systems have also been studied as qubits [13]. From the perspective of pure coherence extension for potential scalable quantum memories in the solid-state, these systems seem to lag behind systems that offer better protection from noise sources, such as nuclear spins [14], which are more sensitive due to lower gyromagnetic ratios. We want to investigate qubits that have inherent protection from

environmental fluctuations but retain coupling pathways to interact with other quantum systems. In other words, those that do not offer the fastest qubit computation times nor the longest lifetimes, but offer a mix of both along with a degree of in-situ flexibility depending on how the systems are addressed. This is the regime that solid-state defect spin qubits inhabit. For instance, the large electronic band gap these qubits inhabit isolate them from many noise sources inherent to their semiconductor hosts. [15–19] Also, the qubits are receptive to lengthening of their coherence by sending microwave frequency control pulses that undo the effects of noise, a process called dynamical decoupling. [18,20,21]. As for methods of control, metal electrodes can be lithographically patterned on the substrate surface to selectively interface the defect with a variety of electromagnetic pulses [21–28] to enable longer coherence, sensing protocols, or control with. The semiconductor material platforms offer the ability to fabricate structures using mature techniques to enable addressing with resonant fields. [29,30] Perhaps the most useful feature is that many of these defects offer an optical interface whereby photons can be used to prepare, manipulate, and readout the spin state as a basis for entanglement protocols [9,31].

The semiconductor of choice for this thesis will be silicon carbide, a material with many use cases due to its fantastic electromagnetic, thermal, and mechanical properties. We will discuss the wealth of studies on the divacancy defect, an optically addressable defect with a well-protected spin system, similar in composition to the nitrogen vacancy center in diamond. In particular, we will study one of the species of divacancy having a configuration in its crystal lattice with low symmetry. This lends it some unique properties that we will exploit in an experiment extending its coherence properties to values on par with nuclear spins without fully sacrificing its high-degree of electromagnetic control. This positions the divacancy as a strong candidate for use in hybrid quantum systems, the second focus of this thesis.

Returning to the DiVincenzo criteria, the second focus of this thesis will be centered around the search for an interface between stationary and flying qubits for quantum communication applications. In this case, the stationary qubit will be a divacancy defect, which has already mentioned has a robust spin-to-optical interface that could be utilized to readout the spin state of a divacancy qubit at long distances via entanglement to a telecom photon, as has been demonstrated at metropolitan scales between two distant nodes with the nitrogen vacancy center. The method pursued here will be using a mechanical oscillator as a quantum transducer to bridge the energy gap between the divacancy excitation at near-infrared (NIR) wavelengths and telecom wavelengths. In particular, we will utilize the ability of light to induce mechanical motion via the optomechanical effect. It was Einstein, who in 1909 first wrote down the first relations between the radiation pressure force on a movable mirror [32], and pioneering experimental demonstrations followed in the 1930s. Thermal effects still dominated the motion, masking any quantum applications, and it was only in the 1980s that the backaction of the membrane on the laser field addressing it in a cavity structure was exploited to reach an atoms motional ground state [33]. In the past decades, many geometries of mechanical oscillators were cooled to their mechanical quantum ground-state [34–36], paving the way for many applications. One of the more recent goals utilizing this ground-state operation is to realize microwave to optical conversion of quantum states utilizing the strong photon-phonon interactions produced in cavity structures [37,38] to potentially connect quantum computers using microwave frequency qubits to flying qubits.

The application of optomechanics in this thesis will be presenting the design of a proposed hybrid quantum device that exposes a divacancy qubit to strong photon and phonon fields contained in a silicon carbide membrane, enhancing the interaction strength between the qubit and the fields. Mirror coatings on the membrane will realize high amplitude optical and mechanical

cavity fields, with the interaction with the optical fields enhancing the emission rate of the divacancy's optical dipole. An optomechanical effect, enabled by estimation of ground-state operation at 4 K, will then be utilized to store an emitted divacancy photon as a mechanical excitation. The reverse process then can transfer the mechanical excitation, still encoded with the information about the divacancy spin qubit, to a telecom frequency photon. The properties of the device will be estimated using finite-element simulations to show the ability of this device to possess a high degree of cooperativity between the spin and the optical field, as well as between the optical and mechanical field to position it as a strong candidate for a quantum transducer.

This thesis draws from the following publication for the results presented in Chapter 5:

1. K.C. Miao, **J.P. Blanton**, C.P. Anderson, A. Bourassa, A.L. Crook, G. Wolfowicz, H. Abe, T. Ohshima, D.D. Awschalom, Universal coherence protection in a solid-state spin qubit, *Science* **369** 6510 1493–1497 (2020).

Chapter 2

FUNDAMENTALS OF SPIN QUBITS

2.1 Classical bits

The bedrock for quantum platforms that can allow us to access new ways of manipulating, storing, and transmitting data is of course the classical “bit”. Thus, we begin by briefly describing how information is defined, stored, and manipulated by classical bits. “Bit” here is a shorthand way to define any object that can be put into one of a pair of states, usually called the “1” state and the “0” state. These two states are distinct and are used to represent information in binary form, either by themselves or as a collective.

Flipping a light switch is a common analogy: the “on” state for a bright room could be represented by the “1” state, and, similarly, the “off” state can be called the “0” state. The most important features of the bit are its mutability, stability, and transferability—it must be able to flip states at a low energy cost, retain its state over a relatively long time against spurious signals threatening to flip it, and information about its state should easily communicated to other nodes. For mutability, a light switch on your wall is easy to flip, relative to how often you enter or leave a room. For stability, save for accidentally bumping it, the switch will rarely turn off on its own. But our bit loses utility if we want to, say, tell our neighbor if our light switch is on/off, which would require other wire hooked to it circuitry. The transferability of communicating the physical latch’s position is cumbersome. Overall, we can say the light switch is a good bit for the job of lighting a room. These three qualities encapsulate the fundamental questions for building good qubits that this thesis will address. So far, all we have done is enable us to define this classical bit

as a binary element. If you observe the bit, it will be found to be in either of its two states, and that is good enough for most cases.

Now, if we want to use bits to represent complex information, we must copy our simple bit millions or even billions of times and be able to store information in each one to be retrieved later. This is the job of memory devices such as compact discs “CDs” or flash memory drives. The fact that the bit we created has only two states is no accident, as binary representation of information is a very efficient way to store it using physical systems that can only be in one of two energetic states. Computer chips composed of transistor logic then can read individual bits and reassign others to perform all the functions of modern computers. It is the job of algorithms to perform the sequential Boolean logic operations on one or two bits at a time in rapid succession. This discrete, one-by-one reassignment of the values of a vast number of classical bits done by modern computer processing units underpins our current classical computing technology.

2.2 The two-level system qubit

Having defined the basics of a classical bit in the previous sections, we now can define a quantum bit, or qubit. Succinctly, a qubit is any system where the two distinct states are governed by the laws of quantum mechanics. In this section, we will first define what it means for the system to be “quantum”, and then we go through a rigorous definition of the qubit that is the focus of this thesis: a two-level system electron spin qubit.

2.2.1 Quantum vs. classical states

The laws of physics seek to define a system’s characteristics using quantities that can be measured. Such quantities, like an object’s mass, speed, reflectance, etc., are deem “classical.” Classical quantities can be observed and measured in everyday settings. Classical mechanics is the study of such properties, and its predictions enable everything from skyscrapers not falling under stress to

communications satellites orbiting stably. Yet for objects that are very small, on the scale of atoms, another domain of physics begins to give more accurate predictions: quantum mechanics. If the states of a system can be described with energy differences on the order of $h = 6.626\times10^{-34}$ J·s known as the Plank's constant, then it can begin to be considered quantum rather than classical. Plank's constant is fantastically small, so it can be tricky to measure such properties, but it underpins the behavior of all atoms. There are many surprising and interesting consequences of quantum systems, but we will focus now on those properties that defines a new domain of computing that is impossible for classical bits to access.

2.2.2 The two-level system qubit

For a quantum state, $|\psi\rangle$ is the wave function written in Dirac notation and we begin by writing the Schrödinger equation, which can be thought of as the equation of motion for the state:

$$\hat{H}|\psi\rangle = E|\psi\rangle. \tag{2.1}$$

$\hat{H}$ is the matrix Hamiltonian for the quantum state that describes how it evolves, similarly to the Lagrangian in classical mechanics. E is the energy of the system. Basically, given the state of the system, the Hamiltonian can tell you the possible energies the system is allowed to have when driven by some external force(s). These quantities can be time dependent or independent, but for now, the important thing to note is a quantum states can represent a bit with their energies being the bit's state. External forces can flip the bit's state and that is the fundamental interaction of performing quantum computation using qubits.

Just like a classical bit, we will constrain ourselves to a two-level system qubit defined to have just two measurable states. These states will be represented by the basis $|0\rangle, |1\rangle$, of which there is total flexibility choosing their vector representation depending on the dimension of the

Hamiltonian. Formulating this in the language of linear algebra, we begin to define the possible states of our qubit as a vector:

$$|\psi\rangle = (a + ib)|0\rangle + (c + id)|1\rangle, \tag{2.2}$$

where a, b, c, d are real-valued constants such that any linear combination of our basis choice must span the vector space, or Hilbert space, defined by the Hamiltonian operator. The constraint is that the normalized vector satisfies:

$$1 = (a + ib)^2 + (c + id)^2 = |\alpha|^2 + |\beta|^2, \tag{2.3}$$

with complex constants α, β. It must be true that $|\psi\rangle$'s state can only give $|0\rangle$ or $|1\rangle$ as quantum mechanics must give physical results when measured, but such linear combinations, or superpositions of states *do exist* and can be leveraged as we will see in the following chapters. Measurement in quantum mechanics means something a bit different than the usual classical sense, but we will not delve too deeply into the definitions right now. In Dirac notation, we write the constraint that the quantum state must be normalized to 1 for given any prefactors on our basis:

$$\begin{aligned} 1 = \langle\psi|\psi\rangle &= (\alpha^*\langle 0| + \beta^*\langle 1|) * (\alpha|0\rangle + \beta|1\rangle) \\ &= |\alpha|^2 + |\beta|^2, \end{aligned} \tag{2.4}$$

where $\langle\psi|$ is the conjugate transpose, denoted $|\psi\rangle^\dagger$ of the state and due to orthogonality of the basis, written as the following relation:

$$\begin{aligned} \langle 0|0\rangle &= \langle 1|1\rangle = 1 \\ \langle 0|1\rangle &= \langle 1|0\rangle = 0. \end{aligned} \tag{2.5}$$

The above is due to the fact we must have an orthonormal basis for this Hilbert space:

$$|0\rangle = \begin{bmatrix}1\\0\end{bmatrix}, |1\rangle = \begin{bmatrix}0\\1\end{bmatrix}. \tag{2.6}$$

This will be the basis we will use throughout this thesis in our treatment of a two level system representing an electron spin qubit. The last constraint we will mention for quantum states is that adding a global phase factor, $e^{i\varphi}$ retains the same physical meaning. This means measuring an observable for the quantum state will not depend on such a phase factor.

2.2.3 Bloch sphere formalism

We are now ready to add formalism that will be useful to define and visualize the results for the TLS of spin-1/2 states of an electron. A spin-1/2 system has two possible states: spin up and spin down. We make the choice of basis $|1\rangle = |\uparrow\rangle$ and $|0\rangle = |\downarrow\rangle$ as representations of our qubit states for spin "up" and spin "down" respectively.

The arbitrary choice of constants allows a lot of freedom, and there is a particular choice of the constants we will use, namely:

$$|\psi\rangle = \begin{bmatrix}\cos\frac{\theta}{2}\\ e^{i\varphi}\sin\frac{\theta}{2}\end{bmatrix}, \tag{2.7}$$

where θ and φ are the polar and the azimuthal angles in spherical coordinates, respectively. Using the spherical coordinate transformation, we can turn a vector in the cartesian plane, $\vec{r} = (x, y, z)$, into coordinates on the Bloch sphere, as in. Figure 2.1 Linear combinations of our basis states now are mapped to points on the sphere and are physically realizable objects in the laboratory called

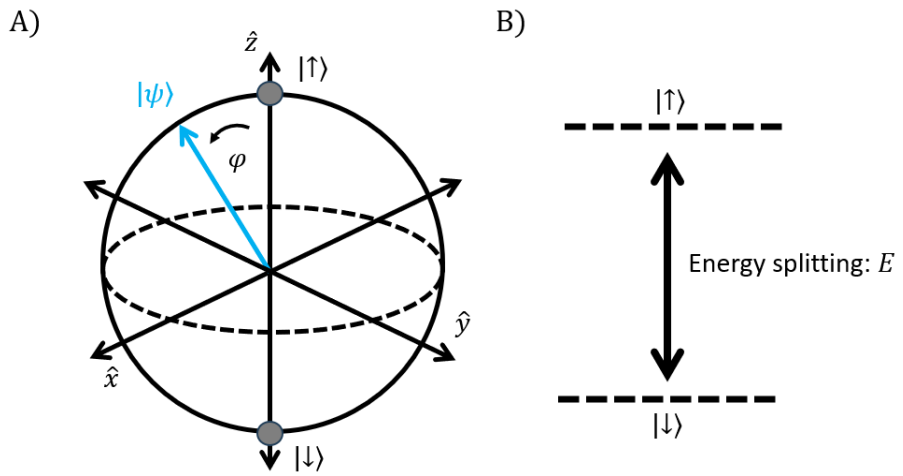

Figure 2.1 **Visualization of two level qubit on the Bloch sphere**. (A): A quantum state (blue arrow) is mapped onto the Bloch sphere. The intersections with the z-axis correspond to the basis states of the qubit. These two states would be the only physical states of a classical bit, but qubits can access infinite superposition states. (B): The energy diagram of the TLS containing an energy difference of E between the basis states represented by the Bloch sphere.

superposition states. They can be attained by driving our qubit with excitation fields near the energy splitting between the up and down states. We can appreciate now that quantum mechanics allows this qubit to exist in an innumerable number of states instead of just two. When measured directly though, we find this collapses back into just two states, the points on the poles. The kinds of interactions possible with superposition states is what differentiates qubits from classical bits. In order to describe better the properties of superposition states of this spin-1/2 system, we must enter the time domain.

2.3 Time evolution of quantum states

We are now ready to return to the Schrödinger equation and write down the most general form for when the state is allowed to evolve in time, due to the presence of the time-dependent Hamiltonian,

$\widehat{H}(t)$, under the equation:

$$i\hbar\frac{\partial}{\partial t}|\psi(t)\rangle = \widehat{H}(t)|\psi(t)\rangle. \tag{2.8}$$

Here $\hbar$ is the reduced Plank's constant, $h/2$. This full picture, involving a differential matrix equation, can be quite complicated to solve generally, so in this section we will focus on a very narrow case for a spin-1/2 system.

Having just written down this general case, we apply the simplification $H(0) = H(t)$, so the forces can be considered static but the state can still evolve. Here we can use the TLS Hamiltonian:

$$\widehat{H} = \frac{\hbar\omega_o}{2}\,(|1\rangle\langle 1| - |0\rangle\langle 0|). \tag{2.9}$$

As defined here, the energy difference, or splitting, between our two states is $\hbar\omega_o$. In other words, it takes that much energy, at least, to flip our quantum bit. Here $|0\rangle$ takes on the role of the ground state and $|1\rangle$ is the excited state. Using the matrix representation of our states, this simplifies to:

$$\widehat{H} = \frac{\hbar\omega_o}{2}\hat{\sigma}_z, \tag{2.10}$$

where we utilize the z-axis Pauli spin matrix, and the complete set of matrices is:

$$\hat{\sigma}_x = \begin{bmatrix}0 & 1\\ 1 & 0\end{bmatrix}, \hat{\sigma}_y = \begin{bmatrix}0 & -i\\ i & 0\end{bmatrix}, \hat{\sigma}_z = \begin{bmatrix}1 & 0\\ 0 & -1\end{bmatrix}. \tag{2.11}$$

It is no accident that our Hamiltonian relates to the energy splitting of a spin oriented along the z-axis, aligning with the Bloch sphere representation in Eq. (2.7) as the choice of basis for the qubit

is arbitrary. Solving the matrix equation for the energies of the states gives us what are called the eigenvalues for the system:

$$E_{|1\rangle} = \frac{\hbar\omega_o}{2}, E_{|0\rangle} = -\frac{\hbar\omega_o}{2}. \tag{2.12}$$

We write E_n as the eigenvalue of the state n. In the language of quantum mechanics, the basis states are called the eigenvectors or eigenstates. The eigenstates critically represent the real-value, measurable energies of a spin-1/2 system in nature. Another term for this is stationary state. What makes these states even more important is that the general time-evolution state can be represented by a linear combination of just these states.

Having defined the time independent Hamiltonian for our spin qubit, we can actually substitute it into the time *dependent* Schrödinger equation, Eq. (2.8), and look at the resulting state evolution over time. We substitute the eigenvalues in, and obtain a linear first-order differential equation:

$$i\hbar\frac{\partial}{\partial t}|\psi(t)\rangle = E_{|0\rangle,|1\rangle}|\psi(t)\rangle. \tag{2.13}$$

This has the solution of an exponential differential equation, where the state of the system at $t = 0$ is energy E:

$$|\psi(t)\rangle = |\psi(0)\rangle e^{-i\frac{Et}{\hbar}}. \tag{2.14}$$

The exponential has a name: the time-evolution operator. This result illustrates that stationary states of a system evolve rather simply over time for a static Hamiltonian, only acquiring an extra phase factor per unit time.

Now we are equipped to answer the question of how to write the general state of our TLS:

$$|\psi(t)\rangle = \sum_{n=1}^{N} c_n |\psi\rangle_n e^{-i\frac{Et}{\hbar}}. \tag{2.15}$$

This is the general form for a state's time evolution composed of only a linear combination of energy eigenstates. The power of this representation comes from the fact that phase evolution of the stationary states can be tracked and measured.

2.4 The rotating wave approximation

The experiments done in this thesis with an electron spin found in a divacancy defect system can be described as a time varying electric or magnetic field rotating the spin between its energy levels. When several of these experiments are done in succession, it makes sense to consider the problem as a transfer of an average population of spins between these energy states. This transfer is called "Rabi oscillations" and is how our qubit's state can be changed during an experiment. Before we can define Rabi oscillations, we must first simplify the time dependent Hamiltonian when we add a sinusoidal drive to an electron spin system.

We start by writing the interaction between the dipole moment, of the spin and an electric field (or magnetic field, $\hat{B}$, the treatment is the same:

$$\hat{H}_{dipole} = -\hat{d} \cdot \hat{E}. \tag{2.16}$$

Now, a general time-varying sinusoidal electric field takes the form:

$$\hat{E}(t) = A_1 \cos(\omega t + \theta), \tag{2.17}$$

and the electric dipole, of magnitude d, for a z-axis oriented electron spin, is:

$$\hat{d} = -\begin{bmatrix} 0 & d \\ d & 0 \end{bmatrix}. \tag{2.18}$$

The dot product becomes a product for a drive along the dipole, and so rescaling with $\hbar\omega_o = d\frac{A_1}{2}$, and using the Pauli matrices (Eq. (2.11), we get the new driven Hamiltonian for our electron spin:

$$\widehat{H}(t) = \frac{\hbar\omega_o}{2}\sigma_z + \Omega\cos(\omega t + \theta)\hat{\sigma}_x, \tag{2.19}$$

where the amplitude of the drive is now rescaled to Ω. This drive will necessarily cause the state of our qubit to precess at frequency ω, but there is a well-known simplification when the drive is near-resonant with the energy difference of the TLS known as the rotating wave approximation, abbreviated RWA.

This time dependent drive is necessary because as in Eq. (2.15), the c_n are constant and thus population cannot be transferred between the states in order to produce superpositions that will be exploited to make a qubit. To begin with the approximation, we will make a first order expansion of the Hamiltonian and only keep the terms of form:

$$\widehat{H}(t) = \widehat{H}_0 + \widehat{H}_1(t). \tag{2.20}$$

This approximation is thought of as moving into the interaction picture where we have a bare electron spin Hamiltonian $\widehat{H}_0$ and a perturbation $\widehat{H}_1(t)$ caused by the drive. This means we can work with states that are time independent, retaining the fact that our qubit should not flip on its own. This stability for our qubit is one of the core tenants of a strong bit we discussed at the start of this chapter. The power of the RWA is that even though the states technically are undergoing

Lamor precession at all times in the frame of reference of the laboratory, if there is a static magnetic field present in the rotating frame, the states can be considered stationary.

2.5 The interaction picture

In quantum mechanics, the interaction picture is a simply a change of basis to a more favorable one where the states are time-independent. Applying a unitary operator, $\widehat{U}$, to our state will transform it into a basis that represents the reference frame of the RWA:

$$|\psi\rangle_{RWA} = \widehat{U}|\psi\rangle. \tag{2.21}$$

Another way to state our goal here is to modify our Hamiltonian, and the result from quantum mechanics for a general unitary operator is as follows, starting with the Schrödinger equation in the RWA frame:

$$i\hbar\frac{\partial}{\partial t}|\psi\rangle_{RWA} = \widehat{H}_{RWA}|\psi\rangle_{RWA}, \tag{2.22}$$

where the new Hamiltonian can be written in terms of the original one and the unitary operator:

$$\widehat{H}_{RWA} = -\widehat{U}^{\dagger}\frac{\partial\widehat{U}}{\partial t} + \widehat{U}^{\dagger}\widehat{H}\widehat{U}. \tag{2.23}$$

By convention, we will take a specific unitary operator defined as:

$$\widehat{U}(t) = e^{-i\frac{\hbar\omega_o}{2}\widehat{\sigma}_z}, \tag{2.24}$$

and now we can simplify the first term of $\hat{H}_{RWA}$:

$$\hat{U}^{\dagger}\frac{\partial U}{\partial t} = -\hat{U}^{\dagger}\hat{U}\frac{\omega_o}{2}\hat{\sigma}_z = -\frac{\hbar\omega_o}{2}\hat{\sigma}_z. \tag{2.25}$$

We now must expand the second term, $U^{\dagger}\hat{H}U$, in order to finish defining the rotating wave Hamiltonian:

$$\begin{gathered}\hat{U}^{\dagger}\hat{H}\hat{U} = \hat{U}^{\dagger}\left(\hat{H}_0 + \hat{H}_1(t)\right)\hat{U} \\ = \hat{H}_0 + \Omega\cos(\omega t+\theta)(\cos(\omega t)\,\hat{\sigma}_x + \sin(\omega t)\,\hat{\sigma}_y).\end{gathered} \tag{2.26}$$

Now by defining the raising and lower spin matrices, we can conveniently continue to expand the left-most term:

$$\begin{gathered}\hat{\sigma}_+ = \begin{bmatrix}1 & 0\\ 0 & 0\end{bmatrix}, \hat{\sigma}_- = \begin{bmatrix}0 & 0\\ 1 & 0\end{bmatrix}, \\ \hat{U}^{\dagger}\hat{H}\hat{U} = \hat{H}_0 + \frac{\Omega}{2}\left(e^{(i\omega t+\theta)} + e^{(-i\omega t-\theta)}\right)\left(e^{(-i\omega t)}\hat{\sigma}_+ + e^{(i\omega t)}\hat{\sigma}_-\right).\end{gathered} \tag{2.27}$$

Here we can finally invoke the simplification of the RAW. Fast precessions, relative to ω, are discarded because the resonant driving terms contributes far more to the evolution of the spin state. We simplify and collect terms in the expansion that contain 2ω and write:

$$\begin{gathered}\hat{U}^{\dagger}\hat{H}\hat{U} = \hat{H}_0 + \frac{\Omega}{4}((e^{i\theta}+e^{-i\theta})\hat{\sigma}_x + i(e^{i\theta}-e^{-i\theta})\sigma_y + \\ + e^{-i(2\omega+\theta)t}\hat{\sigma}_+ + e^{i(2\omega+\theta)t}\hat{\sigma}_-)\end{gathered} \tag{2.28}$$

Now neglecting those fast oscillating terms, we see the raising and lowering terms are fully canceled under the approximation, and we obtain, in the end, our RWA full Hamiltonian:

$$\hat{H}_{RWA} = \hbar\left(\frac{\omega_o}{2} - \frac{\omega}{2}\right)\hat{\sigma}_z + \frac{\Omega}{2}(\cos(\theta)\,\hat{\sigma}_x - \sin(\theta)\,\hat{\sigma}_y). \tag{2.29}$$

2.6 Rabi oscillations

Within the rotating frame, we can begin to discuss the mechanisms that will yield a qubit with the full functionality of a classical bit. In this section, we will describe how to flip the qubit's spin reliably. We want to write down the eigenvectors and the corresponding eigenvalues of the system in the RWA frame. We start by defining the detuning, $\Delta = \omega_o - \omega$, between the drive and the qubit's energy splitting frequency. Choosing the lower energy state to be along the axis of the magnetic field, we call it $|\downarrow\rangle$, and so $|\uparrow\rangle$ will be the higher-energy, anti-aligned state. Also we set $\hbar = 1$ for compactness. Expanding fully the 2x2 Pauli matrices we can write the time-independent Schrödinger equation for the Hamiltonian, (2.29) in the rotating frame:

$$\begin{bmatrix} \frac{\Delta}{2} & \frac{\Omega}{4}((e^{i\theta}+e^{-i\theta}) - (e^{i\theta}-e^{-i\theta})) \\ \frac{\Omega}{4}((e^{i\theta}+e^{-i\theta}) + (e^{i\theta}-e^{-i\theta})) & \frac{\Delta}{2} \end{bmatrix} |\uparrow,\downarrow\rangle = E_{\uparrow,\downarrow}|\uparrow,\downarrow\rangle. \quad (2.30)$$

After diagonalizing the above matrix, we get the solutions in our basis $|1\rangle = (1\ \ 0)^T$, $|0\rangle = (0\ \ 1)^T$:

$$\begin{aligned} |\uparrow\rangle &= \sin\left(\frac{\theta}{2}\right)|0\rangle + e^{i\theta}\cos\left(\frac{\theta}{2}\right)|1\rangle, E_{\uparrow} = \frac{\sqrt{\Omega^2+\Delta^2}}{2} \\ |\downarrow\rangle &= \sin\left(\frac{\theta}{2}\right)|0\rangle - e^{i\theta}\cos\left(\frac{\theta}{2}\right)|1\rangle, E_{\downarrow} = -\frac{\sqrt{\Omega^2+\Delta^2}}{2}. \end{aligned} \quad (2.31)$$

Now consider we begin an experiment that is made up of a large ensemble of trials where each time our electron spin is prepared into the lower energy ground state, $|0\rangle$. If we want to flip our qubit, that is equivalent to attempting to flip the spin state. In the ensemble picture, taking a look at the collective behavior of the spin all at once, we want to move every state of our ensemble

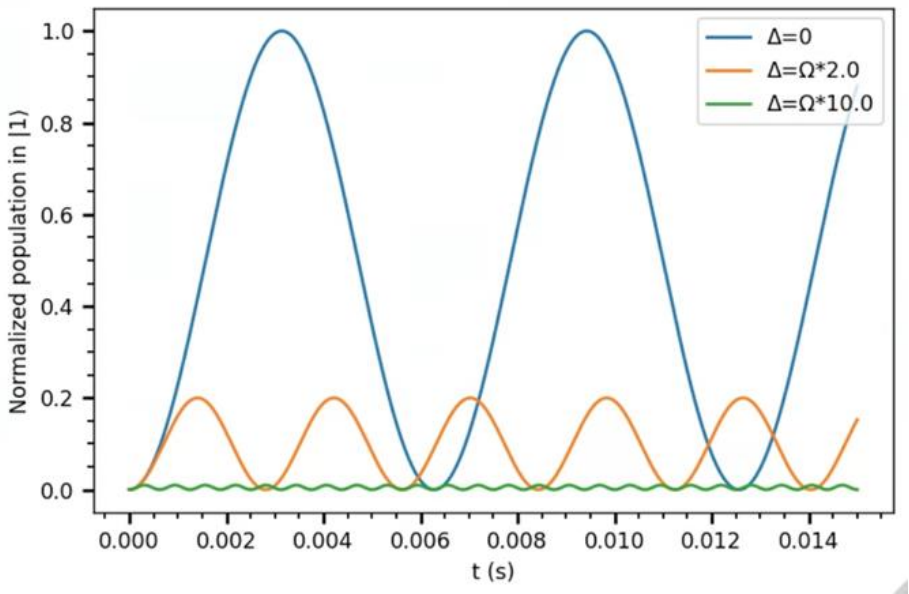

Figure 2.2. **Rabi oscillations of qubit population.** The curves here show population transfer (Eq. (2.35)) of a qubit showing the maximum ratio of the population that can be transferred to the excited state, $|1\rangle$, after beginning the experiment with all the population in the ground-state, $|0\rangle$. Detunings on the order of the Rabi rate lead to significantly lower maximum population transmission.

from $|0\rangle$ to $|1\rangle$. We apply a time dependent electromagnetic drive to the spin to accomplish this and our solution above now lets us gain some quantitative understanding of it. The quantity in question is the population that is in $|1\rangle$ at time t. In Dirac notation, where the evolving state of the qubit is $|\psi\rangle$, we write:

$$Population\ in\ state\ |\varphi\rangle \text{ at time t } = |\langle\varphi|\psi(t)\rangle|^2. \tag{2.32}$$

Now we utilize Eq. (2.15) where we wrote any state of our TLS as a linear combination of energy eigenstates. This is especially useful because it does not matter what frame of reference we are in

because the expansion holds even in the interaction picture of the RWA. Multiplying by the projection operator for the states $|\uparrow,\downarrow\rangle$ we write:

$$|\langle 1|\psi(t)\rangle|^2 = \left|\sum_{n=\uparrow,\downarrow}^{2} \langle 1|n\rangle\langle n|0\rangle e^{-iE_n t}\right|^2. \tag{2.33}$$

Measuring the population in $|1\rangle$ at time t is then given by:

$$|\langle 1|\psi(t)\rangle|^2 = \left|\sum_{n=\uparrow,\downarrow}^{2} \langle 1|n\rangle\langle n|0\rangle e^{-iE_n t}\right|^2. \tag{2.34}$$

Performing the matric multiplication using Eq. (2.31), we get:

$$|\langle 1|\psi(t)\rangle|^2 = \left(\frac{\Omega^2}{\Omega^2+\Delta^2}\right)\sin^2\left(\frac{\sqrt{\Omega^2+\Delta^2}}{2}t\right). \tag{2.35}$$

This is our formula for a Rabi oscillation describing controllable population transfer in our TLS electron spin qubit where Ω is called the Rabi frequency. The significance of Ω is that, when on resonance, $\Delta = 0$, we immediately see a simplification to bare sinusoidal driving with frequency proportional to Ω. This feels remarkable at first because these are the basis states of the system in the lab frame, not the rotating frame. It is instructive to consider non-zero detuning cases as well, plotted in Figure 2.2 because we will see later that knowing the exact resonance of a divacancy spin qubit in silicon carbide involves multiple factors. Understanding all the relevant experimental control mechanisms that lead to coherent Rabi oscillations in the lab setting is the first step towards a robust qubit platform built on creating superposition states of the spin and seeing how they interact with their environment. That information is crucial to evaluating what kinds of quantum

information storage or transfer protocols are the qubit can efficiently perform. Some environments are more hostile and can wholly prevent good qubit operation by inducing unwanted population transfer. This usually falls under noise that cannot be easily canceled out, which we will define as quasistatic noise in the next section. The bandwidth of the noise can vary greatly in different environments, so we need a way to quantify this to determine to what degree our qubits can operate in the face of their noisy environment.

2.7 Decoherence of quantum spin state

The previous sections focused on the ability to manipulate a qubit coherently in a vacuum, free from all environmental concerns. The subject of this thesis though are qubits composed of spin systems in a host crystal that is full of many sources of electromagnetic noise that can lead to "decoherence" of the qubit. Decoherence relates to any process where phase error is introduced into a superposition state of the qubit that cannot be easily accounted for and canceled out. The rate at which a qubit accumulates significant decoherence is one of the most important factors. A qubit encoded with information will, after some time, decohere and no longer hold useful information. Different qubits decohere on timescales ranging from nanoseconds to several minutes and beyond.

Thinking of the analogy to classical information, a qubit representing a quantum state for longer times means more time to perform logic operations on that information. There is a parallel effort to perform quantum logic operations faster and shield qubits from decoherence better. This is perhaps the most striking difference from classical bits, because many classical memory architectures are stable over the course of years, ready to be read out at any time.

The basic mechanism of decoherence is that each superposition state will suffer some error in the phase and amplitude of the state due to the other fields present. After some threshold, the errors will result in the state decaying over some timescale back to the unremarkable ground-state of the system. Unremarkable in that no usable quantum information remains to be measured or manipulated in the qubit. Characterizing that timescale allows us to learn the limits of our qubits and perhaps engineer some part of the system to remove or mitigate decoherence sources. The three time-scales most relevant to electron spin qubit decoherence will be defined in the following subsections.

2.7.1 Lifetime

Consider an electron spin, with two energy eigenstates under the influence of a magnetic field so that the states are separated by a non-zero energy. Consider first a closed quantum system where no external electromagnetic fields are present. If the qubit is prepared into one of its energy eigenstates, then energy conservation says it cannot swap to the other state, as there is no time dependent factor in the Schrödinger equation at all. This is of course a thought experiment and perfectly closed quantum systems cannot be built in the laboratory. All qubits exist in open quantum systems to some degree, and they are subject to energy transfer with their environment. The T_1 time describes at what rate will a qubit undergo energy relaxation into equilibrium with its environment, at which point all quantum information encoded into it is lost.

A basic is example is a spin prepared in its excited state $|\uparrow\rangle$, where after a time, T_1, it will be found in a classical mixed state of $|\uparrow\rangle$ and its ground-state $|\downarrow\rangle$, i.e., a thermal equilibrium state. The same process could be done preparing into a quantum superposition between those two states, where eventually if you observe the state population, you will not be able to measure anything more than a classical mixed state again. This is why T_1 is usually called the lifetime of the qubit.

All the protocols to make the superposition state through coherent population transfer around the bloch sphere must be completed on timescales much faster than the qubit lifetime. It should be noted that $T_1$is not a decoherence process explicitly but acts as an upper bound for the two decoherence processes discussed next.

Measuring the lifetime is relatively simple. Consider an ensemble experiment where we rotate the spin population into the $|\uparrow\rangle$ state initially. We can define the classical probability, $P_\uparrow(t)$, that an experiment will find the spin in $|\uparrow\rangle$ at time t as a simple exponential decay:

$$P_\uparrow(t) = \frac{P_\uparrow(0)}{2}(e^{(-t/T_1)} + 1). \tag{2.36}$$

Then we extract the qubit lifetime from the fit.

The kinds of processes that lead to these random decays in solid-state electron spin defects are spin-flips or population being driven by stray fields near resonance. It is a strong property of the kinds of qubits studied in this work that most of their $T_1's$ are not the limiting factor for experiments and can reach up to and beyond seconds in length, at which point it becomes increasingly difficult to measure due to averaging times ballooning to weeks-long time scales to see decay due to low collection efficiency.

2.7.2 Inhomogeneous dephasing time

A decoherence process must describe the decay-time of a superposition of the qubit. These superpositions live on the equator of the Bloch sphere and are defined by the phase relation between the eigenstates that compose them. This is where the term “dephasing” comes from to describe decoherence because once the qubit state has been rotated off of the poles, it can

accumulate phase not only from our drive, but other noise sources as well. In the most general form, the superposition state ψ for an electron spin TLS is described by:

$$|\psi(t)\rangle = \frac{1}{\sqrt{2}}\left(|\downarrow\rangle + |\uparrow\rangle e^{-iEt}\right), \tag{2.37}$$

with an energy splitting between the spin-up and spin-down states of E. The complex coefficients on the eigenstates determine where on the equator this superposition lies. Thus, we can see that the phase relation is directly related to the energy splitting.

Consider an experiment where we prepare the pure state $|\downarrow\rangle$ and perform coherent Rabi oscillation to generate a superposition state in the equator of the Bloch sphere. This movement is usually characterized by the angle traversed by the state while in the equator, in this case a $\frac{\pi}{2}$ rotation was performed. Once in the equator, we utilize our understanding of the rotating frame and see that the superposition state begins to precess in the lab frame. After a time $\frac{2\pi}{\Delta}$, the state returns after sweeping the equator, where Δ is again the detuning between the sinusoidal drive and the energy splitting. This is due to the extra term $\frac{\Delta}{2}\sigma_z$ in the RWA Hamiltonian, Eq. (2.29), adding phase in the Schrödinger picture.

What leads to dephasing though is when Δ is not constant between experiments, and there are phase errors $\delta\Delta$ accumulated in a time in the equator, t. If we tracked the rotation in the equator by measuring out the phase relation of the state, we would obtain sinusoidal graphs with different frequencies due to the different detunings $\Delta + \delta\Delta$ present for each individual experiment. It is a known result that averaging sines of different frequencies results in an exponential decay of a form e^{-t/T_2^*}. A fit to those averaging sines yields T_2^*, which we call the inhomogeneous dephasing time.

When we describe an electron spin qubit's T_2^* as being long, it is a statement about the qubit's inability to be influenced by its environment. Most of these environmental effects are incoherent and difficult to quantitively track and thus must be considered as averaged effects. The effect of nuclear spins of nearby atoms usually needs to be treated as an ensemble bath state for example. Yet we want more from our qubit. We are not seeking to only build memory qubits that can hold quantum information for several hours or even longer—there are other solid-state spin systems better suited. We are also interested in qubits that can selectively couple to other quantum systems. If we invert T_2^*:

$$T_2^* \sim \frac{1}{\Gamma}, \tag{2.38}$$

we can define Γ, which is what we call the resonance linewidth of the qubit. This quantity relates to the qubit's sensitivity to measure external fields or couple to fields from other qubit systems. With long enough T_2^*, more and more quantum gate operations can be done with a prepared quantum state, and across larger physical distances between qubits.

2.7.3 Hahn-echo time

In the last section we described a kind of phase error that our qubit accumulates when random energy shifts affect the energy level of the TLS. If the noise is more "well behaved" on a certain timescale so that over a time period the phase error is approximately constant, then the phase error can actually be canceled. This type of perturbation is called quasistatic noise and shares many of the same sources as those that define a qubit's T_2^*; mainly, nuclear spins or other TLS's in the

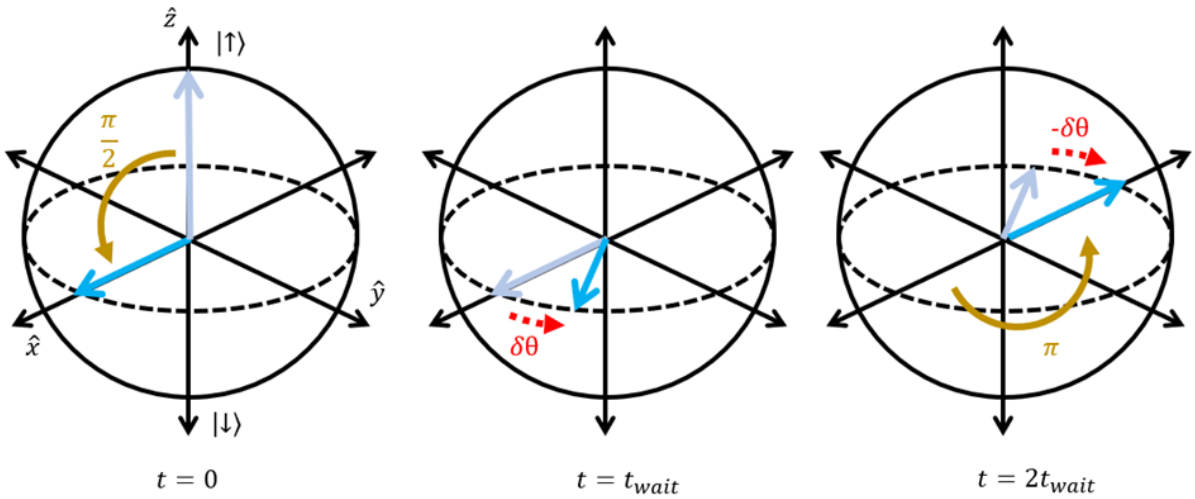

Figure 2.3: **Decoherence phase error in a qubit.** At $t = 0$, a pure state of the qubit in the $|\uparrow\rangle$ is created along the z-axis (light blue). After a $\frac{\pi}{2}$ rotation (gold), a superposition state now is in the equator of the Bloch sphere. After $t = t_{wait}$, inhomogeneous phase error $\delta\theta$ has been incurred. If a π rotation around the y-axis is done, the phase error can be canceled exactly by waiting until $t = 2t_{wait}$ when the rate of error accumulation is constant during both wait times. Quasistatic noise describes error sources that can be canceled by the π pulse.

material can have slow, fluctuating fields that affect the qubit. Being able to differentiate noise sources of different frequencies as quasistatic or not is very useful in understanding a qubit's environment.

To define the timescale of this quasistatic noise, we again prepare the qubit into an eigenstate and then rotate it onto the equator along the y-axis. Here, in a time t, it accumulates phase noise of a particular sign. Performing a π pulse and then letting the qubit sample the noise for time t again inverts the sign of the phase accumulation. If the phase accumulation rate is equal, this "refocuses" the qubit state as it now will be along the negative y-axis. Inverting the rotation to measure the qubit population's chance to be in the original eigenstate would yield 100% if all the phase error was due to quasistatic noise, this is diagramed in Figure 2.3. If the state is not readout, the phase-coherent state can undergo further rotations after such a refocusing pulse.

Quasistatic noise is only a descriptor up to a certain precision though. Nature does not like constants. During the phase accumulation after the refocusing pulse, there will inevitably be some

net change in the qubit phase and as seen for the case of measuring $T_2{}^*$, the oscillations measured will experience exponential dampening, where the Hahn-echo time, T_2 can be extracted from a fit to e^{-t/T_2}. The quasistatic noise effects are canceled out up to the ability to calibrate the length of the pulses. These π rotations are sometimes called refocusing pulses. Even if the noise changes over the course of multiple experiments, if it does not change over the course of a single experiment, then it will be canceled each time using this Hahn echo sequence.

We can see how this refocus works if we remember that two quantum states are equivalent if they are different by a single global phase $e^{i\delta}$. We start at $t = 0$ with a superposition state of our qubit that we prepare in the equator of the Bloch sphere:

$$|\psi(0)\rangle = \frac{1}{\sqrt{2}}\left(|\downarrow\rangle + |\uparrow\rangle e^{-iE(0)}\right). \tag{2.39}$$

After time spent sampling the noise in the equator $t = t_{wait}$ the π rotation is simply equivalent to swapping the basis $|\downarrow\rangle \leftrightarrow |\uparrow\rangle$ and phase accumulation happens on both of the basis states:

$$|\psi(2t_{wait})\rangle = \frac{1}{\sqrt{2}}\left(|\downarrow\rangle e^{-iEt_{wait}} + |\uparrow\rangle e^{-iEt_{wait}}\right), \tag{2.40}$$

Where we recognize the common phase factor and can say $|\psi(0)\rangle = |\psi(2t_{wait})\rangle$. While this means a superposition state cannot ever be perfectly readout after waiting some time, it does allow the environment to be probed by the superposition state, which can give insight into the host crystal or nearby field sources. This in turn defines an extended usable time scale for manipulating information encoded in quantum superpositions on qubits.

Chapter 3

THE DIVACANCY DEFECT IN SILICON CARBIDE

3.1 Introduction

This section will introduce the neutral divacancy defect in silicon carbide. The neutral divacancy, or VV^0, where the superscript refers to its electric charge, is found in the semiconductor silicon carbide (SiC) and is composed of adjacent missing carbon and silicon atoms. Throughout this thesis, we will use "divacancy" as shorthand for the VV^0 and mention when its non-neutral charge state is relevant. This localized feature in SiC has a pair of trapped electrons that will serve as the spin qubit for the work discussed in the following sections. The interaction between the spin-1 system and the crystal and external fields will be discussed in this chapter, where we begin in this section with the solid-state properties of SiC's crystal lattice that give rise to the divacancy spin qubit platform [17,39–43].

As a material platform, SiC combines the some of the coveted properties of diamond with the ease of fabrication and low cost of silicon. There has been interest in SiC for industrial applications long before qubit research, including in the high-power electronics sector due to excellent thermal properties and the ability to easily grow a thermally insulating oxidation layer. Heat dissipation in modern electronics continues to be a factor as the number of transistors per square micron increases in computer chips. Today, SiC is breaking into the CMOS market as an alternative to silicon in certain applications due to the development of wafer scale (4"+), low-

defect growth of epi-layers of SiC [17,41,44]. SiC continues to find applications in new technologies such as smart phones and space-faring vehicles, to name just a few.

Among the plethora of SiC's properties that make it an attractive candidate to host an electron spin qubit [45] we mention here four that are central to the success of the divacancy spin qubit: large bandgap of SiC, sparse magnetic noise from nuclear spins, high optical index of refraction and low phonon loss. SiC boasts a wide bandgap reaching up to 3.33 eV, which enables many species of localized electronic states to be protected from thermal noise. When cooled to cryogenic temperatures, the magnitude of energetic transitions that reside inside the bandgap suppresses the electrons from entering from either the valence or conduction band [46]. One of the most common sources of magnetic field noise relevant to the divacancy is from nuclear isotopes of the host crystal. It turns out that SiC has relatively low concentrations of both species that carry non-zero nuclear spin: carbon is 1.1% and silicon is 4.7% chance to be found to have a nuclear spin. When a material has a higher index of fraction than air, it can be used to confine photons in cavity structures due to higher rates of internal reflection. [47–52] Lastly, SiC's lattice has an ultralow acoustic impedance, a high speed of sound, and non-zero piezoelectricity. This means mechanical excitations generated at the nanoscale or macroscale can be efficiently driven for micro electro-mechanical systems (MEMS) [53,54]. This last point makes SiC an attractive candidate for hybrid quantum systems containing mechanical resonators.

3.1.1 The SiC lattice

The SiC crystal structure can be organized into bilayers, or planes, consisting of an equal number of silicon and carbon atoms. This bilayer is the most energetically stable configuration but the way

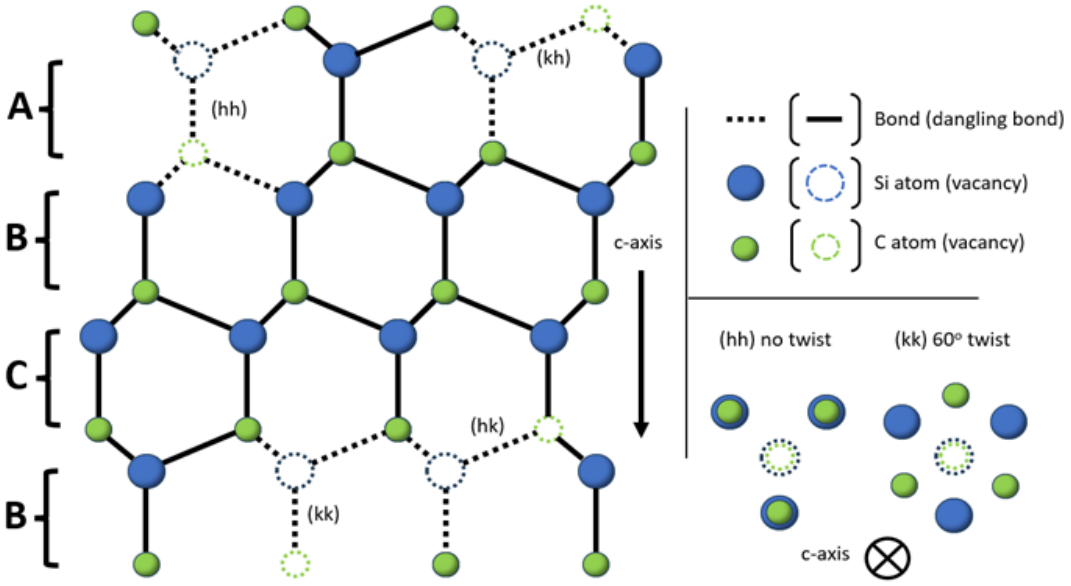

Figure 3.1: **Lattice structure of 4H-SiC.** The ABCB bilayer stacking structure is shown, relative to the c-axis pointing down. The four species of divacancy that can exist due to the hexagonal and quasi-cubic lattice sites are shown as removed atoms with dangling bonds. The 60° twist in the structure present every other bilayer, starting the A-layer containing the (kk) divacancy, breaks the symmetry and leads to the existence of two inequivalent lattice sites.

two bilayers can stack together actually has three possible orientations. Different bilayer stacking order results in different SiC crystal lattice configurations, or "polytypes." If we define the c-axis as the [0001] crystal direction, then Figure 3.1 shows the definition of the three types of bilayer stacking configurations using the 4H-SiC polytype. We label them "A", "B", and "C". The "A" layer is translated to become a "B" layer, and both "A" and "B" can be rotated by 60 degrees around the c-axis to become a "C" layer.

3.2 The divacancy in 4H-SiC

If it is energetically favorable, any of the silicon or carbon atoms can be removed from their lattice sites, leaving a vacancy behind. This can occur at scale when knocked out by high speed electrons or ions. These vacancies can then be coaxed together by making them mobile in the lattice through high temperature anneals. The six dangling bonds from the neighboring atoms are confined and make a localized electronic state. When a silicon and a carbon atom vacancy are adjacent, we can

label the divacancy complex based on its position in the lattice. These complexes have significant energetic barriers preventing them from disassembling, as is the case with other substitutional impurities and complexes. Electron irradiation is the preferred choice for divacancy creation because it can knock out individual atoms and has low structure damage [55]. At 2 MeV, relativistic electron irradiate has a penetration depth on the order of 1 mm [56]. By carefully controlling the dose, the formation of desired defect densities, ranging from sparse single defects to dense ensembles, can be produced on demand in 4H-SiC chips. B_z

Figure 3.1 shows the two possible orientations that there can be a divacancy in 4H, with the four distinct species labeled. The divacancy can be parallel to the c-axis or exist within the bilayer, which we will from now on refer to as the basal plane. The local bilayer stacking leads to four distinct orientations. We use "k" to refer to the quasicubic site and "h" to refer to the hexagonal site. The hexagonal or quasicubic local symmetry results from the particular sequence of bilayers. In this thesis, we use the notation to differentiate the four configurations of divacancies as "xy" where x is the site of the carbon vacancy and y is the site of the silicon vacancy. To further differentiate the divacancy types, the optical transitions within the bandgap for the *hh*, *kk*, *hk*, and kh are labeled PL1, PL2, PL3, and PL4, respectively, where PL = photoluminescence. It will be noted here that there are photoluminescence lines called PL5 and PL6 that have been resolved at room temperature and have similar near-IR wavelength to the four divacancies. These are most likely the result of stacking fault complexes, not vacancies [57]. PL1-4 have been observed to have an excited state lifetime on the order of 13-18 ns, corresponding to a lifetime-limited linewidth of approximately 10 MHz [40].

The main distinction between the c-axis divacancies, hh and kk, and "basal" plane divacancies, hk and kh, is that the lower crystal symmetry of the basal divacancies leads to many

differences in the shapes of the orbitals that contain the electrons donated from the six neighboring atoms. Density functional theory (DFT) is concerned with defining and elucidating these orbitals. We borrow language from DFT when defining the divacancy's level structure, which has been explored in great detail due to similar symmetries as the divacancy complex describing the nitrogen vacancy center in diamond [58]. The symmetry group that defines the basal divacancies is C_{1h} while the c-axis is described by the higher symmetry C_{3v} group. These classifications from group theory define the rotation symmetries allowed, e.g. $3v$ for three vertical reflection planes and $1h$ for only one horizontal reflection plane. This lower symmetry for the basal divacancies leads underpins the results discussed in Chapter 5 We will need to define the language of the divacancy Hamiltonian and optical fine structure next.

3.2.1 Spectral emission features

Regardless of the configuration of the divacancy that is optically excited, the radiative decay to the ground state can unfortunately span a wide range of NIR wavelengths. This leads to two main features in the optical spectrum for divacancies of a sharp zero-phonon line (ZPL) corresponding to the direct, radiative decays between the ground and excited states and a much broader phonon side band (PSB) due to red-shifting of the light occurring by corresponding emission of phonons into the bulk 4H-SiC. ZPL wavelengths exist between ~1078-1132 nm with the PSBs slightly shifted to ~1100-1400, as measured in [41]

The characterization of the percent of ZPL emission one can expect from a divacancy is the Debye-Waller factor (DWF), which is a critical factor for utilizing solid-state spins as entanglement generation due to the requirement of frequency-indistinguishable photon generation from optically active qubits at different times or in from different places to perform photon interference. [9]

Divacancy DWF are typically in the range of ~5-10%, which varies for each of the configurations [40,59]. Estimating DWF for a given crystal defect is non-trivial. Yet, enhancing the percentage of emitted light at the ZPL of a divacancy can be enhanced by coupling the divacancy electric dipole to an optical field cavity. When the cavity resonance is matched with the ZPL, there can be an increase in the emission rate due to the Purcell effect, a feature that we will explore in Section 6.3.4.

3.2.2 Divacancy electronic structure

When a divacancy forms, the electrons that were bonded to the now missing atoms form a new complex that acts like an artificial atom with new electron orbitals. Four of the electrons pair up in orbitals and do not have an intrinsic magnetic moment. These four do not interact with external fields so we can neglect them in the following treatment. The two unpaired electrons can occupy two energetically equivalent orbitals, so they can exist in four total states, either with spin, $S = 1$ or $S = 0$. The states that have nonzero spin are called the triplet states and the one state with zero spin is the singlet state.

We follow the nomenclature for the quantum mechanical spin numbers S and m_s to define the spin and spin magnetic numbers respectively. For an electron, s is simply its intrinsic value of spin angular momentum, being $S = \frac{1}{2}$. Then its magnetic quantum numbers associated with the electron's total angular momentum z-axis projection is $m_s = \pm\frac{1}{2}$. A state for the total spin system is written $|S, m_s\rangle$ where the state of an electron will be truncated as spin-up or spin-down:

$\left|\frac{1}{2},\frac{1}{2}.\right\rangle \rightarrow |\uparrow\rangle, \left|\frac{1}{2},-\frac{1}{2}.\right\rangle \rightarrow |\downarrow\rangle$. For the two electron system, we have $m_s = \pm 1,0$. There are four allowed states for this configuration, written as:

$$\begin{aligned} |1,1\rangle &= |\uparrow\downarrow\rangle \\ |1,0\rangle &= \frac{1}{\sqrt{2}}(|\uparrow\downarrow\rangle + |\downarrow\uparrow\rangle) \\ |1,-1\rangle &= |\uparrow\uparrow\rangle \\ |0,0\rangle &= \frac{1}{\sqrt{2}}(|\uparrow\downarrow\rangle - |\downarrow\uparrow\rangle). \end{aligned} \tag{3.1}$$

The three states with total spin, $S = 1$, represents the antisymmetric triplet states, while there is one symmetric singlet state that has $S = 0$. Within the divacancy orbitals, the triplet state is stable due to the antisymmetric spin-spin interactions being energetically favorable. This is the manifold that qubit control will be done within. The singlet configuration is only metastable but is accessible by way of optical excitation of the triplet state and allows "resetting" of the triplet spin state that helps enable initialization of the qubit (see Section 3.3.1).

Having defined the allowed spin states of the divacancy in 4H-SiC in its optical groundstate, we now begin defining its interaction with external fields. The interactions we will include in the Hamiltonian are interactions with electromagnetic fields and other spins present in the crystal. Our total Hamiltonian operator, H_{tlt}, takes the form:

$$H_{tlt} = H_{ZF} + H_{Elec} + H_{Zeeman} + H_{HF}. \tag{3.2}$$

H_{ZF} is the zero-field Hamiltonian, defined as the contribution from the two electron spin's dipolar spin-spin interaction. H_{Elec} is from AC or DC electric field drives. H_{Zeeman} is similar and describes the effects from magnetic field drives. H_{HF} describes the hyper-fine interactions from non-zero nuclear spins near the divacancy.

3.2.3 Groundstate Hamiltonian

To begin defining H_{ZF}, we need the Pauli spin matrices for $S = 1$ systems, which makeup the full vector, $\hat{S} = [\hat{S}_x, \hat{S}_y, \hat{S}_z]$:

$$\hat{S}_x = \frac{\hbar}{\sqrt{2}}\begin{pmatrix} 0 & 1 & 0 \\ 1 & 0 & 1 \\ 0 & 1 & 0 \end{pmatrix}, \hat{S}_y = \frac{\hbar}{\sqrt{2}}\begin{pmatrix} 0 & -i & 0 \\ i & 0 & -i \\ 0 & i & 0 \end{pmatrix}, \hat{S}_z = \frac{\hbar}{\sqrt{2}}\begin{pmatrix} 1 & 0 & 0 \\ 0 & 0 & 0 \\ 0 & 0 & -1 \end{pmatrix}. \tag{3.3}$$

Now we write the zero-field Hamiltonian explicitly:

$$H_{ZF} = \hat{S} \cdot \widehat{D} \cdot \hat{S}.. \tag{3.4}$$

The zero-field splitting tensor $\widehat{D}$ has components D_{ij}. We can simplify it to a diagonal matrix given the fact that that $\widehat{D}$ is diagonal and traceless in this basis for, so we write:

$$\widehat{D} = \begin{pmatrix} D_x & 0 & 0 \\ 0 & D_y & 0 \\ 0 & 0 & D_z \end{pmatrix}. \tag{3.5}$$

Where above we defined the components of the matrix in terms of the diagonal tensor components, $D_{ii} = D_i$. And we set $\hbar = 1$ for compactness. By expanding and collecting like terms we write:

$$\begin{aligned} H_{ZF} = \hat{S} \cdot \widehat{D} \cdot \hat{S} &= \begin{pmatrix} \frac{D_x}{2} + \frac{D_y}{2} + D_z & 0 & \frac{1}{2}(D_x - D_y) \\ 0 & D_x + D_y & 0 \\ \frac{1}{2}(D_x - D_y) & 0 & \frac{D_x}{2} + \frac{D_y}{2} + D_z \end{pmatrix} \\ &= \begin{pmatrix} \frac{1}{2}(D_x + D_y - D_z) + D & 0 & E \\ 0 & D_x + D_y & 0 \\ E & 0 & \frac{1}{2}(D_x + D_y - D_z) + D \end{pmatrix} \end{aligned} \tag{3.6}$$

Where for the last step, we use the established convention to define a longitudinal and transverse zero field splitting (ZFS): $D = \frac{3}{2}D_z$ and $E = \frac{1}{2}(D_x + D_y)$, respectively [60]. The magnitude of these two parameters has a significant impact on sensitivity of the divacancy's energy levels to perturbing fields, as we will see in the results presented in Chapter 5 Defining these two quantities allows us to simplify the Hamiltonian, up to a constant energy shift, as:

$$H_{ZF} = D\left(S_z{}^2\right) + E\left(S_x{}^2 - S_y{}^2\right). \tag{3.7}$$

If we solve for the eigenvectors after solving the time-independent Schrödinger equation, we obtain three states for the spin system and their corresponding energies defined by the ZFSs:

$$\begin{aligned} |0\rangle, E_0 &= -\hbar\frac{2}{3}D \\ |+\rangle = \frac{1}{\sqrt{2}}(|+1\rangle + |-1\rangle), E_+ &= \hbar\left(\frac{1}{3}D + E\right) \\ |-\rangle = \frac{1}{\sqrt{2}}(|+1\rangle - |-1\rangle), E_- &= \hbar\left(\frac{1}{3}D - E\right). \end{aligned} \tag{3.8}$$

Now we can look at the energies of this Hamiltonian to get intuition about the zero-field tensor. It can be explained as the interaction energy of the triplet states where we lift the degeneracy between the states with $m_s = \pm 1$ with the state with $m_s = 0$. These are separated by the longitudinal ZFS, D because for divacancy systems, $D \gg E$. This will be important as we will normally chose $m_s = 0$ and one of the magnetic excited states as our qubit levels. The states $m_s = \pm 1$ are also split by the transverse ZFS E. Importantly, we also see that the triplet states are no longer the spin eigenbasis, instead we have mixed states $|+\rangle$ and $|-\rangle$. This will be very important in Chapter 5 when we investigate how to exploit this level structure to show an enhanced coherence of the *kh*

divacancy by adding an AC microwave drive between $|+\rangle$ and $|-\rangle$. It is the reduced symmetry of the basal divacancy adding strain to the Hamiltonian that results in the off-diagonal E terms of Eq. (3.6) being large enough compared to D for basal divacancies [25] that the zero-field splitting plays a large role in its spin dynamics.

3.2.4 Response to electric fields

It has been observed that electric field vectors $\vec{F}$ modify the zero-field Hamiltonian curves [24], which due to our definitions in the previous section, we can write the contributions to the LZFS and TZFS due to electric field components parallel, $F_{\parallel}$ and perpendicular, $F_{\perp}$ to the magnetic dipole:

$$H_{Elec} = D_{elec}\left(S_z{}^2\right) + E_{elec}\left(S_x{}^2 - S_y{}^2\right) \\ D_{elec} = d_{\parallel}F_{\parallel}, E_{elec} = d_{\perp}F_{\perp} \tag{3.9}$$

Where the d's are the parallel and perpendicular Stark-coupling parameters to the divacancy ground-state spin.

3.2.5 Response to magnetic fields

The Zeeman interaction term differs in its dependence on the Pauli spin operators, so we will see a marked difference in how magnetic fields couple to the divacancy. For electron spin systems, we can write:

$$H_{Zeeman} = \mu_B \hat{g} \cdot \hat{B} \cdot \hat{S}. \tag{3.10}$$

Here μ_B is the Bohr magneton constant for the electron, $\hat{g}$ is the ground-state electron g-factor tensor (both are ~2 for the divacancy complex), and $\hat{B}$ are the magnetic field components.

Expanding in component form, we write:

$$H_{Zeeman} = \mu_B\left(g_{\parallel}B_{\parallel}\hat{S}_z + g_{\perp}B_{\perp}(\hat{S}_y + \hat{S}_z)\right) \tag{3.11}$$

Now we can make several comments on the response of the divacancy groundstate spin to electromagnetic fields. Starting with magnetic fields, the Zeeman interaction leads to large shifts of the spin energy levels, on order of $\mu_B\hat{g} \sim 30$ GHz/T. This has pros and cons, as always is the case for quantum systems. On one hand, this allows sinusoidal magnetic fields to perform fast, coherent Rabi oscillations of the spin population, but on the other hand, magnetic noise threatens to decohere the qubit through energy level fluctuations. The upside is that the when the ZFSs, are larger than the magnitudes of the noise, the system is quantized by either ${S_z}^2$ due to the presence of D or ${S_z}^2 + {S_x}^2 - {S_y}^2$ due to the presence of E, see Figure 3.2. Non-commuting operators cannot affect the Hamiltonian energies to first order, so what results is an insensitivity to the magnetic field components in $\hat{B}$. This effect is larger the larger D and E are. For the four species of divacancies, D does not change by much, but for the basal divacancies, $E \sim 32$ MHz scale while On the left, c-axis divacancies have negligible E. This large E adds insensitivity to all components of $\hat{B}$, making the basal divacancy an attractive qubit due to a well-protected spin state. Electric fields enter the picture when operating in a regime with negligible $\hat{B}$, and the quantization means E now effects the energy levels to first order. The basal divacancies are well-positioned to show this effect given the large susceptibility to transverse electric fields [24]. Where electric fields shine is their ability to drive normally forbidden $\Delta m_s = \pm 2$ transitions when E is changed in time

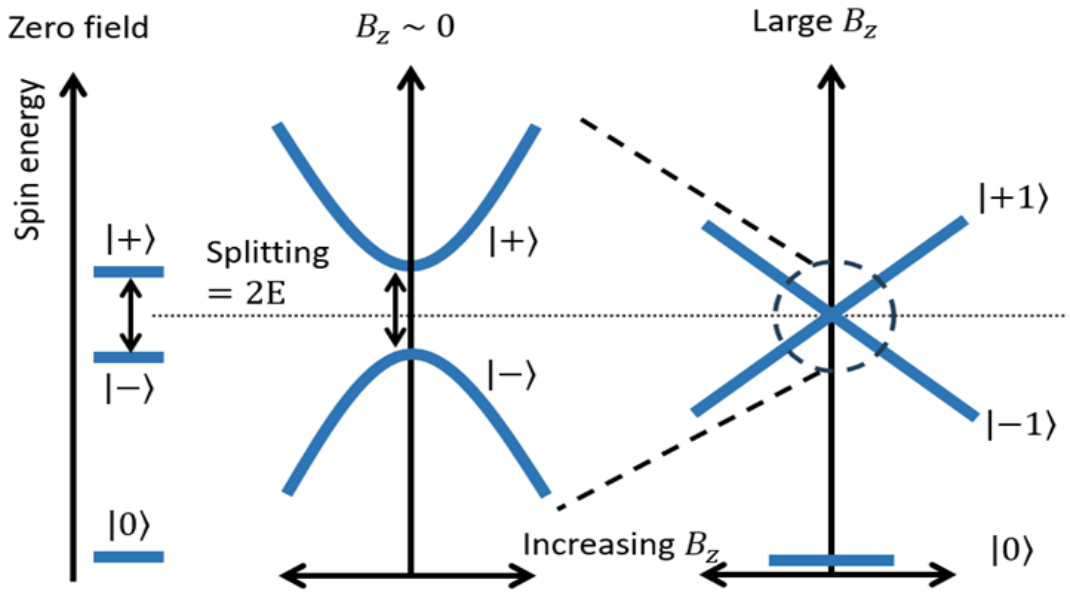

Figure 3.2. **Spin energy dispersion for *kh* divacancy.** On the left, we see the zero field spin states for the kh divacancy with their degeneracy broken by the presence of the transverse ZFS in the Hamiltonian. For small applied B_z (center), the energy dispersion is dominated by the $E\left({S_x}^2 - {S_y}^2\right)$ term, so we maintain the mixed character of the spin basis, $|\pm\rangle$. This regime has high-protection from magnetic fluctuations due to the quadratic dependence, and the avoided crossing is called a clock transition. As B_z increases in magnitude (right), the Zeeman term, $\mu_B \hat{g} \cdot \hat{B} \cdot \hat{S}$, dominates, leading to unmixing of the basis, returning to the $m_s = \pm 1$ basis and increased sensitivity to magnetic noise due to linear dispersion.

by AC electric fields. One last thing to note is that temperature effects on the divacancy ground-state spin are realized through the electric coupling term also inducing changes in D and E [41].

3.2.6 Response to nuclear spins

The hyperfine contribution to the Hamiltonian is the most unwieldy due to it not having a closed form that can capture the extent of every species coupling to a divacancy. The term can be written down as an infinite sum of the magnetic moments, $\hat{I}_n$, of the nuclear spins and corresponding hyper-fine coefficients, $\hat{A}_n$:

$$H_{HF} = \sum_n \hat{S} \cdot \hat{A}_n \cdot \hat{I}_n. \tag{3.12}$$

To understand this, we must introduce the concept of the "nuclear spin bath" or just "bath" for short. Those nuclei with non-zero spin located both near to and far from the divacancy can couple to the Hamiltonian at various degrees of interaction strength. In certain circumstances, this effect can be averaged and represented by a classical magnetic field noise term and the basis states of the nuclear spins are not used. In other cases, a single nuclear spin is so close, maybe even the neighboring atom, to the divacancy that its spin states can be treated coherently. This will not tell the whole story though of the remaining collection of nuclear spins and it requires powerful theoretical tools to describe the effects of the bath.

3.3 Optical fine structure

Having laid the groundwork of how the spin energy levels of the divacancy in its optical ground-state can change, we now consider the effects of optical excitations. Due to the presence of an optical dipole for the divacancy structure, certain wavelengths of light in the near-infrared (NIR) can yield a spectrum of photoluminescence that is different for every configuration of the divacancy. The exact wavelength resonant with a particular defect depends on the local environment and how it interacts with the occupied spin triplet orbitals in the ground and excited state. The energy differences between those states reveals an optical fine structure that will influence how we readout our spin qubit using pulses of tunable, narrow-line NIR lasers.

The c-axis divacancies share their excited state fine structure with that of the nitrogen vacancy center complex in diamond, resulting from their shared C_{3v} symmetry group. There are six spectral lines from the orbital doublet spin triplet levels having their degeneracy lifted by the local electric field. These fields are due to the specific crystal strain at the location of the defect and the existence of nearby trapped TLSs, or from applied fields from fabricated electric leads for deterministic tuning. The most useful character of the divacancy fine structures is the spin-

conservation of the optical transition between the ground and excited state orbitals. Taking advantage of this allows deterministic readout of the spin state of the groundstate.

We will focus on the kh configuration now as it will be the defect studied in the results of Chapter 5 The *kh* divacancy is also theoretically understood to have an excited state doublet [25,58] due to the broken symmetry of its crystal lattice position that leads to internal applied transverse strain, shown in Figure 3.3. Experimental evidence for the second, higher energy excited state is hard to measure and has not been reported even now. One explanation for this lack of observation is that excitations that enter higher orbital undergo rapid internal conversion through non-radiative decay that cannot be easily observed by other spectroscopic or electrical means. Thus, for the *kh* divacancy, only three optical lines are seen for all practical experiments. We focus this section on the lower energy excited state, which gives us the means to prepare the ground-state spin into an arbitrary superposition state as well as deterministically read the state out. Experimental details of these processes will be explained in detail in Chapter 4 Another notable fact about the *kh* defect fine structure is that the optical selection rules means the three spin states for *kh* divacancies are excited by linearly polarized light [58,61] which is in contrast to the c-axis class of divacancies where circularly polarized light excites the $m_s \neq 0$ character spin states.

Much of the theory on the ground-state triplet manifold applies to the excited state, which we borrow the convention from DTF and label A' (the higher energy excited state is labeled A''), and the equation for the Hamiltonian in the ground-state, Eq. (3.8), holds as well. What this means is that the mixed spin basis, $[|+\rangle, |-\rangle, |0\rangle]$, can define the spin states of the electrons in the ground-state as well as the excited state. This gives the *kh* divacancy spin state a chance to remain unchanged after emitting an optical photon (Figure 3.3B), which is very useful for preparation of the spin state before attempting to perform qubit rotations in the groundstate. If there are moderate

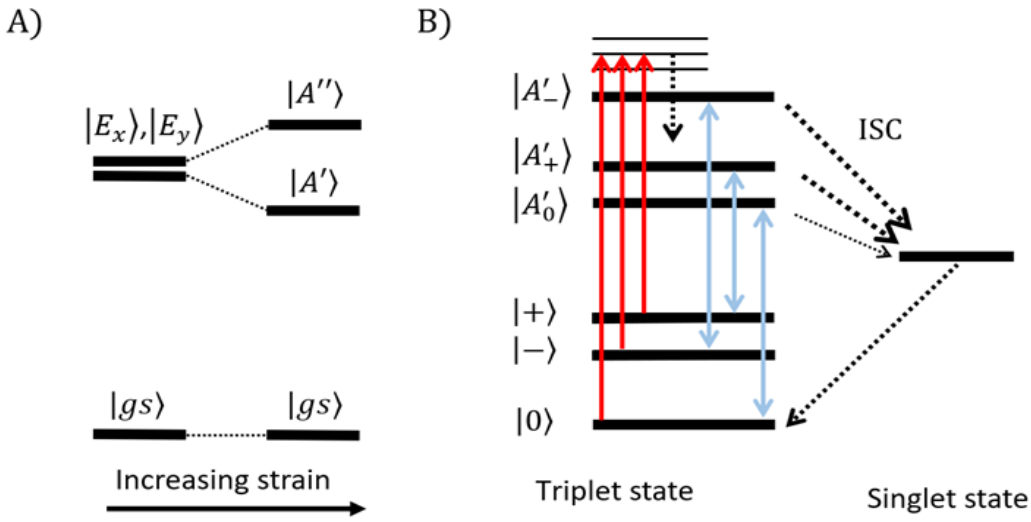

Figure 3.3. **Optical fine structure of *kh* divacancy and spin initlization.** A) The excited state doublet of the optical structure of the divacancy, $|E_x\rangle$ and $|E_y\rangle$ splits under strain into $|A'\rangle$ and $|A''\rangle$. The ground-state, $|gs\rangle$ remains unperturbed. B) Expanding to show the spin-triplet of the addressable optical states of the kh divacancy, $|gs\rangle$ and $|A'\rangle$. Red arrow shows off-resonant excitation from within the groundstate levels that do not conserve spin after non-radiative relaxation (dashed, black arrow) into the optical excited states. Light blue arrows denote the spin-conserving resonantly addressable transitions. Other non-radiate transitions that couple the excited states with the singlet state through the ISC. Thickness shows the $m_s = 0$ state, $|A'_0\rangle$ couples less strongly to the ISC. A spin state can be prepared into $|0\rangle$ by off-resonantly addressing the ground-state, which over time loses $m_s \neq 0$ character spin states on average due to them non-radiatively relaxing through the ISC.

magnetic fields present, the eigenbasis of the excited state can shift and alter the selection rules and spin mixing can be induced upon optical excitation. This degradation of the spin projection would be measured as an energy relaxation effect in the spin readout measurement and should be avoided by working at low magnetic fields.

3.3.1 Optical spin-initialization

Now we will discuss the mechanisms of utilizing the divacancy's optical structure to prepare, or initialize, a specific quantum spin state and then measure, or readout, that spin state deterministically. This technique underpins all the qubit manipulations concerning the divacancy system in this thesis, including Ramsey and Hahn measurements of the coherence of said qubits.

If we want to do an ensemble of experiments, we want to say with some confidence that the spin begins in, say, the $|0\rangle$, where this state is for the ground-state. It so happens that upon excitation with off-resonant light (905 nm for *kh* divacancies), there exists a decay pathway through non-radiative transitions through the singlet states where we see preferential decay into the $|0\rangle$ ground-state after many cycles. This intersystem crossing (ISC) is a well-studied feature also found in the nitrogen vacancy center literature. [62,63] This preferential decay has a contrast of a few percent for divacancies [39]. The off-resonant light critically excites from any of the three spin ground-states, so we do not to have prior knowledge of the spin state to begin an experiment. After a certain number of excitation cycles, the spin population is, to some increasing percentage, found in $|0\rangle$. (Figure 3.3B) This is what we call high-fidelity spin initialization, where fidelity in this context describes the percentage of a population of quantum states prepared in the desired state. Fidelities up to 94% have been achieved by using purely off-resonant excitation [40]. Usage of resonant excitation with tunable, narrow-line lasers can offer better signal-to-noise ratios overall and is generally considered the better choice for addressing the spin-selective optical transitions of the basal divacancy. It allows the mapping of the exact energies of the optical fine structure of the *kh* divacancy [25] Choosing to address just one of the transitions to excite at a time means that the spin population in that level (or lack thereof) can attempt to be measured without worrying about addressing other levels.

Chapter 4

EXPERIMENTAL METHODS FOR SPIN MEASUREMENTS

4.1 Introduction

This chapter describes the experimental equipment and methods used to measure the properties of single divacancies using optical and microwave photon sources while shielding them from unwanted electromagnetic noise and thermal gradients. The goal is to describe the various apparatuses of this setup in a piece-wise fashion to elucidate the technical details of obtaining quantitative data describing the operation of a spin qubit. Several times we will also take a step back to consider best practices to decrease the effect of noise sources when combining the different subsystems.

We will begin with a description of the cryostat system used to maintain a 4 K environment around the SiC chip. and the factors to consider when coupling in diffraction-limited NIR laser light and coherent microwave signals at cryogenic conditions. This will lead into a discussion on both of those subsystems to describe how the raw data from the defect's optical emission can be recorded and used to characterize the electron spin qubit.

4.2 Cryogenics

At ambient conditions, the chips of SiC that house divacancies at densities that allow addressing of single defects will only show broad features dominated by photoluminescence from many other

photoactive species when addressed by off-resonant light. Only at cryogenic temperatures below 5 K does the high-fidelity optical interface of the divacancy become the dominant generator of photons at their optical wavelengths. We thus place our SiC chips inside a closed-cycle helium cryostat (Cryostation s100, Montana Instruments) which uses the Gifford-McMahon cryocooler architecture to extract heat from the sample by pressurizing and expanding helium gas. The heated helium transferred into a chiller pump that enables heat exchange with cold water that is then pumped away to expel heat elsewhere. Heat is ultimately absorbed inside the cryostat using a "cold finger" or copper piece that the sample holder comes into contact with inside the vacuum chamber. Copper is chosen for its excellent thermal conductivity. The heat to be exchanged includes the latent heat exchange with the environment outside the insulated cryostat as well as any radiation we must input into the chamber to address the divacancy.

The cryostat's cooling power defines the thermal budget we have for our experiment, which can easily be overwhelmed. That budget is defined by the degree of thermal isolation the the cryostat can provide from the ambient conditions. There are two main components for our cryostat: an outer metal shroud that creates a vacuum chamber and an inner radiation shield. We use a two-stage pump system composed of a diaphragm and turbomolecular pump to reach pressures < 50 mTorr to minimize the rate of convective heat transfer. A good physical seal is necessary to establish vacuum, which is achieved using a rubber O-ring with a thin coating of grease. Radiative heat transfer from the sample directly seeing the vacuum shroud is steeply reduced by the aluminum inner enclosure that reflects in the infrared spectrum. Typically, this shield sits at around 30 K. These enclosures provide ideal operating conditions for the cryostat to start removing heat using the gas-exchange loop and undergo cryocooling. Typically, we maintain

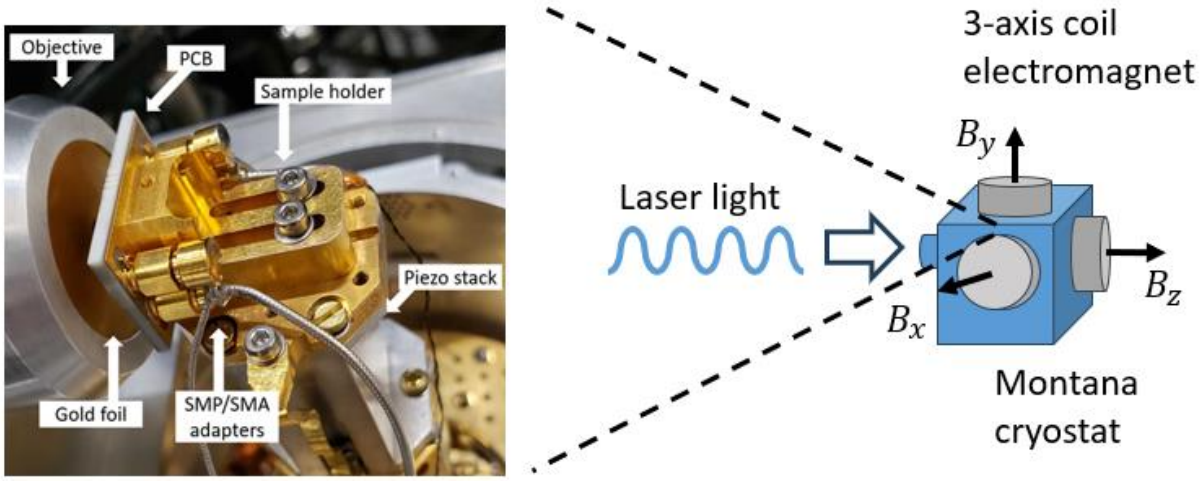

Figure 4.1. **Cryogenic mounting adapter and electromagnet.** Shown here (left) is the back view of a sample mounted inside the 4K cryostat. The laser light enters the cryostat through the objective (left) and through the ultra-thin gold foil, which minimizes as much as possible extraneous radiation from impinging on the sample. The PCB is mounted on a gold-plated L-bracket screwed to the piezo stack anchored to the cold finger. Microwave photons can be sent to the sample through wire bonds connected 4 ports that lead to SMP/SMA couplers. The sample mount sits inside the Montana cryostat (right) with optical access. This diagram shows how the cryostat chamber (blue) is surrounding by three electromagnet coils (grey) that can provide vector-magnetic field sweeps discussed in Section 4.6.7 and Chapter 5 The z-axis is defined as the travel direction of the lasers.

the turbo pumping until the base operating temperature is reached in around 4 hrs. or even during the whole course of the experiment to remove trace contaminants from outgassing in the sample chamber. Outgassing is the process of trace gas particles being initially trapped inside materials and cannot be pumped out, but later leak out slowly over time. These contaminant gasses then can rapidly cool at cryogenic temperatures and land on the sample to become a potential source of optical scattering or degradation of performance of the microwave lines.

To have optical and microwave photon access to the sample, the thermal insulation is necessarily compromised in two places. The first is a series of SMA-SMA coaxial wire feedthroughs mounted on the side of the cryostat. There is a second stage of SMA connectors outside of the vacuum shroud to minimize the risk of unscrewing them compromising the integrity of the chamber itself. The second input is an optical port cut in the vacuum shroud with an anti-reflection coated window to maximize two-way transmission of the wavelengths of interest while

suppressing other wavelengths entering the cryostat chamber. The few-millimeter thick window is necessarily at ambient temperature and pointed directly at the sample through a microscope objective (LCPLN100XIR, Olympus). The solid angle of ambient radiation shining through the objective is minimized by mounting an ultra-thin gold foil annulus between the objective and the sample.

The last element of the cryogenic system to discuss is the physical mounting of the sample to the cold finger. We need to be able to move our sample inside the cryostat, so we mount the sample holder to a 3-axis nano positioner piezo system. The design of the piezo stack includes thermally conductive ribbons that bypass the stages that act as insulating blocks. The sample holder itself is designed for maximum thermal conductivity. The sample is secured by about a toothpick's diameter of adhesive paste applied directly to a copper block screwed to an adapter on the piezos. Around the copper block is a custom-printed PCB board with SMP coaxial interfaces that connect to the SMA wires mentioned above. The direct thermal link through low-thermal insulation copper from the sample to the cold finger helps to minimize the total heat load on the sample.

4.3 Optical apparatus

The optical path of the setup contains a number of subsystems that each play a crucial role in shuttling the light from laser outputs to the sample under study in the cryostat. Great care must be utilized to maximize the signal to noise ratio during each type of experiment used to characterize the defect's differ properties The experiments themselves will be explained in a later section, but first we must describe the subsystems, of which there are six.

The most important function of each subsystem is now mentioned to give an overarching idea of the setup. 1) The lasers generate photons that must have the right frequencies and be sent at the right times to accomplish qubit population driving. 2) Photons from the different lasers must

be overlapped into a single beam and have the right polarization and power to address the divacancy's optical dipole efficiently. 3) This beam must be focused to a diffraction-limited spot to resolve single divacancies and be translatable for raster scans of the surface. 4) The photons emitted by the defect's phonon sideband must be collected at high-efficiency while blocking photons at the frequency of the lasers and undesired other emitters in SiC. 5) These collected photons must be counted at high efficiency to produce accurate count rates.

All five of these subsystems sit on a pair of adjacent optical tables in our laboratory, save the photon counter housed in a thermally controlled closet. The mass of the stainless steel tables act as the primary mechanical dampener for our experiment, helping to reduce the fluctuations of the optical beam path from foot traffic in the lab. Here it is useful to note our lab is located two stories underground to add a degree of passive atmospheric stability to supplement the building's active systems, further mechanical isolation from the university vehicular phonon noise-scape, and shielding from communication technology radiation.

4.3.1 Lasers and laser controls

This first subsystem, diagramed in Figure 4.2, contains the two different laser excitation sources, one 905 nm laser (QFLD-905-200S, QPhotonics) and a tunable laser (DL pro, TOPTICA Photonics). Also included are the necessary instruments to calibrate and observe the spectral quality of the tunable resonant laser. What outputs from this subsystem are the two beams in different single mode fibers sent to the main free-space optical setup that makes up the excitation and collection paths.

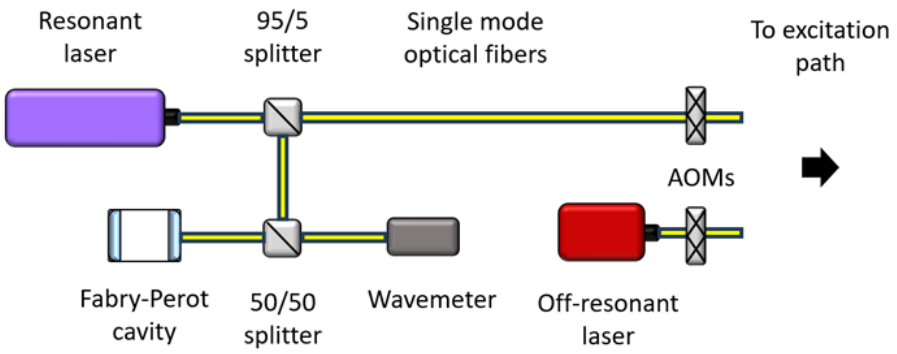

Figure 4.2. **Laser control diagram.** Shown here are the components that make up laser control subsystem. Fiber beams splitters pick off an adequate amount of light to send to the characterization Fabry-Perot cavity and wavemeter. Both lasers are fiber coupled to single-mode fibers and sent to the excitation path of the confocal microscope (Figure 4.3).

We use the 905 nm laser to accomplish several tasks. This laser can illuminate all species of defects for characterizing the density of emitters in new samples. Its main role is to provide off-resonant spin initlization and can also stabilize the defect in the neutral charge state. A resonant readout pulse is then used to readout the spin state. The off-resonant power was set to 350 mW and the controller has active thermal feedback. The power at which we address a single defect can vary by a few orders of magnitude when optimizing for signal to noise ratio, but typical off-resonant powers reaching the sample are in the 1-100 mW range. The 350 mW overhead helps recoup losses from other optical components.

The tunable diode laser system produces photons in the range of 1068 to 1140 nm for the optical resonance characterization and spin state readout of *kh* divacancies. The actual wavelength range the PL4 optical signals were normally found in the sample studied is better expressed in frequency, being a ~150 GHz wide region beginning at ~277.95 THz. The powers needed to reach the sample are much lower given the resonant condition, where powers below 1 mW are typical. The number of control elements used for tuning and active stabilization at a particular resonant wavelength to within ~10 MHz takes a large power overhead, so power efficiency in all components and optical fiber connections is paramount. Our resonant laser has a linewidth of a

few Hz and a widely tunable range, but care has to be taken to produce single mode light from it. Below we outline the two main instruments underpinning this process.

The resonant laser output is coupled into a single mode optical fiber with low loss and a percentage of that light is picked off and sent to a commercial wavemeter (Bristol 671) to measure its wavelength precisely. The device gives a digital reading calibrated to single Hz precision on a repetition cycle of a few milliseconds. The actual measurement is done using Fizeau interferometry where the interference fringes of the wavelength under test is compared to those of a fully internal HeNe laser. The wavemeter can give false readings if the input light is multimode, which can be off by only a few percent and can thus look real.

The instrument we use to observe the mode quality of our laser is a high-finesse, linear Fabry-Perot interferometer. (Optical cavities are discussed in greater detail in Chapter 5 One mirror is attached to a linear piezo motor such that it can quickly sweep over several free spectral ranges (FSRs) of the cavity. A single mode laser beam, whose linewidth is basically constant across all wavelengths, shows up as a set of equally bright peaks separated by the FSR. This spectrum can indicate that the resonant laser's output is multimode if extra, smaller peaks are observed and must be adjusted before the experiment can continue.

The final major part of the laser subsystem is the acousto-optic modulator (AOM), which can produce time-gated laser pulses by deflecting the laser beam upon receiving a microwave signal. This device gives us a way to "flip the switch" for laser beams when producing pulse sequences for initialization and readout of the spin state of the qubit. There are certain crystals with indices of refraction that can change upon applying surface acoustic waves at certain resonance conditions. We operate in the orientation that applying a pulse to the AOM deflects the beam into the main optical path, leaving the non-deflected beam incident on an optical absorber.

Recalling the power overhead requirements for the resonant laser, using the AOM in this orientation reduces the beam intensity by a few dBm, but removes the chance of accidental laser exposure. The tens of nanosecond switch time for the AOMs matches up well with the optical dynamics of the divacancy. It should be noted that insufficient extinction of laser light resonant with the divacancy can be observed as spurious signal. In this experiment, a single AOM with extinction ratio ~45 dBm was sufficient to realize a high enough on/off ratio for the pulse sequences.

The full method of tuning the resonant laser, using the instruments described in this subsystem, to a particular wavelength that matches the optical transition of a divacancy is quite involved. The goal is to be able to obtain operation at a specific wavelength such that one can take small steps of a few MHz at a time and maintain single-mode spectral operation at each point. This is needed for the most demanding experiment with the laser, taking photoluminescence excitation spectra (PLE, described in 4.6.2). The difficulties arise in finding the optimal values for three parameters of the laser: the piezo motor position that define the broad wavelength tuning and the diode voltage and current that define the spectral quality at a certain motor position. The exact wavelength and spectral mode quality needs to be monitored over time while still minimizing the total experiment time. Maintaining accurate laser frequency and mode quality throughout the experiment is very important to not introduce large errors due to unrecorded drifts in the optical power addressing a specific spin-dependent optical line.

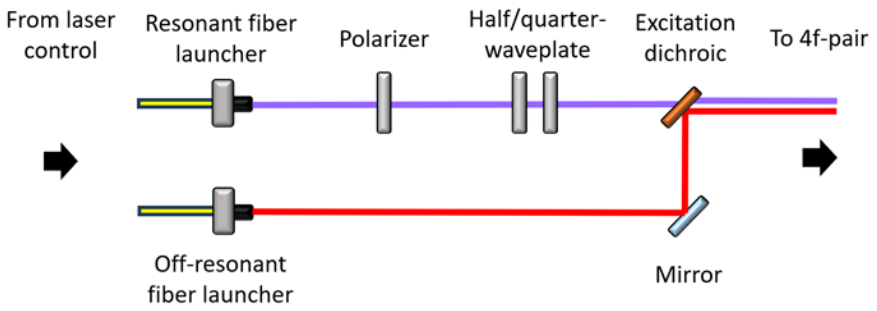

Figure 4.3. **Excitation path diagram.** Shown here are the components that make up excitation path entering from Figure 4.2. After polarization cleaning and assignment of the resonant laser, the resonant and off-resonant beams are co-aligned using the excitation dichroic before being sent the 4f-pair and the cryostat (Figure 4.3).

4.3.2 Confocal microscope: excitation path

After laser light from our sources is sent through single mode fibers into two different fiber launchers, we send the beams into our home-built confocal microscopy setup. The entire confocal setup will be presented as three different subsystems. The excitation path seen in Figure 4.3 uses free space optics to make the different wavelength beams colinear and allows polarization control of the resonant beam.

While commercial laser sources like the two described in the previous section usually have some degree of polarization stability, it is necessary to "cleanse" the resonant laser light as it enters the free-space section. This is also because the AOMs and optical fibers can add polarization drift, which is difficult to correct when not using polarization maintaining fibers and instruments. We use a film-based linear polarizer which gives an output with a degree of polarization along its linear axis over five orders of magnitude better than the incident light.

The fidelity of the linear polarization of the resonant light is important because the light then passes through a set of half- and quarter-wave plates that allow full polarization control when linear polarization is entered. The spatial alignment of *kh* divacancies can have three different orientations when looking along the c-axis, which in our experiment corresponds to the travel

direction of the optical beams. By sweeping the polarization, we can find the angles of the wave plates that give maximum optical readout efficiency. This corresponds with maximizing the overlap between the light's linear polarization angle with the orientation of the single divacancy's optical dipole.

In order to spatially align the off-resonant and resonant optical beams, we utilize a dichroic filter. These are filters that have a wavelength-dependent transmission and reflection spectrum such that we can choose a cut-off wavelength where the majority of the light below that cut-off is transmitted and light above the cut-off is reflected. We choose a 1000 nm as the cut-off of the dichroic. By maneuvering the two beams to be incident on the dichroic, on beam rotated 90-degrees relative to the other, we can overlap their optical modes as one passes through the dichroic and the other reflects off of its surface. The alignment can be adjusted until the transmitted and reflected beams are perfectly co-linear as they head towards the next part of the setup.

4.3.3 4f path

With the excitation laser beams co-linear, it remains to control where on the sample the laser will be incident inside the cryostat. Sending the light through a 4f relay lens pair (Figure 4.4) into a microscope objective allows raster scans of the sample that will reveal bright optical signatures of defects that are spatially resolved due to the diffraction limited, NIR laser spot incident on the sample after exiting the objective. The co-linear beam reflects off a fast steering mirror (FSM) that has voltage controlled tilt angles for its mirror. For an input range of ± 10 volts, we gain the ability of rapid spatial mapping of photoluminescence from our sample in an approximate range of ± 45 microns from where the laser spot is incident with no FSM voltage applied.

Before we discuss the $4f$ lens pair that comes after the FSM, we will discuss the final optical element before the sample itself, the microscope objective. We use a microscope objective

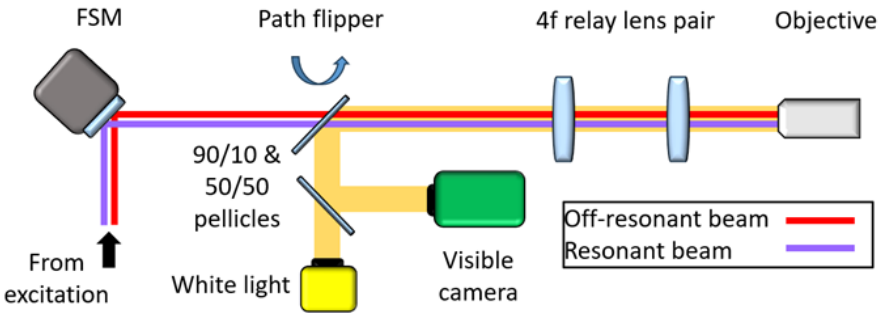

Figure 4.4. **4f path diagram.** Shown here are the components that make up the optical subsystem denoted as the 4*f* path, with beams entering from the excitation path (Figure 4.3). Off-resonant and resonant light enter from lower-left and reflect off the FSM before entering the section containing the 4*f* relay lens pair (not to scale), after which the laser excitation continues to the microscope objective. The path flipper can swing a 90/10 pellicle beamsplitter in and out of the path when we wish to direct white light into the cryostat to illuminate the sample and collect a backscattered image on the visible camera.

(LCPLN100XIR, Olympus) with a high numerical aperture (NA = 0.85)) and high transmission (70%) at the wavelengths of the resonant excitation light. A beam that enters the back of the objective of sufficiently small diameter from the excitation path will produce a diffraction limited spot at a distance away from the objective equal to its working distance. Recalling the thermal constraints of having optical access to our sample, the ~4 mm working distance leads to a tight constraint on the width of the gold reflecting foil that minimizes the unwanted ambient radiation incident on the sample.

The laser beam deflected off the optical axis by the FSM is next sent through a $4f$ configuration. This is the same configuration of lenses used in basic telescopes. In our setup it consists of a pair of lenses with the same focal length f being separated by $2f$, and the point of the angular divergence (the FSM) and the convergence (sample surface, after the objective) must be located f away from either the first or second lens. To first order, it can be shown that the angular divergence upon entering the relay gives translations of the beam focused by the objective.

The above elements allow for observation of the photoluminescence response of the sample surface, but simply having a window into that response function at NIR would make finding a

suitable position on the sample to begin experiments difficult. Especially when utilizing nano-fabricated structures on its surface with small footprints. Conveniently, the $4f$ relay can accommodate colinear white light that reflects off the sample surface and returns through the objective and ends up incident on a visible camera. Then the in-cryo nano positioners can be used to traverse their 5 mm travel range to bring a certain spot on the sample to intersect with the focal point of the lasers.

4.3.4 Confocal microscope: collection path

The next step is to collect the photoluminescence emitted by the defect after excitation by either off-resonant or resonant laser light. The bulk of the work has already been done in our chosen configuration because the emitters acting as point sources overlap with roughly the same optical mode as the excitation light, just with reverse travel direction. To complete the collection path. Figure 4.5, we need a second dichroic that will split off the collected light from the phonon sideband of the *kh* divacancies from the excitation path as well as filters to prevent as much spurious signal from other non-divacancy sources as possible. There is necessarily light also emitted at the ZPL of the divacancy that matches exactly the resonant excitation laser but for the results of this thesis, that light will be filtered out as much as possible as it is a major source of spurious counts.

We choose a dichroic with a cut-off that reflects the excitation light from the resonant laser to the sample but allows the PSB photons to transmit and be fiber coupled into a multimode fiber that is sent to our photon counting instrument covered in the last subsystem.

There remains the choice of filters. The laser light reflected of the SiC surface is still extremely bright, so we must employ a 44 nm notch filter centered at 1064 nm (NF1064-44, Thorlabs) after the collection dichroic that the collection signal passes straight through while the

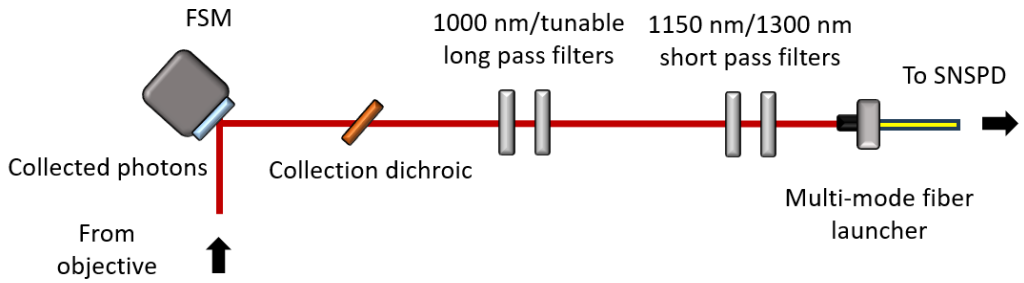

Figure 4.5. **Collection path diagram.** Light collection from the objective returns through the $4f$-pair and reflects off the same FSM mirror, before transmitting through the collection objective (the excitation beam is not shown, but it would reflect off it to go to the cryostat. Then it goes through a series of spectral filters to remove unwanted wavelengths of light that do not carry useful information about the spin population optical contrast experiments explained in Section 4.6.

bright laser reflects off it and towards the objective. Several long pass filters are employed in tandem for most experiments. This includes a 1000 nm and an angle tunable one (TLP01-1116-25x36, Semrock). Short pass filters of 1150 nm and 1300 nm short pass is added to prevent the collection of photons from axial divacancy ZPLs and PSBs, as well as other longer wavelength emitter species.

4.3.5 Photon counting

The last subsystem of the optical setup is concerned with counting the individual photons collected from the sample in the cryostat. This allows us to make quantitative measurements of the emission rate of the divacancy under different experimental configurations. One of the most precise ways to count optical photons is to use a superconducting nanowire single photon detector (SNSPD). Another way is to use an avalanche photodiode, but the NIR emission of divacancies would require the usage of indium-gallium-arsenide detectors that have the necessary bandgap response. These have relatively high “dark counts”, or noise counts during no collecting, and lower collection efficiency than NIR detecting SNSPDs. Collection efficiency is usually called quantum efficiency in the context of photon count and can be, in the case of our SNSPD (SNSPD; Opus One, Quantum Opus), over 80%.

The photons being reflected by the collection dichroic and transmitted through the multitude of filters enters a multimode fiber at the very end of the free space optical setup. Multimode fibers have larger core diameters so they are less stringent about the optical modes they can collect. This is ideal because the emission from a point source defect in the solid-state can vary much more in the spatial extent of its optical mode, especially over the one meter of free-space travel between the sample and the fiber.

The photon to be counted travels a few tens of meters to the closet where the cryogenic system that cools the SNSPD is housed. The nanowire the photons will impinge on is superconducting and cooled to a very precise temperature (in our case ~2.5 K) using a separate closed-cycle helium cryostat. The temperature is precise because the detection of the single photon involves the wire briefly exiting its superconducting state to "go normal". The full theory of superconductivity is complex so we will not go into details, but essentially the photon has the required energy to disrupt the quantum state of the superconducting electron pair states, called Cooper pairs and reduce the current in the device. A classical detection of that current reduction, caused by the energy of a single incident photon, becomes a voltage pulse with an amplitude of around 100 mV, very well handled by typical electronic components. A pulse-converter module takes that voltage pulse and converts it to a higher amplitude of a typical logic pulse (3.3-5 V) and is sent to our data acquisition module discussed that finally can turn the event of detecting a single photon into a number increment in our experimental software.

One point to be aware of when utilizing the SNSPD pulses to count photons is the "dead time" of the detector. Consider the case of two photons arriving at almost the exact same time, separated by Δt. If the first photon leads to a normal response from the nano wire, then the second photon might arrive before there has been time for the wire to exchange thermal energy with the

cryocooler and become superconducting again. A typical pulse length from the SNSPD is on order of 10 ns, so that sets the lower bound of what Δt can be before we start compressing our measured count rate artificially. The count rates from typical divacancy experiments in this thesis are not seen to saturate the detection capabilities of our SNSPD.

The last point about SNSPD operation concerns changing the current in the wire to reduce dark counts while maximizing signal-to-noise ratio from measured photons. The closer the wire is to going normal, the more sensitive the system will be. Every optical system has a certain level of "dark counts" that are incident on the SNSPD path but are not created due to the experiment. Photons leaking into the fiber launcher or other positions are a main culprit. Manually adjusting the current to reduce the sensitivity to all photons can allow a sweet spot to be reached that minimizes dark counts but does not vastly decrease the signal-to-noise ratio of experimentally relevant photons.

4.4 Microwave electronics

This section will include a description of the instruments and passive components that generate and shape the microwave photon pulses that will be used to control the electron spin states of the divacancy for usage as a qubit. In Section 2.6, we derived the equations that described Rabi oscillations in a spin TLS from a sinusoidal drive. We will be generating magnetic and electric fields that can accomplish coherent rotations of the spin qubit populations through on-chip wires lithographically patterned on the surface in close proximity to the divacancies. This is the second main source of thermal load in the experiment, the other being laser heating. We want to be able to place these wires as close as possible to the divacancy under study because resistive heating occurs when we apply a voltage across our device. Using on-chip wires lessens the heat load required to reach a certain drive strength. Much of the microwave architecture is concerned with

sending well-defined pulses, where the degree of control over their amplitude and duration directly corresponds to minimizing the phase errors in the qubit superposition states we create.

There are three main functions of the microwave circuitry. The first is the pulse generation, involving the creation and timing of the microwave pulses and tones at a number of different frequencies. The generated pulses must be shaped using components that amplify, combine, and filter the tones while minimizing the excess noise signals sent to the on-chip components. The final part is in combination with the photon counting apparatus using an SNSPD in Section 4.3.5, we use a pair microwave switches that enable counting only during precisely defined windows during an experiment and to reject common mode noise.

4.4.1 Microwave pulse generation

The central clock that defines the timings of all the electronic pulses in the setup is an arbitrary waveform generator (AWG). It has 16 individually programmable channels that can be used as either TTL (transistor-transistor logic) input or output or as a low-amplitude arbitrary waveform generator. The power of the AWG comes from the very high pulse bandwidth of 2.4 GHz, allowing few nanosecond resolution to shape arbitrary pulses. Arbitrary in this case can be thought of as defining a certain clock speed, say 10 points per microsecond, and at each of those points, we can tell the AWG to produce a TTL output of high or low at each point. This power is multiplied by the 16 independent channels that are synchronized so we can produce a pulse train by combining outputs from multiple channels. The core of the microwave pulse generation for a certain qubit experiment is an AWG sequence. This sequence defines all the electromagnetic drives to be produced, and also controls the AOM on/off states to define the timing of the laser pulses.

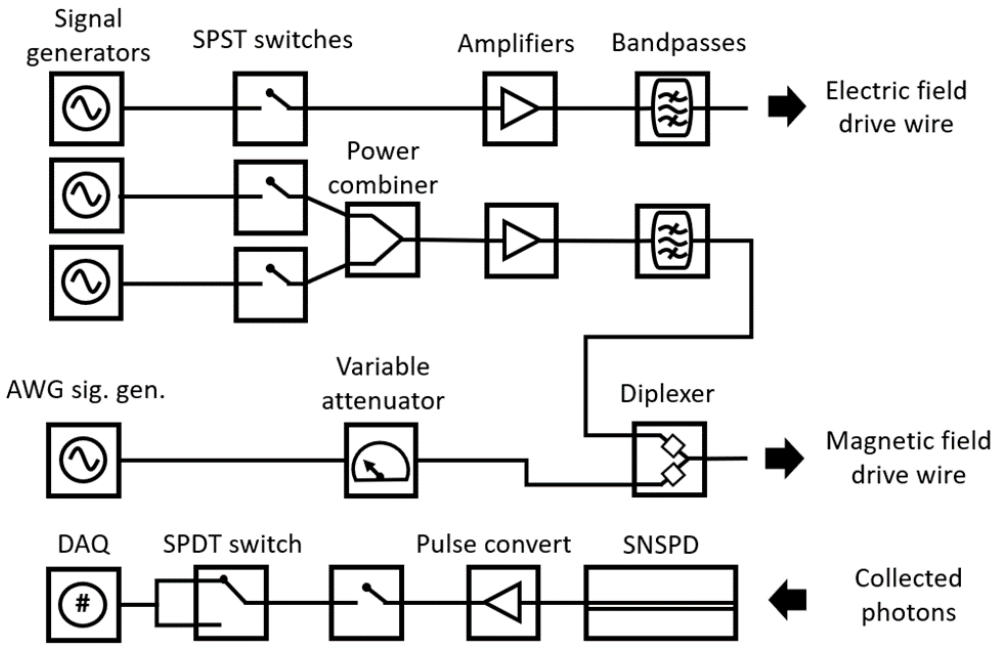

Figure 4.6. **Microwave components.** The major microwave components are shown here, which make up the gating circuitry to generate electrical and magnetic microwave frequency pulses sent to interact with the divacancy spin, as well as the photon counting circuit including the SNSPD. Every signal generator and switch is controlled by a TTL pulse from the AWG (not shown) to enable nanosecond switching on-off the pulses sent to the drive wires on the sample inside the cryostat.

The AWG does not have the power output capabilities we need to drive the requisite spin population rotations. For this, we will need dedicated signal generators (SG396, Stanford Research Systems) that can produce sinusoidal drives in the range of 1-2 GHz at powers up to 16.5 dBm. This power overhead is needed due to compensate for the physical distance between the microwave generation equipment and the cryostat (~3 meters). The frequencies needed are set by the magnitude of the typical magnetic sub-level splittings and ZFS for the *kh* divacancy [25,41]. These signal generators also enable frequency, amplitude, and phase modulation through quadrature modulation (IQ modulation).

There remains to have a way to time-gate the microwave signals generated. This is accomplished by a set of single-pole double-throw switches that can send a microwave pulse to one of two channels from a single input when receiving a TTL pulse from the AWG. Two of the

switches are placed directly after the output of the dedicated signal generators. The extinction ratio of a switch of ~60 dBm provides the necessary reduction in amplitude when combined with an additional ~40 dBm of suppression from the signal generator's amplitude modulation. This allows us to reach "true zero" amplitude for the microwave drive and not drive any measurable spin rotations with the drive turned off. The combination of the switches and AWG timing controls allows for high temporal precision for microwave gates, giving rise/fall times on order of a few nanoseconds in our qubit sequences.

4.4.2 Microwave pulse shaping

A typical experiment will have multiple microwave pulses generated using the instruments of the previous section that must be amplified and then combined to enter the two feed-through lines entering the cryostat. Power amplifiers are utilized to offset the losses in the coax cables when driving fast rotations of the qubits. We typically amplify by ~40 dBm for *kh* divacancy Rabi rotations. Care must be taken at all times because the thin wire bond leads used to bridge the gap from the PCB to the SiC chip can be destroyed if too much power is input. Power dissipation is accomplished by capping the termination lead of our microwave circuit with a 50 Ω termination block. This prevents the input pulses from having reflection components combine into a standing wave that exists throughout the circuit. The presence of a spurious periodic drive would produce an instability in the qubit measurements that would be difficult to troubleshoot during running experiments.

Due to the range of frequencies involved in the experiments, several types of pulse combiners are utilized. A resistive power combiner takes two microwave signals of similar frequencies and can produce a single output signal using the additive property of electromagnetic fields. The cost for using this device and the other types of combiners is a moderate amplitude

modulation, typically on the order of 3-6 dBm per microwave component. This type of combiner is used to send two Rabi driving signals at the same frequencies but at different phases.

For combining frequencies that differ by 1 or 2 orders of magnitude, a diplexer must be used. This is necessary because the high/low-pass filters utilized to prevent cross-talk between the two inputs of a resistive combiner can fail if there is a large frequency difference. A diplexer adds the ~MHz tones used to drive transitions on order of the transverse ZFS.

The two final microwave components employed are a bandpass filter and Schottky diode. The filter rejects all noise sources from instruments or from interactions with the wires, connectors, or passive components. The Schottky diode takes AC drive as an input and outputs a proportional DC signal. We utilize this as a power monitor of the microwave drive for active feedback of our Rabi driving frequencies.

4.4.3 Optical data acquisition

When the AWG signals to the AOM to allow a pulse of laser light to excite the divacancy, we want to be sure to record electronically only the photons created during that a certain readout window. With some temporal delay, the AWG also signals a pair of switches to allow our data acquisition card (DAQ) (PCI-6259, National Instruments) inside a computer to iterate a counter that corresponds to a photon detected by the SNSPD. In all experiments, this is how we obtain the optical count rate raw data. We use that data's correlation with other changing variables such as the laser or microwave frequencies to produce graphical representations of the divacancy's behavior in a software environment described in the next section. Readout contrast can be maximized by calibrating the optimal time window after exciting the divacancy that a photon correlated with the experiment can arrive, before we are simply measuring background counts. We also reject common-mode noise by toggling a switch to send photon count signals to alternating

counter channels and taking the difference of the counts. One counter sees counts from an experiment with microwave excitations and the other sees counts without microwaves sent to the sample.

4.5 Data acquisition software: SPYRE

We have described up to this point several collections of instruments that must work in tandem to perform experiments on our qubit. As there are a handful of similar setups in our lab that operate using similar optical and microwave control schemes, a software program that we call SPYRE has been developed and built up over the course of several years. SPYRE (Scientific Python Research Environment) integrates a number of mature packages native to the Python language such as NumPy and SciPy, among others. The core feature is unification of communication with several experimental instruments so that raw data can be aquired, graphed, manipulated, and saved for analysis from any combination of them in a single program. The central hierarchical design of SPYRE revolves around defining subsets of instruments responsible for taking the data for a particular experiment. These subsets are contained within a single “spyrelet”, or tab of the program. Breaking up the experiment into organized spyrelets allows taking organized data from the many subsystems of the setup.

4.6 Experimental methods

Having covered the hardware and computer interfaces used in the experiments of the divacancy spin qubit system, the remaining sections in this chapter cover the main methods to record raw data from experiments measuring the divacancy system. The presented methods detail the necessary processes when characterizing a new sample of SiC prepared with single defects and

measuring the major optical and spin properties of a single divacancy. This list of procedures reflects the experiments that lay the groundwork for the results presented in Chapter 5

4.6.1 Raster scans

We begin with a few millimeter square chip (typical: 5x5 mm) of 4H-SiC that we assume has undergone electron irradiation and annealing steps that have been calibrated to produce densities of divacancies that can be optically resolved at NIR wavelengths. The epitaxially grown layer ten to twenty microns deep is where we want to find single divacancies to characterize. There is a trade-off though between divacancies that are too shallow or too deep. Optical background from the bulk, n-type doped layer can wash out the signal from single divacancies and surface impurities or contaminant particles can hinder optical collection efficiency as well.

The procedure to first find divacancies given these constraints goes as follows. A clean region near the lithographically patterned drive wires is chosen by sweeping the field of view of the visible wavelength camera using the x- and y-axis stages of our piezo stack. The camera also allows us to ascertain if the 905 nm off-resonant laser is focused on the surface or not. We dampen the power of the laser significantly to focus its gaussian beam profile on the sample surface. Then we turn the off-resonant laser to powers such that the divacancy optical signal will be saturated (typical: 5-20 mW) and complete a raster scan by scanning both the x and y-axis tilt axes of the FSM while recording the optical counts. We call the resulting 2D maps composed of bright spots/regions from various photo-active species “FSM scans.”

These FSM scans with off-resonant light are utilized as an optically non-selective survey of the SiC near-surface environment. Since the constellations of “bright spots” can be created by any of the divacancy orientations or other photoluminescent complexes in the sample, there is a certain flow chart of further checks that must be done on a bright spot that is suspected to be a

divacancy of interest. Initial checks involve observing the time dependence of the photon count rate to check for stable emission. Certain samples can have charge noise that can cause the divacancies to "blink" out of their neutral, photo-active charge state.

Spectral filtering is a main tool to determine the identity of a bright spot. It is known that the ZPL + PSB of PL2 (optical signature from kk divacancies) starts at around 1150 nm. Below 1150 nm, is around one third of the PSB of PL4 (*kh* divacancy spectrum) [41]. Thus, adding an 1150 nm shortpass filter should greatly dim spots from PL2 and reveal likely candidates for PL4 bright spots. Similar trial and error using other filters can increase the probability we know the species of divacancy that matches a bright spot. Of course, acquiring the full spectral response, using a grating spectrometer from a certain spot on the sample can be used to increase this confidence.

4.6.2 Photoluminescence excitation scans

After off-resonant FSM scans have allowed us to zero-in on a particular divacancy that we might want to study, the next step is to characterize its photon emission rate into the PSB under resonant laser excitation. We will focus here on considerations of a PL4 divacancy. The difficulty is that a PL4 optical resonance line can exist in a broad region relative to the scan time of our resonant laser. Considering the divacancies measured in this thesis, a typical PL4 linewidth at 4 K is on the order of a couple hundred MHz, while the center wavelength can be found in a ~150 GHz region due to inhomogeneous shifts from local strain or electric fields. A typical scan rate of ~5 GHz/min means we want to use high resonant laser powers (>100 μW) and sometimes higher temperatures (10-15 K) that broaden the optical lines to a few GHz. These procedures can reduce the total time spent finding the optical line.

After finding an optical resonance at a reasonable frequency for the divacancy configuration sought, we aquire photoluminescence excitation spectra (PLE). We scan the resonant laser at low powers (below 1 μW) to avoid power broadening to measure the linewidth of the single divacancy's optical spectrum. In the limit of low inhomogeneous broadening, we can fit the optical fine structure curves very well to a Lorentzian profile to determine the frequencies of the three spin-conserving optical transitions. We refer to the amplitude of the Lorentzian curves as the "PLE signal" that serves as a shorthand for the count rate when addressing one of the optical transitions corresponding to one of the divacancy's spin states. Sometimes, the linewidth of the individual lines can be broad enough that two lines can overlap. This is particularly troublesome for the lines corresponding to the $|0\rangle$ and $|-\rangle$ states of PL4, which are only separated by ~120 MHz. This will ultimately limit the spin contrast we can achieve in spin qubit readout. The absolute magnitude of the PLE signal does not carry very much useful information. That might sound surprising, but it is mostly determined by an array of experimental factors based on the average chance a laser photon reaches the divacancy to excite it and then that a photon created by the divacancy is not lost and produces a pulse from the SNSPD. Great care in designing and maintaining our setup goes into maximizing that collection efficiency for each experiment.

In order to define how we utilize optical signals to prepare and readout the spin state of our *kh* divacancy qubit, we can think of the PLE signal as a microwave experiment with zero input drive power. On average, the electronic state of the *kh* divacancy will be in one of the groundstate sublevels, $|0\rangle$, $|-\rangle$, or $|+\rangle$ depending on its particular thermal state. When a resonant optical photon arrives, the photon has some average chance to induce an excitation depending on which transition it is closest in frequency to. Then, after the photon exchanges energy with the spin state, the electronic state will relax either radiatively into the same spin state or non-radiatively through the

ISC singlet pathway. As discussed in Section 3.3.1, this non-radiative relaxation is most commonly into $|0\rangle$, but possibly into one of the others. Of course, there is some thermal spin-flip chance as well to consider. The integration of all these rates gives the average PLE signal measured for zero microwave input while addressing the defect with a particular optical frequency at a certain power. The experiments presented in this thesis at their core measure the change in the PLE signal when we apply microwave drives, both continuous and pulsed, to measure the outcome of changing the state of the qubit made up of two of the divacancy's spin states. The experiments involve population rotation and decoherence measurements, which we will now describe in detail in the following subsections.

Determining the optical resonance frequency of a divacancy using PLE scans enables us to measure the energetic properties of its ground-state. This gives perhaps the most tell-tale identification for the orientation of divacancy. For the *kh* divacancy, there should be an increase in the PLE signal when driving our microwave lines at frequencies near 1.35-1.40 GHz [41] with sufficiently high power. This frequency range corresponds with the energy difference between the $|0\rangle$ to $|+\rangle$ state at zero magnetic field. Here we can begin to define operational definitions for our qubit. The "bright", or "on", state here is defined usually as the $|+\rangle$ state for a *kh* divacancy, while $|0\rangle$ is the "dark", or "off", state. Our qubit is considered in the bright state when a PLE readout measurement shows an increase in counts when tuned to excite the optical line of the $|+\rangle$ state.

4.6.3 Continuous optically detected magnet resonance (ODMR)

We will describe here how the initial rough values for the groundstate transition frequencies are determined in the case of an uncharacterized single *kh* divacancy using continuous optical detected magnetic resonance (ODMR). At this stage we assume zero magnetic field. The static background magnetic field value will change the ODMR value, as prescribed by the Zeeman affect (Section

3.2.5), but we will return to that at the end of this chapter when we have discussed coherence measurement of the spin in more detail.

To perform continuous ODMR, we send a sinusoidal tone from our function generators to our sample and sweep the frequency over the range of 1-2 GHz continuously. No other microwave gating is necessary. At the same time, we send a continuous pulse to our resonant AOM to allow continual resonant laser driving on the $|+\rangle$ optical transition, which we choose as the "bright" state in this example. We monitor the count rate for the PLE signal, and when the microwave drive is on-resonant with the $|0\rangle$ to $|+\rangle$ transition, there is more chance the electron will be promoted to and be in $|+\rangle$ where the optical drive can promote the electron to produce a photon. Seeing an increase in counts at a certain microwave frequency that matches literature values for ODMR resonance values gives us confidence that the microwave drive is addressing the ground-state transitions of the single divacancy we currently are studying.

4.6.4 Pulsed optically detected magnet resonance (ODMR)

While continuous ODMR is a powerful initial characterization tool due to its broad searching bandwidth owning to the high probability of displaying some spin contrast in the PLE signal imparted by the continuous microwave drive, it cannot perform fine control over spin rotations. Pulsed ODMR begins to define a method of controlling the state as a spin qubit. Additionally, for *kh* divacancies, continuous ODMR can be complicated by electrically induced resonances in the optical absorption spectrum regardless of the spin state, where Landau-Zener-Stuckleberg interference fringes will complicate the PLE spectrum [25].

Here we first utilize the high-fidelity spin initialization technique first discussed in Section 3.3.1 to ensure our spin starts in the $|0\rangle$ state. The ultimate goal is to find the frequency, ω, and the power, P, to define a microwave π pulse that will fully invert the population of the spin state from

the dark state to the bright state. (Choice of what spin state to call the bright/dark is arbitrary.) Looking at Eq. (2.35), when we are exactly on resonance with the spin transition, $\Delta = 0$, the population rotation is simply the angle:

$$\theta = \Omega \cdot t \,. \tag{5.1}$$

Where t is the time we of the pulse, or the time the microwave switches toggled to allow photons to be sent to the cryostat, and Ω, the Rabi frequency, in the experiment is proportional to the voltage amplitude of the applied drive. Unfortunately, while we can define t very precisely, the actual amplitude at the divacancy in the SiC chip is hard to analytically define. Thus, our initial guess for the power will either under or over rotate the spin. This can lead to a myriad of different changes in the PLE signal for an initial guess of Ω that we set our signal generators to. This is where common mode noise subtraction mentioned in Section 4.4.3 comes in handy. By removing other noise features in the PLE signal, the pulsed ODMR spectrum can reveal the features due to the under or over rotated line shapes, giving an indication for the bounds of the microwave transition frequency measured using pulsed ODMR.

5. Rabi oscillations

Once an initial ODMR spectrum can be identified showing population inversion, varying either Ω or t systematically can produce clean, sinusoidal Rabi driving of the measured PLE signal that indicates the population in the bright state. This can be used to produce the first controlled spin population rotations. As mentioned in the previous section, the Rabi formula gives two tractable degrees of freedom for the population rotation angle, the amplitude of the microwave drive, Ω, or time that drive is pulsed for, t. The condition for that ideal behavior is zero detuning from the magnetic resonance condition.

We consider first the case where nearby hyperfine interactions from nearby nuclear spins leads to non-sinusoidal behavior due to the prefactor being a function of the detuning, Δ. The higher the amplitude can be made, the less this effect is seen. This might indicate that sweeping the time, which does not show up in the prefactor, is better practically, but our AWG has 2^{16} step resolution for Ω while the time steps are limited to ~1000 due to the sampling rate of the AWG. The $\Omega \gg \Delta$ can indeed be practically achieved for the *kh* divacancy so we choose to do amplitude sweeping Rabi oscillation experiments in the presented results.

Here we can take a step back to appreciate what this Rabi drive is doing to the electron spin state of the divacancy by looking at the full experimental sequence. We start by exploiting the preference for the triplet state to decay into the $|0\rangle$ state after a certain time under off-resonant illumination to achieve spin initlization. Thus, our initial quantum state is as well-defined as possible. If we then apply a strong enough drive on resonance with $|0\rangle$, and $|+\rangle$, we can consider the system under the RWA Section (2.4). Here we can return to the Bloch sphere analogy to describe precisely what we mean by a population rotation. Here, spin up and down states become $|+\rangle$ and $|0\rangle$. The third state, $|-\rangle$ has a large enough energy separation at zero field to not cause issues for the TLS approximation. Then we utilize phase modulation for our microwave signal generator to choose a rotation basis around the Bloch sphere for the superposition state. We by default choose the x-plane for the rotation. The Rabi formula then describes the chance a measurement of the superposition state will collapse to yield a situation where the triplet state ends in $|+\rangle$ and a photon is produced by the resonant readout laser pulse. If the Rabi experiment indeed produces curves that can be fit to a sine function, then while vary the amplitude of the microwave pulse, Ω, we can say when PLE signal is lowest defines the π pulse. Since t is constant in amplitude Rabi, this defines the π pulse completely. Usually, ODMR and Rabi experiments work in tandem

at this stage. Doing one and then the other iteratively defines better guesses for the best value of the frequency for the magnetic resonance transition, ω, and the best parameters of the π pulse.

4.6.5 Ramsey experiments

At this stage, we can finally describe the system as a qubit and thus leverage the results of Section 2.7 to discuss the decoherence properties of our qubit. In the Bloch sphere picture, we now have the capabilities to generate arbitrary superpositions of any two levels in the divacancy ground-state triplet. This and the next section focus on two important experimental methods for this thesis: measuring the inhomogeneous dephasing time, or Ramsey coherence time, $T_2{}^*$ and measuring the Hahn-echo coherence time, T_2.

We begin by defining a Ramsey free precession experiment. From the ODMR + Rabi experiments beforehand, we can drive a π pulse up to the precision of our experimental process, and thus if we halve the amplitude, we can also drive a $\frac{\pi}{2}$ pulse to rotate our superposition into the equator. Now, we allow the state to evolve a certain time in the equator, $t_{equator}$. Consider that our qubit is in a perfect vacuum under the influence of no external fields. After $t_{equator}$, a second $\frac{\pi}{2}$ pulse, or $-\frac{\pi}{2}$ pulse, will return the superposition exactly back to either of the poles of the Bloch sphere. But the SiC crystal is far from this idealized vacuum, and there will be noisy (i.e. difficult to precisely define) fields that will lead to random accumulation of extra phase in the quantum state. This process is usually called free evolution because the quantum state, rotated off the basis state, is free to precess under the influence of noise fluctuations. It is better to rename $t_{equator}$ into t_f for free evolution.

The phase accumulated will be random for each instance of the measured ensemble of experiments. By doing a differential measurement where alternating readouts of the presence of a

photon using a $\pm\frac{\pi}{2}$ pulse for increasing t_f, we obtain maximal distinguishability in the measurement of the distribution of spin populations that will make up the exponential decay defined in Section 2.7.2. We can fit this curve to find the time-scale for our qubit we call the inhomogeneous dephasing time, $T_2{}^*$. After our sweep exceeds a certain t_f, readout will show no contrast. Thus, $T_2{}^*$ can be considered the "useful computation time" of our qubit. For if we consider the ultimate goal of qubits to represent information in superposition states, then beyond the timescale of $T_2{}^*$, measuring those superpositions would yield no distinguishability between the two measured basis states, and we would simply be measuring the classical ensemble for our divacancy. In order to be able to measure the resulting superposition after rotations of our superposition, readouts of a manipulated quantum state must be done within the $T_2{}^*$ timescale.

An important feature of the exponential decay in a Ramsey experiment is a sinusoidal feature that denotes the detuning from the actual energy splitting between the superposition basis states. When a drive of $\omega + \omega_d$ is used for the Rabi drive, where again ω defines the splitting, one can plot the PLE signal as a function of the detuning, ω_d. Choosing a single, non-zero value for the free precession time, we sweep the detuning and can observe spin projection information as a sinusoidally changing PLE signal where the maxima indicate no precession in the rotating frame, indicating zero detuning of the Rabi drive.

4.6.6 Hahn-echo experiments

We continue our discussion of measuring the coherence of our divacancy spin qubit by describing a Hahn-echo sequence that can cancel the inhomogeneous phase noise accumulated during the free precession time under certain conditions. As in Section 4.6.6, we assume that the local noise distribution can be considered quasistatic on the timescales of the coherence measurement, or more precisely, for the duration of t_f. This quasistatic noise is represented by a constant rotation the

constant rotation, v, of the superposition in the Bloch sphere equator. If we perform a calibrated $\frac{\pi}{2}$ pulse to create a superposition in the equator that is affected by this rotation, after a certain t_f, we accumulate phase, δ, equal to $\delta = t_f * v$. Now if we perform a π pulse to rotate the superposition, if the noise is purely quasistatic, after a second t_f, we would gain $-\delta$ phase to cancel the phase error. Upon doing the differential measurement to refocus the qubit on the pole states and readout the resulting PLE signals with different t_f's, any non-quasistatic noise then becomes the dominant source of dephasing, where we measure T_2 as the resulting exponential decay constant.

Hahn-echo sequences represent the first attempt to modulate the lifetime of a quantum superposition under the effects of deleterious phase noise. The concept of an echoing pulse can be extended to an arbitrary number of pulses, in segments of $t/(N+1)$ with N π pulses. This technique is called "dynamical decoupling," or a CPMG sequence [59,64]. Adding these additional segmentations of the free evolution allows the cancelation of noise sources with faster oscillations, on order of $t/(N+1)$. The addition of more and more pulses to protect the superposition and extend its Hahn-echo time does come with the downsides of lower experiment repetition rate, impacting averaging times.

4.6.7 Magnetic field tuning

A consequence of the large transverse ZFS in the *kh* divacancy groundstate is that spin qubit prepared in its magnetic sublevels will experience better coherence at zero magnetic field [25]. This is a consequence of an anti-crossing lifting the degeneracy of the states corresponding to $m_s = \pm 1$ resulting in lower energy level sensitivity per unit magnetic field change, as discussed in Section 3.2.5. This feature of the basal divacancies in 4H-SiC motivates the need to obtain zero static magnetic field at a single divacancy and will be a central feature explored in the results in

Chapter 5 where this anti-crossing, or clock transition, at zero magnetic field will form the basis of investigating a modification to the Hamiltonian that result in even longer coherence times. For now, we are just concerned in this Section with obtaining:

$$\vec{B} = \left(B_x, B_y, B_z\right) = 0 \text{ , where } \vec{B} \neq \vec{B}(\text{t}) \tag{5.2}$$

in the cryogenic sample chamber detailed in Section 4.2. The first step is to simply measure $\vec{B}$. An in-situ magnetometer close enough to obtain the requisite precision is not feasible. Commercial detectors would have to be directly on top of the SiC chip, but the 4 mm working distance of our objective prevents that, and the overall compactness of the chamber is necessary to keep the total cooling power high. The solution involves a very good detector of magnetic fields: the spin qubit itself. We know that a non-zero, static $\vec{B}$ from stray fields will increase the qubit's sensitivity to quasistatic magnetic field noise in the crystal. This in turn will reduce the observed coherence during a Hahn-echo measurement of T_2. We use T_2 over $T_2{}^*$ because there were asymmetric zero-field conditions measured when changing the order of the magnetic field's cartesian components and because T_2 obtains first-order insensitivity to energy detunings due to magnetic fields in the *kh* divacancy.

We utilize an iterative 3-axis sweep of adding additional magnetic field from stable sources to cancel the unknown starting $\vec{B}$ until we reach a maximum T_2. In this section, we define the vector normal to the SiC surface as $\hat{z}$ and normal to the optical table as $\hat{y}$. First, inch-scale neodymium magnets with fields on order of a 100 gauss at their poles are swept over large distances near the outside walls of the cryostat. It was found that two such magnets were needed to add moderate -$\hat{z}$ and $\hat{y}$ components. Fine magnetic field calibration was accomplished with a set of a 3-axis solenoid electromagnet with iron cores. After a number of iterations of all three

axes, a zero-field condition can be achieved up to the error in the current in the solenoids, about 0.001 mA.

Chapter 5

UNIVERSAL COHERENCE PROTECTION IN A SOLID-STATE SPIN QUBIT

5.1 Introduction

This result centers on the how the host crystal lattice and Hamiltonian engineering can increase the coherence times of electron spins to timescales useful for state-of-the-art quantum information applications. This is done by protecting a solid-state qubit from fluctuations that would typically reduce its coherence. The divacancy defect in 4H-SiC has the benefit of shielding from thermal decoherence due to its position deep within its crystal host's wide bandgap from which it gains long spin coherence [39], positioning it as a strong candidate for engineering quantum control using phonons [26,65,66], optical cavities [47], or classical electronic diode structures [21,27].

All crystal hosts of spin qubit candidates are home to fields that threaten to decohere the quantum state of the qubit during manipulation of a created superposition. The typical coherence timescales found in well-studied electron spin complexes, including the divacancy and the nitrogen-vacancy, are microseconds for the inhomogeneous dephasing time, T_2^* [39,67], and milliseconds for the Hahn-echo coherence time, T_2 [27,39,67,68]. Taking the divacancy as an example, the bath of non-zero nuclear spins in SiC (silicon-29 and carbon-13) is responsible for the bulk of the magnetic noise that limits the spin dephasing times to the aforementioned

timescales. Even with the relatively low natural abundance of those nuclear species in SiC, when they are proximal to the divacancy, the coupling produces inhomogeneity in the spin and orbital energy levels during operation of the qubit.

Nuclear spins are not the only major source of decoherence. In cases where there are no near-neighbor nuclear species, electromagnetic fluctuations from paramagnetic species can limit coherence times [25,27,69]. As the growth of silicon carbide improves, the densities of these impurities will hopefully raise the floor on natural coherence times.

It remains to fully remove the decoherance from nuclear spins present in a sample, but there are tractable methods being explored. Simply having a lower nuclear spins at the onset by using isotopic purification techniques [70] during growth reduces the spin bath noise significantly in divacancy qubits in 4H-SiC [21,28]. The availability of high quality isotropically purified 4H-SiC limits the scope of such endeavors and active field control is the preferred at-scale method.

Dynamical decoupling is the most common activate method of reducing the accumulation of inhomogeneous phase error by canceling out certain dominant components by adding periodic control pulses [64,71]. The greatest drawback dynamical decoupling techniques is that any finite pulse devoted to reducing incurred error reduces the total available time one can use to do “useful” spin rotations. Those rotations used for information manipulation or information transfer to another quantum system are the ultimate goal for developing these spin qubits. Seeking solid-state spin qubit candidates or improving the environment around previously studied ones can open up new possibilities for improved coherence values.

This chapter presents a method that reduces a *kh* divacancy’s spin sensitivity to decohering fields in 4H-SiC by engineering the energy levels of its spin Hamiltonian directly so that our qubit is made up of new, dressed states built out of the existing spin bases. To show the strength of this

technique, this will be done with a 4H-SiC crystal that has been acquired with minimal processing done to reduce environmental inhomogeneous noise sources. All noise sources will be shown to have reduced effects on the spin coherence, including magnetic, electric, and thermal. This is primarily shown by a measurement of a four orders of magnitude increase in the inhomogeneous dephasing time, T_2^*, of a spin qubit prepared within the magnetic sublevels of the *kh* divacancy when comparing to typical conditions seen by *kh* divacancies in the bulk. This value is one of the largest values seen for an optically addressable electron spin qubit. the highest Critically, this method offers these enhancements without utilizing long pulse trains normally used to correct inhomogeneous noise and could be a replacement for dynamical decoupling in certain systems. The coherence times realized as also reaching timescales normally only seen when using nuclear spin state basis for qubits, which have inherent shielding from noise sources. This protocol thus offers high levels of shielding but retains the *kh* divacancy's electron spin's highly tunable optical, microwave, and electrical interfaces [25].

5.2 Results

This result builds upon a consequence of the *kh* divacancy's single mirror plane symmetry where its energy level sensitivity to stray magnetic fields reduces dramatically near a clock transition at zero magnetic field due to its high transverse and longitudinal zero field splittings (ZFS)[25]. We show operation of a dressed basis [65,72–77] in the magnetic ground-state after applying a continuous microwave drive resonant with the transverse ZFS that produces Autler-Townes splitting of two of the hybridized triplet spin states of the *kh* divacancy. We then perform spin lifetime measurements within this dressed basis and characterize it as a decoherence protected subspace that suppresses inhomogeneous shifts from local field fluctuations. The extent of this protection is probed by precisely measuring the magnetic effects on the energy transitions with 3-

axis field scans. The tradeoff is first-order sensitivity to quasistatic noise content of the added continuous microwave drive, which we can track and mitigate to some degree using active feedback protocols.

We list here the advantages of utilizing a continuous drive to yield an extended coherence for the spin compared to using active field controls like dynamical decoupling. Arbitrary manipulations of a protected electron spin during a dynamical decoupling sequence can be difficult to achieve, save for some implementations of complex pulse trains [78,79]. The longer and more complex the pulse train for a dynamical decoupling sequence, the higher chance uncorrected dephasing can accumulate due to experimental pulse errors. Universal dynamical decoupling [80] seeks to mitigate the effects of such errors, and bang-bang dynamical decoupling seeks to shorten the necessary length of the pulse trains [81]. These advancements are pushing the cutting edge of active coherence enhancement, but they can add significant experimental overhead in their execution, and this opens up the need for simpler methods that can be applied. The method presented here offers the ability to greatly enhance coherence of a spin using pulses, which removes the imperfections inherent to generating clean rising and falling edges in microwave pulse trains. Furthermore, we gain these advantageous while retaining the full spectrum of magnetic and electrical response to driven microwave fields to perform rapid quantum operations of the long-lifetime spin qubit in the decoherence protected subspace.

The main details of the material system, experimental control, and the *kh* divacancy energy levels are first discussed in order to explain how the dressed states are created and manipulated. Then the method for measuring the extended coherences is presented. What follows is details of the added protection from the noise sources present, including vector magnetic field scans showing the magnetic sublevels of the protected basis's response to applied noise. Finally, a number of

conclusions about the usability and benefits of this dressing drive approach are discussed. These include the method's platform agnostic nature, where the most important prerequisite being a large magnitude in the transverse ZFS for the spin Hamiltonian, and this system's advantages as a component in hybrid quantum systems due to its electron spin T_2^* allowing fast, on-demand, strong coupling to other qubit platforms.

5.2.1 Experimental details

We study the single *kh* divacancies in the optical and microwave generation setup described in Chapter 4 We use a 5-by-5 mm chip of high-purity semi-insulating 4H-SiC with a 20 μm thick layer of insulating-type 4H-SiC epitaxially grown atop it. It was purchased from a commercial source, from the supplier Norsel AB. The epitaxial layer c-axis has a 4° tilt off-axis that we account for in our magnetic field alignment. Preparation of a density of single divacancies in the chip involved electron irradiation with 2-MeV electrons at a dose of 3E12 electrons per square centimeter followed by 850 °C annealing in Ar atmosphere for 30 min. Metal leads (Figure 5.1A) were patterned on the chip using electron beam lithography to allow generation of electromagnetic fields local to the optical laser spot. The function of the metal leads included a magnetic drive wire and two wires making up a coplanar capacitor structure. Width of all the leads was 10 μm and the materials deposited were sputtered layers of Ti + Au. These wires provide control over the ground-state spin-1 system of a single *kh* divacancy that is found in the 4H-SiC epitaxial layer using off-resonant raster scans (Section 4.6.1). Scanning with a resonant laser reveals the optical interface of the groundstate of the isolated divacancy at a frequency of 277.95597 THz and we measure its optimized photoluminescence excitation signal (PLE) (Section 4.6.2) to be on average 4.28 kcps.

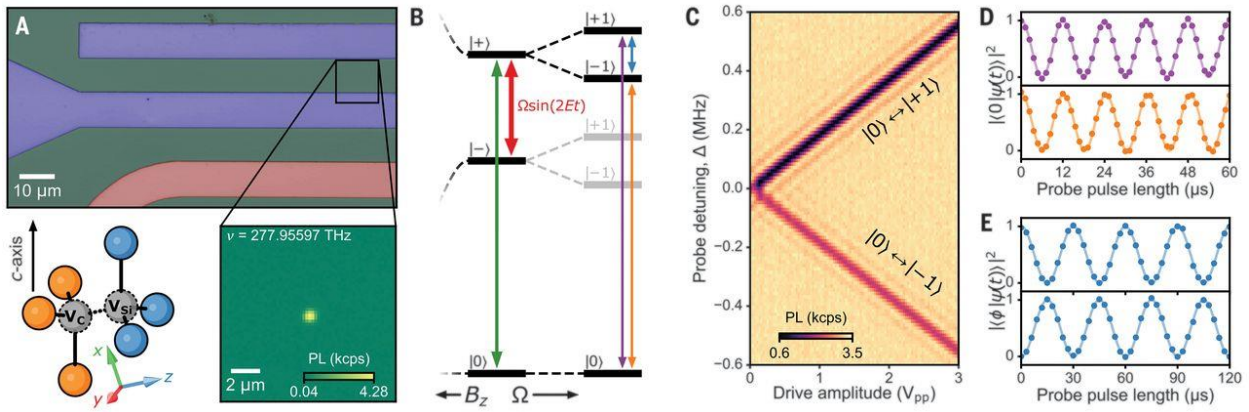

Figure 5.1. **Driven *kh* divacancy spin system in 4H-SiC. (A):** Optical microscope image (false color) of the 4H-SiC sample showing electrical capacitor (blue) and microwave drive wire (red) for ac electrical and ac magnetic driving of the spin in the region between the capacitor wires. Inset shows the single *kh* divacancy's PLE signal from driving $|0\rangle$ state spin character optical resonance. Lower left: *kh* divacancy lattice showing nearest-neighbor carbon (blue) and silicon (orange) atoms. Cartesian axes of the spin-1 system are labeled. **(B):** Energy levels of the ground-state spin of the *kh* divacancy. Dashed lines to the left show the dispersion of the clock transition as B_z increases from the zero-field conditions. Green (red) arrow indicates spin driving of the magnetically allowed transition $|0\rangle \leftrightarrow |+\rangle$ ($|-\rangle \leftrightarrow |+\rangle$) in the undressed basis. Dashed lines to the right show Autler-Townes splitting resulting from continuous microwave driving of $|-\rangle \leftrightarrow |+\rangle$ at frequency $2E$ at amplitude Ω. Resulting levels form a hybridized spin-photon dressed basis. Purple (orange) arrow indicates spin driving of the magnetically allowed transition $|0\rangle \leftrightarrow |+1\rangle$ ($|0\rangle \leftrightarrow |-1\rangle$) in the upper branch of the dressed basis. Blue arrow indicates spin driving of the magnetically forbidden transition $|-1\rangle \leftrightarrow |+1\rangle$ accomplished with ac electric fields. Greyed out copy of $|\pm 1\rangle$ levels in lower branch are inaccessible due to inability to strongly drive $|0\rangle \leftrightarrow |-\rangle$ (See Appendix B.). **(C):** Pulsed optically detected magnetic resonance (ODMR) showing Autler-Townes splitting of $|+\rangle$ while continuously driving transition $|-\rangle \leftrightarrow |+\rangle$. The probe's detuning, Δ, is relative to the $|0\rangle \leftrightarrow |+\rangle$ resonance frequency. **(D):** Purple (orange) curve shows Rabi oscillations of spin population between $|0\rangle \leftrightarrow |+1\rangle$ ($|0\rangle \leftrightarrow |-1\rangle$) upon pulse of ac magnetic microwave drive. **(E):** Top (bottom) blue curve shows Rabi oscillations of spin population between $|-1\rangle \leftrightarrow |+1\rangle$ readout from $|+1\rangle$ ($|-1\rangle$) using contrast recovery sequence (Appendix B.).

Using a combination of optically detected magnetic resonance (ODMR) and Rabi experiments (Section 4.6.4), we can access the magnetic sublevels of the divacancy at non-zero magnetic field ($\hat{B} \neq 0$). We can drive spin population between the energy levels at mixed character between the bare triplet state ($|0\rangle, |m_s = -1\rangle, |+1\rangle$) and the hybridized, linear combination of those states ($|0\rangle, |-\rangle, |+\rangle$) that dominate description of the energy diagram due to the high magnitude of the transverse ZFS at $\hat{B} = 0$ (Section 3.3). Using the magnetic field zeroing process (Section 4.6.7) we find and operate the spin in the regime of $\hat{B} = 0$ where we find optimal parameters for the π

pulses between all three basis states, giving us full spin control to create superpositions between all three states in their respective rotating frames.

We measure the precise value of the transverse ZFS to define the frequency of the dressing drive which will generate magnetic sublevels of the decoherence protected subspace. Ramsey interferometry between the states $|-\rangle$ and $|+\rangle$ is used to accomplish this. (Section 4.6.5) The superposition between those states is allowed to undergo free-precession for a time of 100 μs. This time was chosen to maximize the signal to noise along with the frequency resolution. We extract our value for the transverse ZFS, E, of our single divacancy as $E/2\pi = 18.353164(4)$. This defines the dressing drive's angular frequency as $\omega = 2E$, which will enable creation of dressed states made from $|-\rangle$ and $|+\rangle$ to make a new qubit basis (Figure 5.1B).

5.2.2 Generation of dressed states

With the application of this dressing drive to the single divacancy using the microwave drive wire, the Hamiltonian under which we entered the RWA for the electron spin system is no longer valid (Section 2.4). We must construct a new Hamiltonian to both define the new energies as well as show that the new states act like a new divacancy triplet manifold, where transitions for the electron spin outside the 3-level complex are disallowed by selection rules. We will use the tenets of Floquet theory to exploit the fact our new drive addition to the *kh* divacancy Hamiltonian matrix, $\hat{H}$, is periodic, in that it satisfies:

$$\hat{H}(t) = \hat{H}(t + t_o). \tag{5.1}$$

We invoke Floquet's theorem where the new quantum states will have the form similar to our general solution for a TLS. The derivation is located in Appendix B. When applying a strong magnetic field drive with Rabi frequency, Ω, we see there is a Autler-Townes splitting of the

spin states $|\pm\rangle$ by exactly half the drive amplitude into new dressed states. The $m_s = 0$ state remains unperturbed. We make a notation choice for compactness where the dressed states of $|+\rangle$ will be denoted by their Floquet mode number (see Appendix B.) and label the new spin triplet states as $|\pm 1\rangle$ and $|0\rangle$. This is not related to the non-zero magnetic quantum number and any reference to the states $|m_s = \pm 1\rangle$ in this chapter will be explicit. The dressed states eigenvectors turn out to simply be linear combinations of the *kh* divacancy states at zero magnetic field:

$$|\pm 1\rangle = \frac{1}{\sqrt{2}}(|-\rangle \pm |+\rangle). \tag{5.2}$$

5.2.3 Dressed basis driving

The new dressed basis ($|0\rangle$, $|\pm 1\rangle$) of the divacancy groundstate can be accessed when the dressing drive Ω is turned on. In this section, we will describe how we perform coherent driving between the dressed states while staying in a low-noise regime. We wish to show full control of the three-level system, which includes retaining the ability to initialize and readout the spin-state, as well as drive spin population between the levels to create superposition states. Our spin initialization procedure (Section 3.3.1) is not fundamentally changed by the introduction of the dressing drive because $|0\rangle$ retains its original properties. Off resonant laser driving of the system still leads to preferential decay into $|0\rangle$ after several microseconds. We will describe two types of spin rotations used in this result. There is ac magnetic driving using the on-chip drive wire to accomplish $\Delta m_s = \pm 1$ transitions from $|0\rangle$ to $|\pm 1\rangle$. There is also ac electrical driving using the on-chip capacitive pads for $\Delta m_s = \pm 2$ transition between the $|\pm 1\rangle$ states. The Floquet Hamiltonian leads to a non-

trivial "best" choice for the Rabi frequency used for this system, $\frac{\Omega}{2} = 350\ khz$. This is used in order to mitigate the higher order dispersion components present.

We now describe a protocol for reading out the population of the dressed states, which necessarily contains character from all three undressed states. The basic operation can be encapsulated by adding an extra rotation about the Bloch sphere to enter a basis that we can perform a high contrast readout operation, as described in Section 4.6.2. Thus, we can perform what we call the contrast recovery sequence to readout any arbitrary superposition in our three-level dressed basis. The contrast recovery (see Appendix B.) involves non-adiabatically turning off the dressing drive and rotating into the basis of $\{|0\rangle, |+\rangle\}$, where reading out the PLE signal from the $|0\rangle$ state accomplishes the spin readout.

5.2.4 Coherence measurements

Having established a version of our experimental methods for the dressed states that retains the high signal to noise readout of optical signals and coherent spin population control, we now perform Ramsey and Hahn-echo measurements as prescribed in Section 4.6.5 and 4.6.6 to quantify the energy inhomogeneity within the decoherence protected subspace of the dressed states.

We find a value of $T_2^* = 22.40(10)$ (Figure 5.2A) when we prepare a superposition state, $|\psi\rangle$, in the upper branch states of form:

$$|\psi\rangle = \frac{1}{\sqrt{2}}(|-1\rangle + |+1\rangle). \tag{5.3}$$

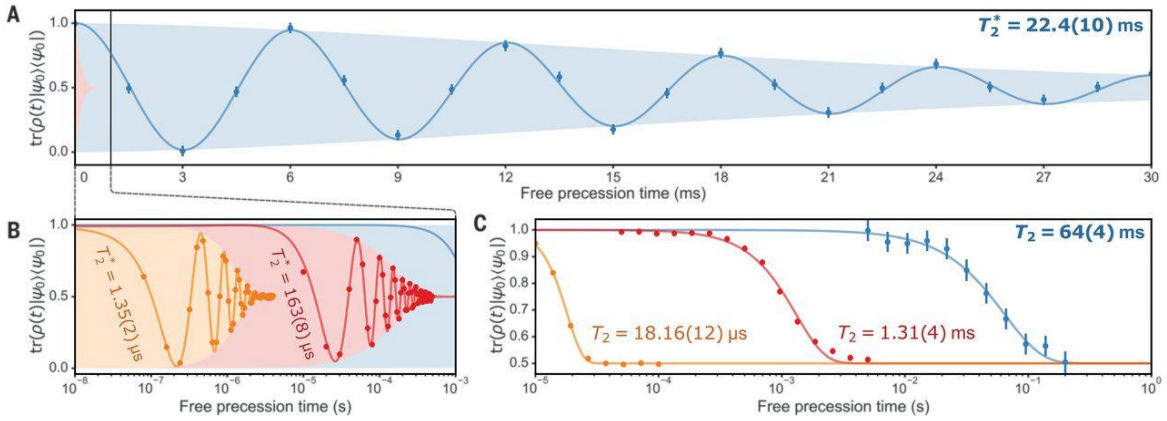

Figure 5.2. **Measured coherence values in decoherence-protected subspace. (A):** Blue curve shows Ramsey free precession of a superposition, $|\psi\rangle = \frac{1}{\sqrt{2}}(|-1\rangle + |+1\rangle)$, created in the dressed basis of the decoherence protected subspace at $\vec{B}$ = 0 mT. A frequency detuning of 166.6 Hz is added for visibility. **(B):** Red (orange) curve shows Ramsey free precession of a superposition, $|\psi\rangle = \frac{1}{\sqrt{2}}(|0\rangle + |+\rangle)$ ($|\psi\rangle = \frac{1}{\sqrt{2}}(|0\rangle + |m_s = +1\rangle)$, created in the undressed basis at $\vec{B}$ = 0 mT ($\vec{B}$ = 1.2 mT). Significantly shorter spin dephasing times are seen outside of the decoherence protected subspace. **(C):** Hahn-echo free precession of the same superpositions under the same conditions for the blue, red, and orange Ramsey free precession experiments in (A) and (B). Error bars are one standard deviation.

This represents a remarkable improvement for the coherence from engineering the local environment of our qubit using by applying the continuous microwave drive, Ω. This value is two orders of magnitude longer than $T_2{}^*$ for a similar superposition of the undressed states, $|\pm\rangle$, of this *kh* divacancy at the clock transition at B_z = 0. Comparing it to "natural" conditions, the same superposition at B_z = 1.2 mT displayed four orders of magnitude lower than the dressed basis $T_2{}^*$. Adding a refocusing pulse, we then measure a Hahn-echo coherence time of T_2 = 64.4 ms (Figure 5.2C). These values are among the largest values seen for an optically addressable electron spin qubit. These results are significant due to the lack of a large number of refocusing pulses used in the echo sequence and the coherence was measured in an SiC chip with natural abundance of nuclear spin species. There is one caveat though, an active feedback of the dressing drive amplitude was responsible to counteract first order coupling of fluctuations of that drive to the energy levels.

In order to discuss this, we will present a more complete picture of the energy dispersion in the dressed basis before detailing the feedback scheme.

5.2.5 Energy dispersion curves

We will use the derived the dispersion curves for magnetic fluctuations in the decoherence protected subspace Hamiltonian to understand all the fluctuations—magnetic, electrical, and thermal—that contribute to phase noise of our created superpositions through the experimental parameters we have introduced. The parameter we have the most control over is the static magnetic field, $\vec{B}$. We have the ability to perform fine scans along the cartesian axes of $\vec{B}$, and we use these scans to both show the validity of our assumptions about the dressed basis Hamiltonian and to elucidate the coherence protection mechanisms further. The dispersion curve for a perturbation of the magnetic field in the z-axis, defined as the c-axis of 4H-SiC, and along the x-axis are derived in Appendix B.

We want to evaluate how small changes in our applied static magnetic field shift the energy levels of the dressed states to measure the dispersion curves experimentally. We can add a perturbation to our setup, B, along any direction using the same electromagnets that cancel the local field. Our cancelation procedure for $\vec{B}$ (Section 4.6.7) does not prescribe a certain coordinate system to our sample and does not tell us where the z-axis of the 4H-SiC chip is, defined by the direction of the crystallographic c-axis. To align cartesian axes inside our cryostat to perform the x- and z-axis scans, we first develop a model for the magnetic field of the summation of three solenoid loops. Then we can apply positive or negative current on-demand, without spurious zero-crossing errors, using a single 3-port current source to increase the field along a single, arbitrary

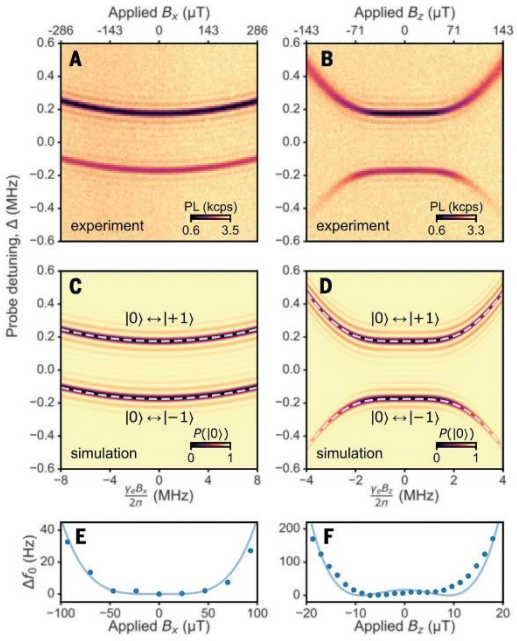

Figure 5.3. **Energy dispersion of decoherence protected subspace. (A,B):** Spin resonance spectrum of the $|0\rangle \leftrightarrow |+1\rangle$ energy levels measured by sweeping ODMR probe detuning, Δ, of resonance frequency between $|0\rangle \leftrightarrow |+\rangle$ while changing applied x-axis (A) and z-axis (B) magnetic fields offsets from $\vec{B}$ = 0 mT. The PLE contrast between the upper and lower dressed state branches is a result of the contrast recovery procedure and is not indicative of unequal transition probabilities in the dressed basis. We see inhomogeneous broadening of the energy levels for high z-axis fields in (B), indicating when the spin levels are no longer fully characterized by our description of the decoherence protected subspace. **(C,D)**: Simulated spin resonance spectrum of the dressed basis Hamiltonian's driven transitions in (A, B) over the same range of applied magnetic fields. Dashed white lines indicate analytical transition energy spectra derived from Floquet analysis. (E,F) Energy difference, Δf_0, between the $|+1\rangle$ and $|-1\rangle$ states as a function of applied B_x (E) and applied B_z (F). This was measured using Ramsey interferometry of $|\psi\rangle = \frac{1}{\sqrt{2}}(|-1\rangle + |+1\rangle)$. Solid lines are a fit based on the energy differences in the decoherence-protected subspace derived from Floquet analysis (see Appendix X and Y). Error bars are smaller than the symbol size. Error bars are smaller than the points.

cartesian axis. By parameterizing our field sweeps by an angle, θ, we attempt to find a condition where scans stepped along two axis where $\theta = 90°$ shows dispersion curves with only B_x or only B_z character. The fundamental difference of B_z scans showing inverted quadratic curves away from the origin (Appendix B.) for small shifts of the magnetic field.

The resulting scans (Figure 5.3A,B), show we obtained very good agreement between the experiment and our theoretical dispersion curves for the $|\pm 1\rangle$ states in the dressed basis. The data is taken by sweeping a microwave probe detuning, Δ, and performing ODMR sweepings at different magnetic field values. When the probe is on resonance with one of the dressed states, we can measure an increase in the PLE signal due to the probe preferentially adding spin population to one of the dressed states. This population increase in the dressed bases is then read out in the undressed basis using the contrast recovery sequence.

The energy dispersion relations (Appendix B.) also give insight into the noise perturbations that our single *kh* divacancy experiences in our setup during these scans. In both cases, the magnitude of E directly increases the suppression of energy inhomogeneity so we can say that the large E of the *kh* divacancy helps greatly reduce magnetic noise. For B_x, the ratio includes the sum of the ZFS's, $F = D + E$. F being an order of magnitude larger than E, adds more suppression that is reflected in the scan showing steeper slopes for the energy dispersion under z-axis magnetic field perturbations. There is a primarily quartic suppression when the dressing drive amplitude is larger than the magnetic noise term in the Hamiltonian, $\gamma\hat{B}$. This strong, non-linear noise reduction would indicate we want to drive at as high as Rabi frequency as possible, but there is a quadratic term that competes with the quartic term. Therefore, Ω must be chosen with care. In our coherence experiments, we chose $\frac{\Omega}{2} = 350\ kHz$ which sits in the middle of two effects. It is large enough to add noise protection over the whole range of perturbations and avoid linear characteristics at the edges. It is also not too large to add extra spin energy inhomogeneity within the region of small perturbations. This value is stabilized at the input to the cryostat by a microwave bandpass filter.

5.2.6 Nuclear spin bath noise

Next, we perform Ramsey interferometry (Figure 5.3E,F) on the spin population transferred between the $|\pm 1\rangle$ dressed states to observe the frequency shift under applied magnetic fields in the z- and x-axis. We can use the Floquet dispersion equations here again to find excellent agreement with the data. Together, the magnetic vector sweeps utilizing ODMR and Ramsey interferometry show that remaining inhomogeneity from magnetic noise sets the new limit for the measured coherence in the decoherence protected subspace. Two additional checks on this understanding involve numerical simulation of the full Hamiltonian evolution and a phenomenological model of quasistatic noise of the spin bath.

For the numerical simulation of the Hamiltonian, we add the ODMR probe field, with amplitude and frequency ω', Ω':

$$\widehat{H} = D\left({S_z}^2\right) + E\left({S_x}^2 - {S_y}^2\right) + B_i S_i + \Omega\cos(\omega t)\hat{S}_z + \Omega'\cos(\omega' t)\hat{S}_x. \qquad (5.4)$$

The terms here are set to match the experimental conditions: $\Omega' = 20\ khz$, $350\ khz$, $\omega = 2E, \omega'$ sweeps a range of 1.2 MHz around the magnetic spectrum. The term $B_i S_i$ represents the swept magnetic field component. The ensemble of spins begins with 100% population into the $|0\rangle$ basis and then the population remaining is measured after $25\ \mu s$. This plot (Figure 5.3C,D) matches the experimental dispersion curves (Figure 5.3A,B) very well, including the extra bands of magnetic resonance along the bright lines. These indicate the higher order terms we neglected in the RWA of the Floquet treatment (Appendix B.) are real energy levels being sparsely populated in the ensemble experiments.

The magnetic field scans also allow us to probe the effect of fluctuations from the nuclear spin bath. We can describe this primary source of decoherence for the system as an isotropic (scalar) distribution of magnetic fluctuations. If we invert the ${T_2}^*$ for an undressed *kh* divacancy at high field in the bulk of our sample, we can define it as a frequency fluctuation, Δf:

$$\Delta f \sim \frac{1}{2{T_2}^*}. \qquad (5.5)$$

We can relate this to the field fluctuation, $B_{z,nuclear}$, due to the weakly coupling nuclear spin bath from the Zeeman effect along the dress basis z-axis. Using the uncertainty principle, we obtain an estimate of 13 μT for the upper bound of these fluctuations. This phenomenological model of the nuclear spin bath as a source of quasistatic noise gives values approximately two orders of

magnitude lower for this fluctuation when we operate at zero magnetic field, and an additional two orders of magnitude is added when operating in the decoherence-protected subspace. This adds another confirmation that our models describe the dynamics of the dressed states as it matches the approximately four orders of magnitude increase in the measured T_2^*.

5.2.7 Non-magnetic noise

So far, we have presented a number of results on the magnetic sensitivity of the decoherence-protected subspace levels aided by fine vector magnetic control. Probing electrical or temperature sensitivity is more challenging experimentally due to the lack of precise control in our system. The dc electrical landscape of the SiC sample cannot be fully controlled with the present capacitor pads, which produce too shallow of fields to fully freeze out the mobility of free charges during the course of an experiment. Electric field depletion could add more robustness to using a classical electrical device architecture to produce strong electric fields parallel to the c-axis [27]. The temperature response timescales of the local environment on the scale of the single divacancy are far too small an effect to be measured directly using our cryostat's thermometry capabilities. The ZFS terms are the key here. The local electrical and temperature fluctuations couple into the system by changing the ZFS terms. This is very important because this will affect the magnitude of the dressing drive, $2E$, and thus the validity of our assumptions underpinning the model of the dressed states. Tracking E during coherence measurements is not practical, but we can estimate the effects of the fluctuations.

We must revisit our derivation of the energy levels produced by Autler-Townes splitting (with no magnetic noise terms) from the dressing drive (Appendix B.). The dispersion of the magnetic sublevels imply D fluctuations will not contribute heavily, but the first-order sensitivity to electric field noise that the undressed basis experiences will manifest in E fluctuations. Using

this, we can estimate the upper bound of this sensitivity from the T_2^* = 163 μs of the undressed clock transition using Eq. (5.5). This gives an estimate of the spin energy inhomogeneity from the electric field perturbations to be on order 3 *khz*. Even if D did have coupling, it is an order of magnitude larger than E so it will have minimal effect on the energy inhomogeneity we measure. Furthermore, the decoherence protected subspace adds first-order protection to the fluctuations in the ZFS magnitudes, resulting in two orders of magnitudes better protection from the electric field noise present. The first-order protection also applies to the longitudinal ZFS, translating the property to temperature fluctuations as well.

5.2.8 Dressing drive feedback

So far, we have assumed no noise in the dressing drive amplitude Ω or the frequency ω. What remains is to evaluate the effects directly related to Ω noise. The dispersion equations (Appendix B.) show linear shifts in the dressed state energy levels occur due to a shift in the dressing drive amplitude, $\delta\Omega$. This shift also will cause a change in the Rabi frequency during coherence measurements to artificially shorten the Ramsey measurements from what the spin system will measure from the noise sources present in the host crystal. The amplitude can be tracked during the course of the experiment though. This means that the part of the noise profile of Ω that is quasistatic with respect to the timescales of the experiment, set by the speed of the Rabi drive, can be mitigated using an active feedback scheme if it contributes to observable error in the coherence times.

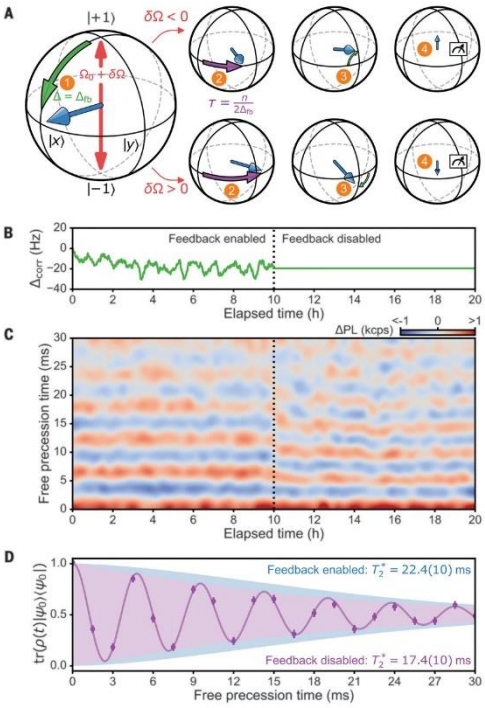

Figure 5.4. **Active feedback of dressed state spin resonance. (A):** Illustration of the feedback protocol described in detail in Section 5.2.8 that enables stabilization of the energy levels of the spin energy levels of the dressed states created when driving the *kh* divacancy with a single microwave tone. **(B):** We show the feedback sequence's correction to the frequency of the transition $|+1\rangle \leftrightarrow |-1\rangle$ during a 10 hr. time period. The second 10 hr. time period had no feedback applied. **(C):** Heat map of PLE signal showing Ramsey free precession of the superposition $|\psi\rangle = \frac{1}{\sqrt{2}}(|-1\rangle + |+1\rangle)|0\rangle \leftrightarrow |+1\rangle$ showing improved stabilization of a frequency detuning of 166.6 Hz. The period with the feedback turned off shows slow drift in the resonance and the detuning fluctuates. **(D)**: Purple curve shows averaged Ramsey free precession with active feedback enabled of a superposition, $|\psi\rangle = \frac{1}{\sqrt{2}}(|-1\rangle + |+1\rangle)$, created in the dressed basis of the decoherence protected subspace at $\vec{B}$ = 0 mT. Blue envelope shows the same experiment without the active feedback, showing an increase in the measured inhomogeneity also plotted in Figure 5.2. Error bars are one standard deviation.

To make a rough estimate of the potential noise content, we observe that the oscillator circuit in our AWG that produces the dressing drive is a collection of solid-state components whose performance depends on the lab environment conditions to some degree. Besides changing pressure (both atmospheric and mechanical vibrations) and humidity, we understand temperature fluctuations to be a major source of variability in the oscillator and as well as the internal microwave amplifier and mixing components. We take the rated thermal stability of the AWG oscillator amplitude from the manufacturer, 100 ppm/°C, as the primary source of this noise after discarding the potential of the frequency response of our microwave filters not canceling higher-order noise. Combining this metric with the temperature stability rating of our laboratory, ± 0.25 °C, we could see up to 50 ppm fluctuations in $\frac{\Omega}{2\pi} = 350\ kHz$. The fluctuations in the energy levels of the dressed basis we measured from magnetic field vector sweeps are on order with this

estimate. Thus, the classical noise content of Ω in our hardware could be influencing the measured coherence values.

If this noise is present, then we should see an increase in the measured coherence times when attempting to correct for drifts in Ω. We adopt an active feedback scheme to correct for quasistatic, or "slow", noise such that in-between the sequences used to prepare and readout the spin-state during coherence experiments, we measure an "error signal" that can be used to adjust the dressing drive amplitude before the next measurement. Below are the steps describing this feedback labeled by descriptors.

1. **Initial state preparation.** An off-resonant light pulse prepares the spin into the $|0\rangle$ state. The pulse is calibrated to be long enough to ensure high fidelity state preparation but not reduce the signal to noise. The continuous dressing drive switch is toggled on, mixing non-adiabatically the empty $|\pm\rangle$ into $|\pm 1\rangle$ states. A π pulse rotates the spin population into the $|+1\rangle$ state.

2. **Superposition precession.** Using the Bloch sphere picture, the state is then rotated into the equator along the x-axis with a $\frac{\pi}{2}$ pulse. The pulse is done with Rabi frequency, Ω, detuned by a set amount, Ω_d, causing a precession of the spin in the equator. We wait for a free-precession time τ_d, where $\tau_d \Omega_d = \frac{\pi}{2}$ so that the superposition would rotate just long enough to line up exactly on the y-axis of the Bloch sphere.

3. **Error signal measurement.** This is where the error in the drive amplitude, $\delta\Omega$, enters the picture. The superposition will either make a positive or negative angle with respect to the y-axis in the xy-plane depending on the magnitude of $\delta\Omega$. The superposition is then attempted to be rotated back onto the z-axis, where the projection onto that axis is measured as a change in the measured PLE signal as an error signal proportional to $\delta\Omega$. The $\frac{\pi}{2}$ rotation in the equator ensures

that the error signal is positive (negative) if $\delta\Omega$ is positive (negative) at the point in the plot of the decaying sine curve of the single point in a Ramsey measurement with the steepest slope as it crosses the time axis. Due to this choice, $\tau_d = 15$ ms, and $\Omega_d = 16.66$ Hz, we obtain sensitivity to and can correct for $\delta\Omega$ on order of 30 Hz with drift timescales of a few minutes.

Averaging T_2^* in the $|\pm 1\rangle$ basis over the course of several hours while performing this feedback every minute between repeated sequences of the Ramsey measurement gives a modest increase in the coherence time. This indicates that our feedback protocol was successful at mitigating some of the energy inhomogeneity in the system due to the quasistatic noise present in the dressing drive amplitude. It should be noted that the corrections implemented by the feedback are incapable of differentiating between drifts in Ω or other quasistatic drifts present in the electromagnetic fields coupling to the spin system from the host crystal. Thus, we can label our active feedback as a mechanism to track the noise content of other inhomogeneity present to reveal the coherence times this system can reach when under the effects of noise with faster fluctuation timescales than our active feedback can correct. Further characterization of the spin bath properties could give insight into the remaining noise sources. Any remaining noise from electronics and microwave circuitry would have to be more carefully checked in future experiments.

5.2.9 Conclusion

In this chapter, we described the effects of adding a single continuous microwave drive tone to an avoid crossing in the *kh* divacancy spin-1 ground-state. The result was a dramatic improvement of the inhomogeneous dephasing time and the Hahn-echo coherence time of a spin qubit superposition prepared in the upper branch of the dressed basis produced by Autler-Townes splitting of the undressed levels making up the clock transition. The extended coherence times are due to higher-order protection from magnetic, electric, and temperature fluctuations present in the

4H-SiC crystal due to the dressed basis energy dispersion taking on quadratic or quartic protection from these fluctuations based on the magnitude of the transverse and longitudinal ZFS of the *kh* divacancy. A powerful feature of this result is that the coherence extension is compatible with established noise suppression techniques in 4H-SiC. Charge depletion has shown coherence enhancement of the *kh* divacancy [82] and can also lead to observation of transform limited optical linewidths [25,27]. Dynamically decoupling is not necessary to reach the measured coherence values, but it could be implemented in this system for longer coherences. Also, spin bath driving and spin bath hyperpolarization can reduce the remaining nuclear spin effects on the measured inhomogeneity. Of course, simply removing the nuclear spins using isotopic purification will reduce the effects of the bath on the spin superposition's phase coherence [18–20].

The few key factors necessary for the implementation of this technique make it attractive for usage in other quantum spin systems with similar energy levels. Namely, any quantum system with three or more levels where an avoided crossing forms between two of them lends itself to adding a continuous microwave tone at the frequency of the avoided crossing to form a dressed basis with a drivable transition. In order to produce similar initialization and readout scheme, the system should possess an auxiliary state accessible with probe tones to transfer qubit population to the now-dressed levels. Critically, systems that satisfy this criteria and have a larger magnitude of the transverse ZFS can expect potentially better decoherence protection. Even just in 4H-SiC, there are two such candidates: *hk* divacancy ($E/2\pi$ = 82.0 MHz [41]) and the basally oriented nitrogen-vacancy center ($E/2\pi$ = 103 MHz [83]). The always-on aspect of the drive could also be the basis of "continuous dynamical decoupling" schemes by modulating the continuous drive. [84] Outside of SiC, recently, the hexagonal boron nitride divacancy showed $E/2\pi$ = 658 MHz [85].

There are a host of other spin qubit candidates, including: strained nitrogen-vacancy centers [29], phosphorus [86] or bismuth [87] donors in silicon and designer molecular spins [88].

This result also positions the *kh* divacancy as a candidate for inclusion in cutting-edge quantum infrastructure applications, including coupling to various hybrid spin systems and as a long-lived quantum memory entangled with a flying qubits traveling in optical fibers. When considering coherent coupling of solid-state spins to other systems, recent advancements needed to leverage an ensemble of N spins to counteract the coupling requirements to the strong dipolar coupling strengths of superconducting resonators [29,89]. For the $T_2^* \sim 10$ milliseconds we measured in this work, that lifetime appears to enable coupling without the $\sqrt{N}$ sensitivity enhancement from using a spin ensemble. That same T_2^* regime makes the *kh* divacancy a potential choice as a memory qubit [9,90,91], which are necessary in quantum internet repeater networks to produce long-reaching quantum information state transfer. In this case though, the *kh* divacancy's NIR emission and potential low optical contrast due to overlapping optical modes in its fine structure, are drawbacks for this application. Operation at transform limited optical linewidths would solve the photon distinguishability issue, but what remains is the poor optical collection rate of photons carrying spin information. Integration with optical cavity structures could boost the emission utilizing the Purcell effect (see Section 6.3.4). Potential conversion to more favorable wavelengths for established telecom infrastructures is also a possibility with integration of an optomechanical cavity to perform state transduction (Chapter 7) using optically induced transparency (see Section 6.5.2) to shelve the divacancy photon excitation as a mechanical excitation and read it out at telecom wavelengths.

Chapter 6

PROPERTIES OF CAVITY STRUCTURES

6.1 Introduction

There are a variety of systems proposed for quantum technology applications due their possessing unique advantages of the material platform when it comes to its quantum properties. In order to capitalize on that advantage, different systems must build qubits at a wide range of length scales and energies to leverage those platform advantages [10]. The application that the work presented in Chapter 7 will address concerns frequency conversion of a NIR photon emitted from a divacancy to telecom frequencies using a hybrid spin-opto-mechanical device. The transduction would be done using energy exchange between the emitted photon mode and phononic modes present near the defect to store the photon as a mechanical excitation. The reverse process would be reading out that mechanical excitation as a telecom frequency photon. Down converting the divacancy photons potentially entangled with its spin qubit to telecom frequencies opens up avenues for city-scale quantum information distribution utilizing the current telecom C-band infrastructure at 1550 nm, which has the lowest losses of any wavelength band of ~0.2 dB/km compared to divacancy NIR emissions with ~8 dB/km losses. The central problem here is that a single emitted photon from the divacancy has a low chance to interact with a specific phonon mode and similarly for the readout at telecom frequencies.

Cavity structures can be used to trap and greatly enhance field excitations inside a specific spatial domain to boost interaction between systems. This mechanism is usually described as enhancing the coupling between systems, which can have weak- or strong-coupling regimes,

depending on the strength of the interaction relative to the decay rates of the modes. The basic principle involves having a pair of barriers that reflect energy back towards each other. The "cavity" describes the space between the barriers, where there is an increase in the energy intensity of the field compared to outside them. The rate of energy input and output across the barriers defines the quality of the cavity and will affect how any system placed inside the cavity behaves due to the cavity fields present.

This chapter will first introduce the fundamentals of interactions of optical cavities with photon emitters, e.g., atoms, where the presence of the cavity can boost the emission rate of the atom by way of the Purcell effect. The second part of this chapter will introduce the core principles of optomechanical cavities. The momentum exchange of photons can drive mechanical modes strongly under certain conditions, usually denoted by the quantum cooperativity, C_q, which describes the coupling strengths relative to the decay rates. Reaching the regime $C_q > 1$ is where the photon-phonon energy exchange can take place between the quantum mechanical ground states of both modes to complete the transduction. [92] These principles will be needed to describe the spin-opto-mechanical hybrid transduction device described in Chapter 7 where finite element modeling will be used to explain the necessary qualities and features the hybrid transduction device must have to realize high Purcell factors and high optomechanical cooperativity.

6.2 Cavity quantum electrodynamics

The first cavity interaction we will discuss is an atom strongly interacting with an optical field. In our case, the "atom" will be the electronic state of the divacancy. Interactions between quantized electromagnetic fields of high intensity and quantized matter is the subject of cavity quantum electrodynamics (CQED). CQED attempts to define the complex interactions and changes to the base system's properties when they are considered a composite cavity system [93,94]. We will

start by introducing the Jaynes-Cummings Hamiltonian to model the ideal atom-cavity system in the strong coupling regime defined in Section 6.3.4. This will enable us to define what the coupling strength is when we talk about a CQED system. After which we will define a number of other terms that describe the operation and qualities of a Fabry-Perot optical cavity system and the benefits that such a system can have in the context of hybrid quantum systems.

6.2.1 Jaynes-Cummings Hamiltonian

We first write out the constitute parts of the Hamiltonian for an atom inside an optical cavity:

$$\hat{H}_{JC} = \hat{H}_{atom} + \hat{H}_{field} + \hat{H}_{int}. \tag{6.1}$$

The atom Hamiltonian, $\hat{H}_{atom}$, in this case is simply the TLS we defined for the divacancy complex in Equation (2.9):

$$\hat{H}_{atom} = \frac{\hbar\omega_c}{2}\,(|e\rangle\langle e| - |g\rangle\langle g|). \tag{6.2}$$

Here we define ω_c as the frequency of the optical transition between a single ground state, $|g\rangle$, and excited state, $|e\rangle$. The cavity field can be represented as a quantum harmonic oscillator, which is an approximation valid for moderate cavity energies:

$$\hat{H}_{field} = \hbar\omega_c \hat{a}^\dagger \hat{a}, \tag{6.3}$$

where ω_c is the frequency of the cavity. The operators $\hat{a}^\dagger$ and $\hat{a}$ are the photon number creation and annihilation operators, respectively. Their produce, $\hat{a}^\dagger\hat{a}$ is called the photon number operator and understood as adding or removing discrete photons from the cavity. In reality, ω_c will be described by some distribution of frequencies that the barriers of the cavity are designed to reflect,

usually with a gaussian or Lorentzian distribution. How close in resonance the systems are can increase the strength of the cavity coupling. The final term, $\widehat{H}_{int}$, describes the interaction between the atom and field and must be treated with care. Starting with the semi-classical dipole interaction we wrote in Eq. (2.16) when describing electric field interaction with the divacancy, we add knowledge of the electron's position, $\vec{d} = e_c\vec{r}$, to write:

$$\widehat{H}_{int} = -e_c\hat{r} \cdot \hat{E}, \tag{6.4}$$

where e_c is the electron charge. This term can be made quantum mechanical by rewriting $e_c\hat{r}$ in terms of dipole moment matrix elements and atom transition operators and using the quantum operator term for the electric field, $\hat{E}$. [95] We obtain after simplification a compact form for the interaction Hamiltonian:

$$\widehat{H}_{int} = i\hbar(g^*(\vec{r})\hat{a}^\dagger\hat{\sigma}_- - g(\vec{r})\hat{a}\hat{\sigma}_+). \tag{6.5}$$

Here $\hat{\sigma}_+ = |e\rangle\langle g|$) and $\hat{\sigma}_- = |g\rangle\langle e|$ are the atomic rasing and lowering operators respectively. We will discuss in greater detail in the next section the emitter-field coupling for the atomic state at some position in the cavity, $g(\vec{r})$. For now, we will make a few points about the eigenstates of the total Jaynes-Cummings Hamiltonian constructed from the three terms in Eq. (6.1). The states of the bare atom and field are from different Hilbert spaces that must be reconciled in the interaction picture. The atomic states are described again by our TLS qubit picture of a ground and excited state, while the field states are called Fock states and describe photon number. The main difference is that Fock states can have n-dimensional matrix representation. This means tensor products between the basis states will define the new best eigenbasis for the composite cavity system. A formal treatment of these states will not be explored by this thesis. At the single excitation level

though, the system can be considered to undergo state transfer in the same way as when we discussed it for a single TLS when we considered an electron spin qubit. A single photon inside the cavity can be described as undergoing Rabi oscillation to excite the atomic state, and vice-versa. Such a transfer of energy can be understood by a state transformation:

$$\psi(t=0) = |g,n\rangle \rightarrow \psi(t>0) = |e,n-1\rangle. \tag{6.6}$$

Here an optical cavity initially containing n photons gives up one of them to excite the atom when driven. The quantum state basis here is $|m,n\rangle$, where $m = e/g$ describes the ground or excited state and n describes the photon population of the cavity.

6.2.2 Emitter-field coupling

We are interested in defining the interaction strength between the atom and the cavity under the Jaynes-Cummings model. The coupling strength, g, is typically used to describe how well two constitute systems couple to each other in a hybrid quantum system. We are interested in calculating $g(\vec{r})$ we wrote in the Jaynes-Cummings Hamiltonian.

Following the treatment of references, [95], we write out the full form of the emitter-field coupling:

$$g(\vec{r}) = \frac{1}{\hbar}\sqrt{\frac{\hbar\omega_c}{2V_{mode}\max\left(\varepsilon(\vec{r})\left|\vec{E}(\vec{r})\right|^2\right)}}\,\vec{\mu}_{eg}\cdot\vec{E}(\vec{r}). \tag{6.7}$$

The frequency of the optical transition is ω_o and $\vec{E}(\vec{r}) = \hat{E}E(\vec{r})$ describes the magnitude of the electric field in direction $\hat{E}$ in all space. The dipole matrix element of our atomic transition is $\vec{\mu}_{eg} = \langle e|e_c\hat{r}|g\rangle$, whose magnitude we will discuss below. The product $\varepsilon(\vec{r})\left|\vec{E}(\vec{r})\right|^2$ describes the energy density of the optical field at any point in space, where we are particularly interested in the

maximum value, at $\vec{r} = \vec{r}_m$. Lastly, V_{mode}, defined below in Eq. (6.9), is a geometric parameter called the cavity mode volume. In order to make this equation tractable, we will make a few assumptions about the system. Assuming we can apply a laser source of photons with arbitrary polarization into our cavity, we can choose any direction of its electric field at $\vec{r}$, namely, we want it parallel to the dipole direction. If we also place our atom at the point of maximum electric field energy density, the vectors drop out of the equation, and we obtain the maximum estimation for the emitter field coupling:

$$g_{e,o} = \mu_{eg}\sqrt{\frac{\omega_c}{2\hbar V_{mode}\varepsilon_{max}}}. \tag{6.8}$$

We add subscripts here to denote this as the emitter-optical coupling we will explicitly calculate in Chapter 7 using optical mode simulations of the hybrid cavity system. To complete this calculation, we need values for the cavity mode volume and the dipole magnitude. The mode volume requires knowledge of the spatial domain of the cavity in order to take a volume integral over the electric field energy density[95]:

$$V_{mode} = \frac{\iiint \varepsilon(\vec{r})\left|\vec{E}(\vec{r})\right|^2 d^3\vec{r}}{\max\left(\varepsilon(\vec{r})\left|\vec{E}(\vec{r})\right|^2\right)}. \tag{6.9}$$

An important thing to note is that $g_{e,o}$ is inversely related to V_{mode}. Thus, the dimensions of a cavity should be minimized to increase the coupling. This point has driven much miniaturization in the fields of optomechanical and photonic cavities when it comes to fabricating micro- and nano-scale cavity volumes. On the other hand, maximizing the electric field strength will increase the light-matter coupling in the cavity. These two goals are sometimes at odds and new cavity

designs are necessary to made headway. Expressing the above equation as ratio of the wavelength to the index of refraction of the material is typical for such systems:

$$V_{mode} = Vol * \left(\frac{\lambda_0}{n}\right)^3. \tag{6.10}$$

Here Vol is a unitless parameter that encapsulates the geometry of the system, λ_0 is the cavity wavelength, and n is the material's index of refraction. This allows an agnostic comparator between cavity designs. Mode volumes on the order of $\left(\frac{\lambda_0}{n}\right)^3$ have been realized for diamond and SiC systems and the state-of-the-art continues to push for lower values to increase coupling efficiency. Scaling down a device always comes with some tradeoffs in device performance or ease of construction.

The final parameter we must define in Eq. (6.8) is the dipole magnitude, μ_{eg}, which encodes information about the an optical transition's dynamics under excitation. This value is closely related to the spontaneous emission rate of the atom in the cavity (see Section 6.3.1). It can be understood as a factor in the matrix element in the Hamiltonian of the field that drives a transition between the ground and excited states. The larger the μ_{eg} the larger the "Rabi rate" of the cycling during continuous optical driving of the transition. There is an equation that relates the excited state lifetime of an emitter, Γ_0, to μ_{eg}, as well as a number of other parameters that describe the emission properties of the atom [96]:

$$\Gamma_0 = \frac{1}{\beta}\left(\frac{3n^{5/2}}{2n^2+1}\right)^2 \frac{{\mu_{eg}}^2 {\omega_c}^3}{3\pi\epsilon_0\hbar c^3}. \tag{6.11}$$

The variables c and ϵ_0 are the fundamental constants for the speed of light and the vacuum permittivity and n is the index of refraction of the host crystal for the emitter. The parameter β is the fraction of the decay rate due to spontaneous emission at the transition matched to the cavity's fundamental frequency. This is just the product of the Debye-Waller factor, DWF, defined in Section 3.2.1 and the radiative efficiency for the emitter, RE:

$$\beta = DWF * RE. \tag{6.12}$$

The excited state lifetime as well as the Debye-Waller factor and radiative efficiency can all be experimentally measured. Thus, we have a method to calculate the emitter-cavity coupling using known constants, experimentally measured values, and an estimation of the cavity mode volume from knowledge of its geometric domain and electric field distribution.

6.3 Fabry-Perot cavity parameters

Having defined the Hamiltonian for a CQED system and discussed some of the important parameters and states that the system is described by, we now will discuss several parameters central to discussing energy exchange for optical cavities. The goal is to be able to describe the properties of high-performance Fabry-Perot cavities in the context of hybrid quantum systems. Many of these parameters apply to the description of mechanical cavity interactions as well, as we will see in the rest of the sections of this chapter.

A Fabry-Perot cavity is a specific geometry of optical cavity, and perhaps the simplest form, as it is composed of just two planar mirrors separated by a distance, L. The planar Fabry-

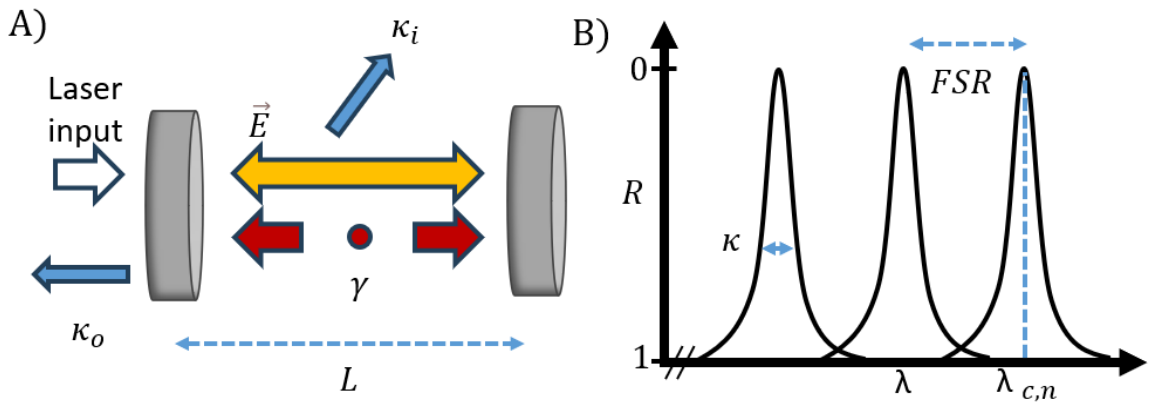

Figure 6.1. **Linear Fabry-Perot cavity coupled to emitter (A):** Pair of mirrors separated by a length, L, forming a Fabry-Perot cavity. White: laser input at variable frequency through input port mirror. The cavity field, $\vec{E}$ (yellow), is determined by the combination of the laser input, light field from the emitter with spontaneous emission rate γ (red), and the total leakage of photons from internal (κ_i) and external (κ_o) decay rates. **(B):** The linewidth of the resonances upon scanning a probe laser, ω and collecting the reflected light, R, shows resonance conditions of zero reflectance at the harmonics of the fundamental standing wave resonances of $\lambda_{c,n} = 2L/n$, where n is an integer and the spacing is the free spectral range FSR = $c/2L$. The second mirror is assumed to have perfect reflectance, making this a single-sided Fabry-Perot cavity. The linewidths are equal to the total cavity decay rate $\kappa = \kappa_i + \kappa_o$.

Perot cavity is actually the limiting case for a cavity composed of two circular arcs of radius, R, where the radius is infinite. The distance L sets the frequencies of standing waves that result when traveling photonic waves transmit through the backside of one of the mirrors. The optical properties of the mirrors are key to determining the cavity behavior. Coatings can change the reflectivity/transmissivity of either of the sides of both mirrors, leading to a wide variety of cavity responses to the excitation beam. In the following sub-sections, we will define the major parameters to describe the behavior of a Fabry-Perot as denoted in Figure 6.1.

6.3.1 Spontaneous emission rate

The spontaneous emission rate, γ, describes the rate of photon emission for an atom or defect complex as if the emitter was in a vacuum [95]:

$$\gamma = \frac{{\mu_{eg}}^2 {\omega_c}^3}{6\pi\epsilon_0 \hbar c^3}. \tag{6.13}$$

In fact, Equation (6.11) can be understood as modification of the above equation as the excited state lifetime, Γ_0 is simply $\frac{1}{\gamma}$. The modification comes from the interactions of the emitted photons with the crystal lattice. Any single photon emitted can either not physically enter the cavity due to its trajectory not overlapping with the spatial mode of the cavity or by exchanging energy with the lattice so as to not be on resonance with the cavity anymore.

Choosing emitters with higher spontaneous emission rates means more photons are likely to be inside the cavity at any one time and increase the probability of light-matter interactions. Experimentally, this means choosing emitters with higher count rates, $Cts(t)$, as measured directly from the exponential decay of the excited state population after an optical pulse on resonance:

$$Cts(t) = e^{-\gamma t}. \tag{6.14}$$

One possible drawback to higher emission rates is a broader spectral linewidth for the optical lines. In systems where several spectral lines are close together, potential overlap between them can increase the complexity of performing optical control pulses on qubits. When these pulses are initializing the states of electron spin qubits, the fidelity of the initial superposition can suffer. When the pulses are reading out the information of states, $Cts(t)$ can contain spurious counts from

a transition that does not contain quantum information. The impact of broader emission lines for the operation of high-performance cavities will be elucidated in the following sections.

6.3.2 Quality factor and decay rates

An important metric for defining the cavity's ability to confine light around an atom in a CQED system is its quality factor, Q. Q is notorious for having several different interpretations under different contexts. Much of this comes from the fact that confining a light field has both a spatial and a temporal factor. If we consider a CQED system in a vacuum that perfectly contains a certain optical mode for long times, $t \to \infty$, then its $Q \to \infty$ as well. In the laboratory, if we inject light into our cavity, then on some timescale, Q may as well be infinite as the light has not escaped the boundary we define as our cavity. But for $t \to \infty$, that light will reveal the imperfections of our confinement. Unless we continue to expand the geometric bounds of our cavity, at some point we must characterize that photon loss rate of the small device designed to tightly confine light instead of a wider description that includes light that has diffused on the way to some other optical element in the system. In fact, several cavity designs want a specific loss rate as that is the light that can carry quantum information from the emitter out of the cavity to another part of the hybrid quantum system.

Following this description, one definition for the quality factor is:

$$Q \equiv 2\pi \frac{Energy\ in\ cavity}{Energy\ lost\ per\ cycle}. \tag{6.15}$$

Where up to some constants, the quality factor is defined as the energy content of the cavity per energy lost to dampening processes due to imperfections of the boundaries keeping the photons contained. The factor 2π enters from Q being defined as a time constant that describes the

timescale for the cavity to reduce to $\frac{1}{e}$ of its starting energy content. Measuring these energy values precisely in a nanostructure would be fantastically difficult, so the above equation is usually reserved for understanding of the underlying energy exchange processes that define a cavity's effectiveness.

To add some numerical context, Q's on order of a million have been achieved [97] for NIR photonic cavities in SiC nano-platforms but values even in the thousands are useful in several contexts for emitters in hybrid quantum systems, with $Q = 10{,}000$ usually the lower bound for being called excellent quality factors.

An experimental way to measure the quality factor is to vary the frequency of a laser addressing a cavity and measure the amount of light that is transmitted, or in other words, measuring the average amount of light that is not confined by the cavity. This transmission spectrum will usually reveal a Lorentzian profile centered at the cavity's resonance condition, ω_c, that has a certain linewidth characterized by a full-width half-maximum, $FWHM$.The quality factor is found by:

$$Q = \frac{\omega_c}{FWHM}. \tag{6.16}$$

This is called the bandwidth definition of the quality factor and is typically the easiest way to measure it.

A way to merge the energy and bandwidth interpretations of the quality factor is to consider the FWHM of the spectral response of the cavity as a decay rate for the total energy exiting the

cavity. This gives us a way to experimentally measure the quality factor when we can measure the transmission or reflection spectrum of the light exiting or reflected from a cavity using the relation:

$$Q = \frac{\omega_c}{\kappa} \tag{6.17}$$

In certain contexts, it is sometimes useful to consider both internal and external decay rates κ_i and κ_o to describe physical processes that remove energy from the cavity in different ways. The internal decay rate κ_i describes all the loss mechanisms between the cavity boundaries that removes energy from the cavity, i.e., transfers it to another field preventing it from interacting coherently with the emitter under the Jaynes-Cummings picture. In a vacuum Fabry-Perot cavity, there might be residual atmosphere of gas that the electric field can excite and release photons of non-resonant light. The external decay rates usually encompass the reflective properties of the boundaries at the optical wavelength of the cavity. The external decay rate, κ_o, defines the energy lost by fields carrying energy through the cavity boundaries, or for a Fabry-Perot cavity, this describes light leaking through the mirrors. The sum of these is the total decay rate:

$$\kappa = \kappa_i + \kappa_o \tag{6.18}$$

A useful descriptor for these decay rates is the overcoupling factor, defined as:

$$\eta_c = \frac{\kappa_o}{\kappa} \tag{6.19}$$

The overcoupling factor denotes the percentage of light lost through one of the Fabry-Perot cavity ports, based on the optical properties of that mirror. We can rearrange this equation to remove κ_o, which can be difficult to measure:

$$\kappa = \frac{\kappa_i}{1 - \eta_c} \tag{6.20}$$

This relation will be useful in Chapter 7 when we wish to consider the optomechanical properties of the proposed transduction scheme in relation to realistic cavity linewidths based on estimations of their scattering losses due to the surface roughness of SiC.

6.3.3 Finesse and free spectral range

Another parameter commonly used to describe a cavity's operation is the finesse, $\mathcal{F}$. It is defined as the number round trips a photon takes inside a cavity before the energy content decays to $\frac{1}{e}$ of its starting value. The finesse of a Fabry-Perot cavity is connected to the free spectral range (FSR) of the cavity spectrum through the relation:

$$\mathcal{F} = \frac{FSR}{FWHM} = \frac{FSR}{\kappa}. \tag{6.21}$$

This makes the finesse and the quality factor very closely related. For a vacuum Fabry-Perot cavity, there will be an infinite number of resonances spaced by the FSR from the relation:

$$FSR = \frac{c}{2L}, \tag{6.22}$$

Where L again is the distance between the mirrors. Since the FSR is related to the round trip length, increasing the cavity length while keeping the energy losses constant will keep the finesse constant but increase the quality factor.

We now have all the parameters to estimate the linewidth, κ (Eq. (6.18)), of a Fabry-Perot cavity, given certain assumptions of the internal and external losses. If we assume the transmission losses through one of the mirrors is zero compared to the other mirror, we have a single-sided cavity, whose surface roughness can be assumed to be the dominant internal loss channel. The roundtrip loss, RTL can be assumed to be [98]:

$$RTL = \left(\frac{4\pi\sigma_{RMS}}{\lambda_c}\right)^2 \tag{6.23}$$

The finesse only for the internal processes under this assumption is:

$$\mathcal{F}_i = \frac{2\pi}{2RTL} \tag{6.24}$$

Then this can be used to calculate κ_i, which, along with choosing an overcoupling by tuning the transmissive properties of the mirror of the single-sided cavity to set its overcoupling ratio, the linewidth of the cavity can be defined. The optical cavity quality factor can also be calculated from the total linewidth.

6.3.4 Purcell factor and cooperativity

Now we will introduce one of the main enhancements that a cavity system provides to a solid-state emitter used for qubit applications. The emitter in a cavity system experiences an increase in its vacuum spontaneous radiative rate, γ, defined in Eq. (6.13), by a ratio defined as the Purcell factor, F:

$$F = \frac{\gamma_c}{\gamma}, \tag{6.25}$$

Here γ_c is the enhanced emission rate. This higher count rate by implementing a cavity architecture around a qubit with an optical interface like the divacancy can greatly improve the efficiency of reading out the quantum information of its spin encoded in emitted photons.

Purcell enhancement is actually seen in a system not quite in the strong-coupling regime of the Jaynes-Cummings model, in what is called the Purcell regime coupling regime. These different regimes are defined by the relative coupling between the cavity and the emitter and their individual decay rates. First, we describe the weak coupling where the emitter and cavity linewidths fulfill the condition:

$$\gamma, \kappa > g_{e,o} \, , \tag{6.26}$$

Here the system linewidths are larger than the emitter-cavity coupling between them. This regime is not very useful from a practical standpoint. Using the decay rate definitions for the linewidths, it is clear energy is exiting the cavity too fast to see much energy exchange between the emitter and the cavity.

One can now talk about the Purcell regime, where we have a slightly more favorable ordering:

$$\kappa > g_{e,o} > \gamma. \tag{6.27}$$

For a cavity system in the Purcell regime, consider a single photon emitted by the atom. On average, just as in the weak coupling regime, it will interact with the cavity before being reabsorbed by the atom. The $g_{e,o} > \gamma$ condition though ensures there is an increase in the density of photonic states in the cavity due to state mixing, and this will increase the emission rate of the atom.

Under this condition, we can rewrite the Purcell factor in terms of the emitter cavity coupling defined in Eq. (6.8) for a host crystal of index of refraction, n [95]:

$$F = \frac{2\left|g_{e,o}(\vec{r})\right|^2}{\kappa n \gamma}. \tag{6.28}$$

This indicates that the maximum Purcell factor will be achieved when the maximum coupling rate is also achieved (when the emitter dipole is aligned to the field and at the field maximum), so we can simplify the equation to:

$$F = \frac{3}{4\pi}\left(\frac{\lambda_0}{n}\right)^3 \frac{Q}{V_{mode}}. \tag{6.29}$$

This form is useful because it makes it clear that the ratio $\frac{Q}{V_{mode}}$ is important for maximizing the enhanced emission from the atom inside the cavity. If the confinement of the electric field is sacrificed by reducing the size of the cavity, the rate of photons emitted from the system might not drastically increase. Though we do not even have to reach the strong coupling regime to see an increase in counts due to Eq. (6.28) because the relation $g_{e,o} > \gamma$ will ensure $F > 1$.

The last regime of interest is the strong coupling regime:

$$g_{e,o} > \gamma, \kappa. \tag{6.30}$$

Here we see the coupling outperforms both the loss mechanisms of the spontaneous emission rate and cavity leakage rate. Here we will introduce the last CQED parameter of this section, the

cooperativity, which helps unify the boundaries between the weak and strong coupled regimes. The cooperativity, $C_{e,o}$, is defined for an optical cavity as:

$$C_{e,o} = \frac{{g_{e,o}}^2}{2\kappa\gamma}. \tag{6.31}$$

This definition means that $C_{e,o} \gg 1$ can indicate we have very strong coupling between the emitter and cavity, and thus the Jaynes-Cummings picture will make good predictions for the behavior of the system. It is this regime that is sought after for hybrid quantum systems due to coherent quantum state transfer demanding strong coupling between the states of the system to counteract all the loss mechanisms at play. Yet, simply reaching the Purcell regime is very useful as we gain an increase in photon collection efficiency per shot.

6.4 Optomechanical cavities

The other type of cavity mode we will investigate in Chapter 7 is a mechanical cavity that supports a certain resonance frequency of phonon standing waves between "phononic mirrors", made of distributed Bragg reflector stacks to be discussed later in that chapter. Mechanical cavities operate under many of the same principles as optical cavities. Resonance frequency, decay rates, quality factor, finesse, and cooperativity are all things that can be discussed for mechanical cavities in much the same way as in the previous sections. We are interested in mechanical cavities in the context of cavity optomechanics, where the radiation pressure forces from light mediates interactions between the mechanical and optical modes. One interaction is motional cooling where if the optomechanical interaction is strong enough, laser tones can transfer energy out of a mechanical mode to reach its quantum ground state. This operating point is a prerequisite for considering any quantum state transfer schemes between the optical and mechanical modes,

including the one discussed in Chapter 7 based on optical mechanical induced transparency to down-convert divacancy photons to a phononic mode and subsequent optical readout at telecom frequencies.

The rest of the sections in this chapter will be devoted to first discussing the quantum harmonic oscillator Hamiltonian representation of an optomechanical system. Specifically, the calculation of the phonon-photon coupling will be described and how this influences the quantum cooperativity of the system. The threshold coupling requirements for that cooperativity for operating the system at its quantum ground state will be discussed in the context of the cavity parameters for the optical and mechanical modes.

6.4.1 Optomechanical Hamiltonian

The basic understanding of the optomechanical interaction can be thought of as the mass of the photons in an optical cavity causing the mirrors to translate. If the effect is large enough, such translation can produce vibrational waves, i.e. phonon modes, which if confined, can been seen to have a resonance condition in the cavity, with separate boundary conditions. At the quantum mechanical level, this system is composed of a pair of interacting quantum harmonic oscillators, one radiation mode and one vibrational mode (Figure 6.2). As always, we write the system Hamiltonian as a sum of the individual parts:

$$\hat{H}_{OM} = \hat{H}_{rad} + \hat{H}_{mech} + \hat{H}_{int} = \hbar\omega_c \hat{a}^\dagger \hat{a} + \hbar\Omega_m \hat{b}^\dagger \hat{b} + \hat{H}_{int}. \tag{6.32}$$

This is the simplest representation of the optomechanical Hamiltonian, $\hat{H}_{OM}$, involving only one optical and mechanical resonance frequency, ω_c and Ω_m, respectively, which is valid normally for small displacements present in many experimental realizations of this system [99]. The radiation term, $\hat{H}_{rad}$, is the same as introduced in Eq. (6.3), and $\hat{H}_{mech}$ is another quantum harmonic

oscillator with a phonon number operator, $\hat{b}^{\dagger}\hat{b}$. We neglect the constant contribution of $\frac{1}{2}\hbar\Omega_m$ added to $\widehat{H}_{mech}$. We assume this Hamiltonian describes an optical cavity with at least one movable mirror, translating along the x-axis, so the optical cavity resonance frequency is modulated by the amplitude of that mechanical motion. If we write this parametric coupling only considering up to the linear term, we have:

$$\omega_c(x) \approx \omega_c + x\frac{\partial\omega_c}{\partial x}. \tag{6.33}$$

Here we define the optical frequency shift per displacement, G, as:

$$G = -\frac{\partial\omega_c}{\partial x}. \tag{6.34}$$

The sign indicates that the positive x direction increases the cavity length, L, and would decrease the resonance frequency. Plugging into the Hamiltonian we have:

$$\hbar\omega_c\hat{a}^{\dagger}\hat{a} \approx \hbar(\omega_c - \hat{x}G)\hat{a}^{\dagger}\hat{a} \tag{6.35}$$

We introduce the position operator, $\hat{x}$, and the momentum operator, $\hat{p}$:

$$\hat{x} = x_{ZPF}\left(\hat{b} + \hat{b}^{\dagger}\right), \hat{p} = -im_{eff}\Omega_m x_{ZPF}\left(\hat{b} - \hat{b}^{\dagger}\right) \tag{6.36}$$

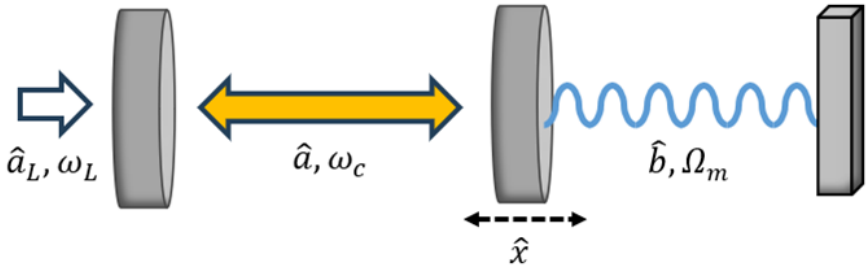

Figure 6.2. **Optomechanical cavity diagram.** A laser tone with photon mode $\hat{a}_L$ and frequency ω_L are incident on an optical cavity with photon mode $\hat{a}$ and frequency ω_c composed of two mirrors. The right mirror is allowed to move, with coordinate, $\hat{x}$. This moving boundary is a mechanical oscillator with phonon mode $\hat{b}$ and frequency Ω_m.

The zero-point fluctuation amplitude of the mechanical oscillator that describes its average position in its ground-state is [99]:

$$x_{ZPF} = \sqrt{\frac{\hbar}{2m_{eff}\Omega_m}} \tag{6.37}$$

It can also be understood as describing a spring-constant, k, in analogy to Hooke's law:

$$\Omega_m = \sqrt{\frac{k}{m_{eff}}} \tag{6.38}$$

Returning to the Hamiltonian, we can now collect terms that make up the interaction part given under the approximation of a linear optical frequency shift per displacement:

$$\hat{H}_{int} = -\hbar g_{o,m} \hat{a}^\dagger \hat{a} \left(\hat{b}^\dagger + \hat{b}\right), \tag{6.39}$$

where we have introduced the vacuum optomechanical coupling strength, $g_{o,m}$:

$$g_{o,m} = G x_{ZPF} \tag{6.40}$$

This describes the interaction strength between a single photon with a single phonon in the system and can be better to call it the single phonon optical coupling strength.

6.4.2 Linearized approximation

Here we can begin to consider the system being driven by a laser frequency, ω_L, and as usual, we gain a lot moving to the rotating frame. The unitary transformation follows similar to Section 2.5, with $\widehat{U} = e^{i\omega_L \hat{a}^\dagger \hat{a}}$ we can write the Hamiltonian as:

$$\widehat{H}_{OM} = -\hbar\Delta\hat{a}^\dagger\hat{a} + \hbar\Omega_m\hat{b}^\dagger\hat{b} - \hbar g_{o,m}\hat{a}^\dagger\hat{a}\left(\hat{b}^\dagger + \hat{b}\right). \tag{6.41}$$

We define the detuning between the optical cavity and the laser tone, $\Delta = \omega_L - \omega_{cav}$. In order to make this problem tractable, we enter the "linearized" approximation for the optomechanical interaction. Where the cavity field is built from an average amplitude, due to the presence of an average number of cavity photons, $\bar{\alpha} = \sqrt{\bar{n}_{cav}}$ to which we add a term allowed to fluctuate, $\delta\hat{a}$:

$$\hat{a} = \bar{\alpha} + \delta\hat{a}. \tag{6.42}$$

Removing a constant shift from the expansion that removes the laser driving term, and only keeping powers linear in the cavity amplitude, we have:

$$\widehat{H}_{OM} = -\hbar\Delta\hat{a}^\dagger\hat{a} + \hbar\Omega_m\hat{b}^\dagger\hat{b} - \hbar g(\delta\hat{a}^\dagger + \delta\hat{a})\left(\hat{b}^\dagger + \hat{b}\right). \tag{6.43}$$

Here we have defined a new parameter, $g = g_{o,m}\sqrt{\bar{n}_{cav}}$, we label the optomechanical coupling strength.

In the context of wanting to maximize interactions between the optical and mechanical systems, which will define the kinds of excitation transfer we can achieve in the system that can

be used to perform transduction in the device investigated in Chapter 7, we start by defining in analogy to Eq. (6.28), with the corresponding damping rates, the single phonon cooperativity:

$$C_0 = \frac{4{g_{o,m}}^2}{\kappa \Gamma_m}, \tag{6.44}$$

We define the mechanical decay rate in terms of its frequency and quality factor $\Gamma_m = \frac{\Omega_m}{Q_m}$. Maximizing this involves improving the system itself, but we can work in the high laser power regime, and we can define the optomechanical cooperativity for the situation where the optical cavity contains on average $\bar{n}_{cav}$ photons due to a certain laser drive power:

$$C = \frac{4{g_{o,m}}^2}{\kappa \Gamma_m} \bar{n}_{cav}, \tag{6.45}$$

One further consideration is the average number of thermal phonons present in the mechanical oscillator due to the thermal bath it is coupled to at a particular frequency mode. We define the quantum cooperativity:

$$C_q = \frac{C}{\bar{n}_{th}}, \tag{6.46}$$

where the phonon occupancy is given by the Boltzmann distribution for phonons:

$$\bar{n}_{th} = \frac{k_B T}{2\pi \hbar \Omega_m}. \tag{6.47}$$

Here k_B is the Boltzmann constant.

6.4.3 Bistability regime

A threshold to keep when defining how large the cavity optical field can be, is that we cannot drive our optomechanical system with infinite laser pump powers, as we would like to do to compensate for the number of intracavity photons lost through potentially large decay rates from external and internal loss channels. Similarly, if the optical decay rate is too large compared to the optomechanical coupling, we might not be in a regime where C_q or even C is larger than one.

To explain this, consider the optomechanical interaction described as a backaction effect, where the cavity decay rate adds some delay to the mechanical motion shifting the optical resonance, which changes the cavity photon occupancy, which changes the force acting on the barrier. One basic effect of this is to shift the equilibrium point of the oscillators motion. There is a driving threshold above which the system enters the "bi-stability regime" [100] and the properties of Section 6.5 will not be realizable in our system due to there being two equilibrium points leading to instability. This would prevent us from enabling a set of properties of the optomechanical system that are valid only in the "sideband-resolved regime" where the optical linewidth of the cavity is much smaller than the mechanical frequency: $\Omega_m \gg \kappa$. This includes the process of cooling the mechanical resonator to its quantum ground state (see Section 6.5.1) and a process by which optical emissions of certain frequencies can be transferred to mechanical excitations called optomechanical induced transparency (OMIT) (see Section 6.5.2). Ground-state cooling and high quantum optomechanical cooperativity ($C > 1$) are prerequisites for OMIT. With all that in mind, the bi-stability criteria [99] is given by:

$$1 = \frac{3}{2}\sqrt{3}\frac{{g_{o,m}}^2}{\Omega_m \kappa}\bar{n}_{cav,max}. \tag{6.48}$$

We will use it to estimate the maximum $\bar{n}_{cav}$ our optomechanical system can contain to calculate the highest possible optomechanical cooperativity for our system. Experimentally, this tells us there is a critical laser driving power we cannot exceed when addressing our system.

6.5 Sideband-resolved regime

In this section we want to describe a set of properties of the optomechanical system that are valid only in the "sideband-resolved regime" where the optical linewidth of the cavity is much smaller than the mechanical frequency: $\Omega_m \gg \kappa$. We want to describe the two major consequences of this regime that are relevant to our proposed transduction process in Chapter 7. The detuning most relevant to us will be $\Delta = -\Omega_m$, where driving at a red-detuned sideband of the mechanical density of states due to the optomechanical interaction will enable the process of cooling the mechanical resonator to its quantum ground state and performing OMIT.

6.5.1 Ground-state cooling

The backaction from the radiation pressure force can be considered as a linear, mechanical response affecting the mechanical oscillator. This effect can be contextualized as an additional mechanical dampening term added to the intrinsic dampening that the oscillator experiences due to friction and other physical loss channels during its motion. We write:

$$\Gamma_{eff} = \Gamma_m + \Gamma_{opt}, \tag{6.49}$$

where the additional dampening due to the optomechanical interaction, Γ_{opt}, can be either positive or negative, depending on the photon frequency relative to the center of the optical cavity, ω_c. For photons of higher frequency ($\omega > \omega_c$), they have a chance give up energy in the form of phonons entering the mechanical cavity. This would mean amplification of the mechanical motion, and we

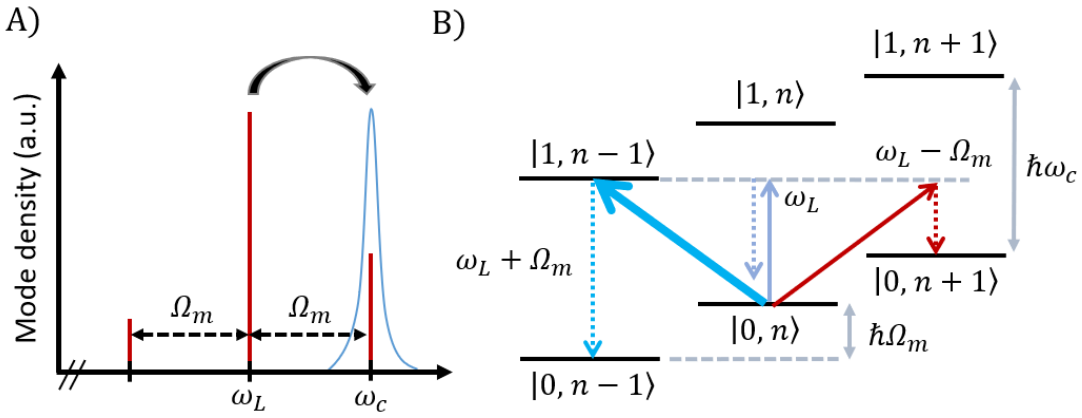

Figure 6.3. **Ground-state cooling of optomechanical system (A):** Laser tone (grey) addressing the optical cavity at frequency $\omega_L = \omega_c - \Omega_m$ achieves cooling of mechanical mode by enhancing anti-Stokes scattering (blue) and suppressing Stokes scattering (red). **(B):** Energy level diagram of the process in (A), where the state is $|n_{cav}, n_{phonon}, \rangle$. We focus on three of the motional states, with or without a photon entering the optical cavity. The anti-Stokes scattering process (blue) is the only transition on resonance with ω_L, and the other two processes are suppressed. Cooling is accomplished by the photon blue-shifting by absorbing the energy of a phonon and subsequently exiting the cavity.

can say Γ_{opt} is negative for such a process. If this process is encouraged, it could reach $\Gamma_m < \Gamma_{opt}$, leading to massive population increase in the mechanical mode leading to an unstable cavity. On the other side of the optical cavity, ($\omega < \omega_c$), photons can accept energy from phonons, leading to an increase in Γ_{opt} and less energy in the mechanical cavity. Perturbation theory of the full coupled quantum mechanical equations of motions for this system reveals that the net effect of this modification of the mechanical decay rate is that the cavity photon field contains sidebands with center frequencies located at $\omega_c \pm n * \Omega_m$ [101]. For the purpose of ground-state cooling, we only need to concentrate on the first order sidebands ($n = 1$), which can be seen when the optical cavity is driven on resonance and the transmission spectrum is measured. Another explanation says that the radiation pressure driving force and the mechanical motion become out of phase with each other and allows either positive (warming) or negative (cooling) energy transfer to occur between the optical and mechanical density of states.

If we now consider driving the optomechanical cavity with a detuned laser, we can choose to address either of the sidebands, which we call the Stokes ($\omega_c + \Omega_m$) and anti-Stokes sidebands ($\omega_c - \Omega_m$). If we are in the sideband-resolved regime, $\Omega_m \gg \kappa$, then we can be assumed to be addressing only one of the sidebands. We must consider the three different scattering processes when addressing the anti-Stokes sideband with a pump laser (Figure 6.3). From the energy level diagrams of the available states for the incident photon, only the process whereby a phonon is absorbed by the photon scattering off the optomechanical cavity is resonantly addressed. The blue-shifted photon then has a chance to carry that energy out of the optical cavity via reflection. We can utilize a relation [102] that provides a threshold for when the average minimum phonon, occupation can be made less than one:

$$\bar{n}_{min} = \left(\frac{\kappa}{4\Omega_m}\right)^2 < 1 \tag{6.50}$$

This again, plainly shows the requirement of being in the sideband-resolved regime.

6.5.2 Optomechanical induced transparency (OMIT)

If the red-detuned sideband of an optomechanical cavity can be addressed by a strong laser drive, the cavity resonance spectrum, as measured by another, weaker tone in transmission is seen to be completely transparent at the center of the optical cavity. The transmission window depth, T_{OMIT} can be shown for an overcoupled optical cavity with η_c=0.5 (Eq. (6.19)), to be [103]:

$$|T_{OMIT}|^2 = \left(\frac{C}{C+1}\right)^2, \tag{6.51}$$

Where C, the optomechanical cooperativity, is given by Eq. (6.45). Here is where the requirement high optomechanical cooperativity comes in, as $C > 1$ gives asymptotically increasing

transmission. The existence of the transmission window can physically be explained as the beating of the weak probe and strong resonant laser drive adds a temporally varying radiation pressure force. If that time dependence matches the resonant frequency of the mechanical cavity, then it will be driven and create sidebands on the strong probe tone. When the upper sideband of that strong drive (located at ω_c) interacts with the weak probe the photons scattered from the cavity experience destructive interference due to them being phase coherent. One requirement of this is phase stability of both lasers on the time scales of the cavity decay rates.

The width of the Lorentzian line shape of the transparency, Γ_{OMIT} window is given by [103]:

$$\Gamma_{OMIT} = \Gamma_m + \frac{4{g_{o,m}}^2}{\kappa}\bar{n}_{cav}. \tag{6.52}$$

This linewidth sets the bandwidth of the pulse that can be transmitted through the cavity undistorted. Γ_{OMIT} is also called the effective optomechanical dampening rate, with the term added to Γ_m arising due to the interactions with the optical cavity at a certain photon occupation, $\bar{n}_{cav}$. Thus, dampening strength can be considered as proportional to some laser power input into the optical cavity. More power input adds more dampening and widens the bandwidth.

Chapter 7

DESIGN OF A MONOLITHIC HYBRID OPTOMECHANICAL RESONATOR COUPLED TO A SPIN QUBIT

7.1 Introduction

Quantum technologies are showing remarkable progress in many domains, but no one platform is currently able to offer simultaneous solutions to the key functionalities needed for a complete quantum information platform [11]. The desired functionalities fall under broad categories, such as computation involving multi-qubit states, long-term storage of quantum superpositions, and transfer of quantum states over city-scale distances. Combining different platforms into hybrid quantum systems offers progress towards solutions [92,104] and is the current goal of many institutions.

A major hurdle for hybrid quantum systems is transferring quantum information between degrees of freedom housed in platforms that operate at vastly different energy scales. This involves development of “flying qubits” that can transfer quantum information between “stationary qubit” systems that excel at computation or long-term storage. Having a robust array of communication channels to shuttle delicate quantum states is a major goal of quantum information science [105]. It is generally considered that photons of wavelengths in the telecom band are the best candidate for flying qubits due to the low attenuation in existing optical fiber technologies. High-throughput

generation of photons at these wavelengths would allow implementation of robust entanglement protocols necessary for long-distance quantum communication. The current challenge is the development of quantum transducer platforms that can generate photons at telecom frequencies entangled to the quantum states of stationary qubit platforms, which typically are in the microwave regime. Superconducting circuits operating at microwave frequencies have shown quantum advantage in a quantum processor [6] and early implementation of quantum error correction [106]. An efficient microwave-to-optical transducer would enable the connection of these or other quantum computation architectures to communicate over long distances

A plethora of systems realizing connections between microwave and optical excitations have been studied in recent years, including optomechanical systems, atomic ensembles, electro-optical systems, organic molecules, and magnons. [107,108] Mechanical resonators especially have been studied as useful for hybrid quantum systems due to their ability to couple mechanical motion to degrees of freedom at many energy scales. These interactions enable overcoming the off-resonant processes inherent in trying to bridge the five order-of-magnitude wide energy gap between microwave and optical excitations. Circuit-QED systems coupled to mechanical oscillators can have cooperativities that overcome the myriad of lossy channels involved when coupling systems of disparate energies. Both bulk and surface phonon modes with high mechanical quality factors are being investigated that exhibit high-degrees of control over quantum states at the mechanical ground-state of these hybrid quantum systems [37]. Efficiencies as high as 47% for microwave-to-optical up-conversion has been shown using a mechanical membrane coupled to microwave resonator realizing a parametric oscillatory response that is described by an effective beam-splitter like Hamiltonian [38].

An alternative pathway towards creating telecom frequency flying qubits for various applications are the collection of optical point emitters that have demonstrated photon-mediated entanglement at short distances [9,109–114] to show the potential of long-distance quantum networks in trapped ions, quantum dots, or solid-state color center spins. The most successful of these solid-state spins so far is the nitrogen-vacancy (NV) center found in diamond. The spin state of an NV center has been reported to be entangled to a telecom-wavelength photon using difference frequency generation at an entanglement fidelity of 77% [115]. This conversion process has recently allowed heralded entanglement between two independently operated NV spin qubit network nodes separated by 10 kilometers at ~50% fidelity [116]. This technique uses periodically poled lithium niobate (ppLN) crystal waveguides to mix the 637 nm NV emission with a 1064 nm pump laser to create 1588 nm L-band telecom photons. The advantages of the NV center also include the utilization of multi-spin quantum registers in the diamond host by coupling to nuclear spins. A ten-qubit register composed of the NV center and multiple ^{13}C nuclear spins was used to create an N-qubit Greenberger-Horne-Zeilinger state [117], which are multi-qubit states necessary for doing quantum computation applications over entanglement protocols [118]. The clear successes of the NV center as an entanglement generator are remarkable, yet challenges remain. Its Debye-Waller factor (DWF) is only 3%, indicating 97% of the photons emitted are not emitted into the zero phonon line (ZPL) and these spectrally distinguishable photons are useless for entanglement. In order to boost the collection efficiency of ZPL photons to the single-shot regime, time and spectral filtering, as well as integration with a solid immersion lens to direct more counts to their detectors, have been utilized since the first demonstration of heralded entanglement of NV centers 3 m apart [9]. This low collection efficiency is one of the major factors limiting the entanglement generation rate in [119].

To address the low emission rates, integration of NV centers into open microcavities that can boost the emission rate of photons in the ZPL have been explored [120,121]. These devices exploit the Purcell effect, whereby the optical mode of an optical cavity is tuned into resonance with the wavelength of the NV spin-to-photon interface and the cavity-emitter coupling enhances the ZPL emission by the Purcell factor, F. Unfortunately, mechanical instability is inherent given the open-cavity design composed of a stationary mirror upon which is placed a diamond substrate containing the NV centers. The top mirror of the cavity is floating and can be positioned with a piezo motor to tune the cavity resonance to match the NV emission wavelength. The un-correlated mechanical motion inherent to the floating mirror cavity reportedly has limited the observed Purcell factors for NV ZPLs to values of $F \sim$ 4-30. These metric are stated to have potential for better collection efficiencies than the solid immersion lens devices. Further refinement of the open microcavity design and integration into isolated NV center qubit nodes will thus be necessary to reach faster entanglement generation rates to meet the demands of future quantum communication infrastructure.

Given the need for faster emitters at telecom wavelengths, other cavity geometries could be explored with different advantages. The result presented in this chapter will be the investigation of the feasibility of using a different solid-state color center, the divacancy in 4H-SiC, in a hybrid quantum system architecture to develop a method for generating telecom-frequency photons which could be entangled to the divacancy spin qubit. The divacancy shows promise as a spin-qubit in the areas that NV center technologies have excelled at so far. These properties, to briefly reiterate, are that the divacancy has an optical-interface for initlization and readout of spin qubits with high fidelity [40], they could offer potential multi-qubit state storage and preparation due to demonstrated coupling with nearby nuclear spin registers [21], and their ultra-long inhomogeneous

dephasing times could enable high coupling when interfacing with other qubit systems, including transmon qubits or mechanical excitations, as related in Chapter 5 Unfortunately, the natural near-infrared (NIR) photon emission wavelengths of these defect complexes are not at telecom frequencies, but are closer than the visible emission of NV centers. Divacancies unfortunately also suffers from low ZPL emission (DWF ~5-10%) and as of now, single-shot readout has only been achieved by electrical readout using spin-state to charge-state conversion [28]. The properties of the crystal host of the divacancy described in this thesis, 4H-SiC, will be pivotal in the design of a fabricated cavity device that could lead to single-shot readout of the divacancy and potential telecom transduction applications.

7.2 Overview of transduction scheme

The proposed device discussed in this chapter is a hybrid spin-opto-mechanical quantum transducer where the photon down conversion is enabled by a pair of optical cavities coupled to a mechanical cavity. The divacancy emitter will be on resonance with one the optical cavities. The outline of how the spin qubit will be readout is diagramed in Figure 7.1. A photon from the divacancy will be emitted into the first optical cavity that has a resonance matched to the divacancy's ZPL. The efficient capture of a divacancy photon by the optical cavity will be aided by the Purcell enhancement (Section 6.3.4) of the divacancy's ZPL emission rate into the cavity. Then, through an interaction known as optomechanical induced transparency (OMIT), discussed in Section 6.5.2, the photon excitation can be transferred to the mechanical cavity and then subsequently transferred, using OMIT again, to the second optical cavity whose resonance is near telecom frequency. That telecom photon can be recorded as it transmits out of that cavity, potentially carrying with it entangled quantum information about the divacancy spin state when it was originally emitted. This type of three-cavity interaction known as a beamsplitter interaction

has been implemented in many hybrid quantum systems for microwave to telecom frequency conversion at varying efficiencies [38,122–125]. Here we will mention the most important prerequisites for realizing this transduction scheme.

For the design of this cavity device, we are interested in determining the fundamental thresholds necessary to show the technique is feasible. For the optical cavities, we will require sufficient spatial containment of the optical mode addressing the divacancy to give high Purcell enhancement factors. For the mechanical cavity, a similar requirement will be needed. These translate to calculating high emitter-cavity and optomechanical coupling rates. Also, as mentioned in Section 6.5, in order to perform OMIT, we require for the optomechanical system to have quantum cooperativity satisfying $C_q > 1$, and, furthermore, operate in the side-band resolved regime, $\Omega_m \gg \kappa$, where the mechanical oscillator linewidth is resolved against the optical linewidths. This enables driving at the anti-Stokes sideband for both optical resonators and ensures the exchange rates of the photons and phonons between the resonator energy states is always larger than the leakage into the decay channels present, including the thermal bath.

We now discuss an additional criteria, based on findings from the experiment in [38]. In this work, they coupled a superconducting microwave oscillator to a membrane resonator at telecom frequencies and achieved microwave-to-optical conversion at efficiencies ~47% using the beamsplitter interaction. In our device, the divacancy takes the place of the microwave cavity. The criteria is that the optical pumps detuned from the divacancy's frequency should give a total optomechanical dampening rate during OMIT (Eq. (6.52)) equal to the bandwidth of the divacancy

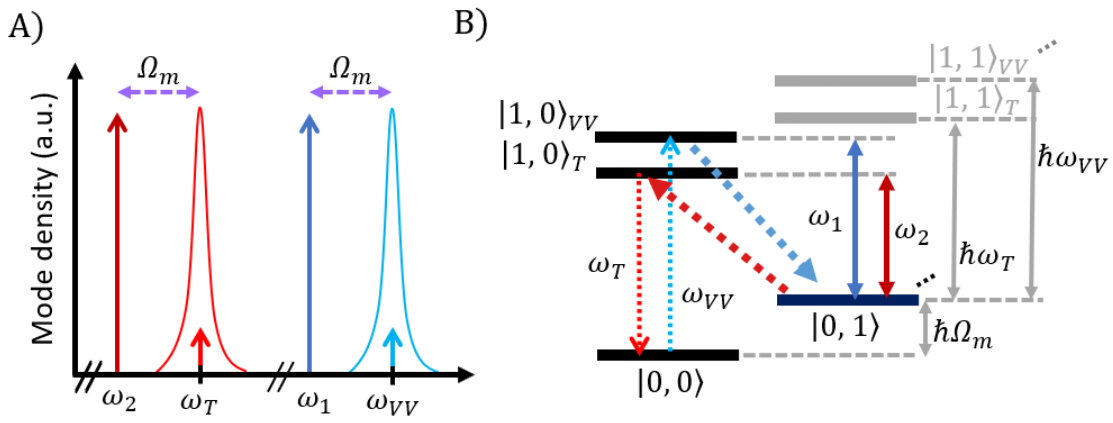

Figure 7.1. **Divacancy-to-telecom readout scheme level structure. (A):** Laser drives and optical cavity resonances for transduction readout. **(B):** Corresponding level structure of the states addressed during the readout. Upon driving at $\omega_1 = \omega_{VV} - \Omega_m$, ground-state cooling of the mechanical resonator will enable operation at the side-band resolved regime in state $|n_{cav} = 0, n_{phonon} = 0\rangle$. The proposed transduction scheme begins with a divacancy photon emitted at ω_{VV} (light-blue arrow (A)) matched to the center of the optical cavity's linewidth and populating $|1, 0\rangle_{VV}$, whereby preferential emission of a photon at ω_{VV} into the mechanical mode as a phonon is accomplished via optomechanical induced transparency ($|0, 1\rangle$) by driving at ω_1. Upon driving at ω_2, the transition to $|1, 0\rangle_T$ in the second optical cavity at ω_T will be induced. After which, emission of a telecom photon at ω_T from the second optical cavity can be detected, and the system returns to $|0, 0\rangle$.

optical emission we wish to store in the mechanical mode. This constraint is actually modified for the beamsplitter interaction as there is a second addition to the effective optomechanical damping rate due to the second cavity [38]:

$$\Gamma_{OMIT} = \Gamma_m + \frac{4{g_{o1,m}}^2}{\kappa_1}\bar{n}_{cav1} + \frac{4{g_{o2,m}}^2}{\kappa_2}\bar{n}_{cav2}, \tag{7.1}$$

where the first cavity is at the divacancy frequency and the second at telecom frequency (1550 nm). The maximum conversion efficiency is achieved when the two bandwidths are equal. In our case, we have a requirement on our bandwidth that it match a photon emitted from the divacancy after spin readout (see Section 3.3) without being too narrow to not distort the pulse, nor too wide, which would mean it could accept frequencies from one of the different spin-dependent transitions, an outcome that would ruin the spin-contrast measurement.

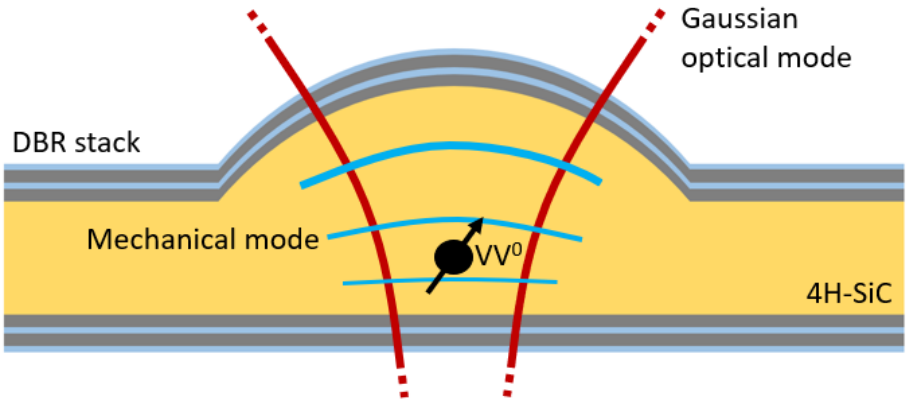

Figure 7.2. **Hybrid spin-opto-mechanical cavity device diagram.** Diagram of the proposed hybrid device showing 4H-SiC (gold) membrane with etched dome structure that allows resonant modes of optical (red) and mechanical (blue) excitations co-localize around a divacancy (black arrow) that is far (~ 2.5 μm) from the fabricated edges. The DBR stack is made of different thicknesses of alternating SiO_2 (blue) and Ta_2O_5 (grey) layers based on their indexes of refraction (Section 7.4.1).

In investigations of single divacancies, typical inhomogeneously broadened optical linewidths are on order ~200 MHz, with observed narrowing to linewidths on order ~50 MHz after charge depletion in p-i-n junction devices over several hours [27], which approaches the lifetime limited linewidths of 10 MHz [40]. One last consideration is the closeness of the spin-conserving lines corresponding to the spin states $|-\rangle$ and $|0\rangle$ in the *kh* divacancy, where there is a separation of only ~120 MHz. [25] This is all to say, we must be aware of what our predicted divacancy linewidth will be when proposing the final design of the hybrid device in order to as closely match the OMIT bandwidth with the divacancy emission. A linewidth of 100 MHz is probably sufficient to contain a 50 MHz divacancy pulse. In this result, we will focus primarily on the optical cavity directly coupling to the divacancy to show storage of divacancy photon excitations in mechanical modes is feasible for this proposed device.

7.3 Overview of transduction device

The shape considered for the transduction device is a bulk, plano-convex Fabry-Perot resonator composed of a 10-20 micron thick SiC slab etched on the top side to produce a

hemispherical structure (**Error! Reference source not found.**). This will allow the formation of co-localized optical and mechanical modes in a monolithic structure. The mirrors of the optical cavities are to be made from depositing alternating layers of tantalum oxide and silicon dioxide to create distributed Bragg

reflectors (DBR) that can be applied by a commercial vendor with custom thicknesses and layer numbers to produce the desired properties of the high-quality factor cavities. This DBR mirror design is typical for such cavity designs, but we will also investigate in Section 7.5.3 the potential of utilizing the DBR stacks to act as "phonon mirrors" at certain frequencies relevant to the experiment. This would vastly increase the mechanical quality factors achievable by preventing the phonon modes from propagating in the mechanically lossy glass layers of the DBR stack. Other systems that have seen success using monolithic microcavities with DBR mirrors are quantum dots where strong emitter-cavity coupling was achieved [126], and a high-overtone bulk acoustic wave resonator using a flip-chip geometry where the mechanical motion of the convex structure enabled swapping states between the groundstate of the mechanical oscillator and a superconducting transmon qubit [127].

One of the major benefits of the monolithic cavity design is intrinsically higher mechanical stability of the alignment of the mirrors, stated to be one of the limiting factors for quality factors for open microcavities [120,121]. This comes at the cost of almost complete loss of tunability of the optical cavity length to match its resonance with that of the divacancy. Tuning the optical cavity length, using piezo control, to match the frequency of an NV emitter is intrinsic to the device's performance because each single emitter will have some unique optical resonance due to the local environment it resides at inside the diamond. The solution to mode-matching the monolithic cavity to a divacancy ZPL could involve Stark tuning the divacancy instead of having

transverse motional degrees of freedom in an open-microcavity design. Divacancy emitters exhibit large Stark tunings if they are measured in the i-layer of a p-i-n diode junction in a doped SiC stack and driven in the reverse bias regime [27]. The large electric fields produced when a reverse bias is applied to reach a critical voltage threshold can produce stark shifts of magnitude greater than 850 GHz (hh), 200 GHz (kk), 760 GHz (*kh*) for the corresponding divacancy configuration's spin-optical interface. Given the FSR of our NIR Fabry-Perot optical cavity will be on order of 2 THz ~ $\frac{c}{2*L}$ for L ~ 10 μm, such a Stark tuning would allow more than 75% of single divacancies could be tuned into resonance if we integrate the p-i-n junction into an eventual device. For the first iteration of the proposed hybrid device, it would be possible to fabricate a large array of devices with slightly different cavity lengths and perform an exhaustive search to locate divacancies on resonance with the optical resonance. This is feasible given the densities of the single divacancies created by electron irradiation + annealing could be tuned to contain several spectrally non-overlapping optical lines from divacancies addressed by the ~1 μm diffraction-limited focus of our NIR confocal microscope.

There are several additional benefits of constructing the optomechanical cavity in SiC. Its crystal lattice possesses qualities that lend it very low mechanical losses to enable high quality factor mechanical resonators to be constructed. This can be seen by comparing the upper limit for the Q-f (product of quality factor and mechanical resonance frequency) product for SiC, Si, and diamond, a set of materials hosting strong candidates for solid-state qubits. Theoretical studies involving gives SiC the highest value of 64×10^{13} Hz, over 30x that of the other two materials [128]. Related to this, in the A*kh*iezer regime for phonon-phonon dissipation where thermal effects are negligible compared to the energy of the phonons, SiC has among the lowest dissipation [129,130]. SiC also possesses an array of qualities that enables high-precision fabrication at the

micro- and nano-scale. A technique has recently been shown to produce photonic cavities with high-Q resonators up to 10^7 in micron-scale SiC slabs bonded to a silicon substrate. This silicon carbide on insulator (4H-SiCOI) [131–133] gives us the material platform to produce a suspended membrane upon which we can fabricate hemi-spherical domes using a photoresist re-flow etch [134]. Completing the bulk microcavities involves etching away the Si substrate on the backside and patterning the DBR mirrors on both sides. These microfabrication results and intrinsic properties show SiC is a strong candidate to build an optomechanical transduction device.

The last major consideration is surface proximity in SiC structures. A previous work used a nanobeam photonic cavity to observe Purcell enhancement factor from an hh divacancy of 53 and 16 for the lower and upper branches of the ZPL its spin-optical interface, respectively [30]. The coupling to the photonic cavity increased the DWF 75% above that of natural divacancies. This study noticed both optical linewidth broadening and reduced magnetic sublevel superposition state coherence values compared to hh divacancies in the bulk. The main culprit is thought to be proximity to charge traps and crystal damage at the surface (first few nanometers) of the photoelectrochemically etched SiC. The bulk microcavity proposed in this thesis would enable the placement of the addressed emitters at least a few microns away from any etched or polished surfaces, hopefully improving the performance of their spin-optical interface.

7.3.1 Results utilizing finite-element simulations

In order to make informed decisions about the design of the monolithic microcavity structure proposed, investigations into the geometry and cavity properties of the system were conducted in the COMSOL Multiphysics finite-element simulation software program [135]. Using 2D and 3D eigenmode solvers and driven frequency spectrum studies, models of resonant electric and mechanical fields supported by the plano-convex cavity geometry can be produced and analyzed.

Conclusions can be drawn about the modeled cavity's properties, and these will inform us about the feasibility of this design with respect to the two main goals for improving the divacancy spin-qubit platform. This result focused on modeling the optical mode that would couple to the divacancy ZPL and the mechanical cavity only. The telecom wavelength optical mode was not explicitly simulated as its spatial behavior would closely mirror the divacancy wavelength optical mode.

From cavity properties estimated through simulations, we estimate a maximum Purcell enhancement achievable in this device to enhance the divacancy's ZPL emission rate by $F \approx 170$ (Eq. (6.29)) with a cavity operating at divacancy wavelength. This increase could allow the divacancy to attain optical single-shot readout of its spin state, a major goal for solid-state spin qubits [28,42] in a fabricated device that does not deleteriously broaden the optical lines due to surface proximity using the monolithic cavity design. The optomechanical properties indicate we should be able to cool the mechanical resonator to its ground state for sideband-resolved regime operation (see Section 6.5). The maximum optomechanical quantum cooperativity (Section 6.4.2) we can operate the cavity at is $C_q \approx$ 1000-5000 before the optomechanical cavity becomes unstable due to entering the bistability regime (Eq. (6.48)) and taking into account the bandwidth matching between the OMIT linewidth and the divacancy optical linewidth. There are several other properties of the cavity related to and supporting these conclusions which will be discussed in detail after the simulation methods implemented in COMSOL are introduced in the next section.

7.4 Optical resonance modes

The first step in simulating the optical mode is to determine the optimal shape for the proposed cavity device. For this, we must parameterize the optical resonances for our Faby-Perot cavity in

terms of certain geometric parameters. The resonances of a classic planar Fabry-Perot cavity composed of a pair of mirrors separated by a distance, L, occur when the relation:

$$f = \frac{c}{2L} q, \tag{7.2}$$

is satisfied given a longitudinal mode number, q, of the resonance. In order to enhance the coupling to the dipole emission of a divacancy at its ZPL, we want to utilize a plano-convex Fabry-Perot cavity geometry where the fundamental mode of our cavity will be the lowest order Hermite-Gaussian mode called the TEM00 mode. This will also allow high overlap of the excitation lasers used to address the divacancy, as our optical setup can send a diffraction-limited beam through our microscope objective to be focused on the sample surface in the vicinity of the divacancy.

The treatment of the TEM00 mode being a resonance condition for the cavity assumes the electric field at all points satisfies the paraxial approximation and the longitudinal cavity axis (along L) to be perpendicular to the polarization vector. This also means that we can have an assumption of cylindrical symmetry in all our simulations of the optical mode. When the spot size of the focused beam is on the order of the wavelength when attempting to focus gaussian beams down to diffraction limited spot sizes, the paraxial approximation can no longer be assumed. In order to check we are in the paraxial regime; we must calculate the waist diameter of our light beam on the flat mirror of the cavity.

Starting with the equation for the radius of curvature, R, and the beam waist, w, of the TEM00 wavefront:

$$R(z) = z + \frac{{z_0}^2}{z}, w(z) = w_0 \sqrt{1 + \frac{z^2}{{z_0}^2}}, \tag{7.3}$$

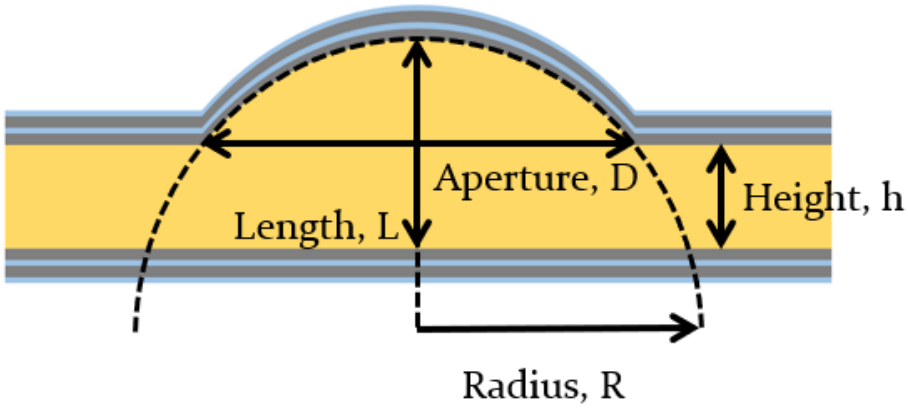

Figure 7.3. **Geometric parameters defining plano-convex cavity.** Arrows define the geometric dimensions for the hybrid device. *L* is the length of the primary, longitudinal axis of the 4H-SiC cavity. *R* is the radius of curvature of the dome structure. *h* is the residual height of the bulk 4H-SiC membrane. *D* is the diameter of the circular aperture demarcating the dome structure from the bulk membrane.

where the z axis is along the cavity axis, w_0 is the diffraction limited beam waist diameter, and z_0 is the Rayleigh range:

$$z_0 = \frac{\pi {w_0}^2}{\lambda}. \tag{7.4}$$

The intensity, I, of the Gaussian beam, averaged over an optical period is:

$$I(r,z) = \frac{2P}{\pi\, w(z)^2} e^{-2r^2/w(z)^2}, \tag{7.5}$$

where P is the total power of the beam, and r is the radial coordinate. The assumption for the cavity is that $R(0) \to \infty$ at the flat mirror, which then implies that the spherical mirror is centered at the other mirror, so that $R(L) = R$. Rearranging and solving for the new minimum beam waist gives:

$$w_0 = \sqrt{\frac{\lambda}{\pi}} (L(R-L))^{\frac{1}{4}}. \tag{7.6}$$

The parameters that determine the shape of the cavity are defined in Figure 7.3. Among them is the height of the SiC slab, h, which will be important later when simulating the mechanical modes. This equation immediately gives us the first constraint on the geometry for a stable optical resonance: $R > L$. We can then define our best estimate for the actual resonance conditions for the plano-convex geometry. We utilize an expression for the optical resonances in terms of the cavity length, radius of curvature, and the longitudinal mode number [136]:

$$f = \frac{c}{2L}\left(q + 1 + \frac{1}{\pi}\cos^{-1}\left(\sqrt{1 - \frac{L}{R}}\right)\right). \tag{7.7}$$

At this stage, we can choose R = 30 μm , L = 10 μm to estimate if we are indeed in the paraxial regime. The 44th longitudinal mode (q = 44) at this size has $f \approx$ 266 THz for its resonance, or $\lambda_{SiC} = \frac{c}{fn} \approx$ 0.442 μm for the index of refraction of SiC of n = 2.55. The beam waist using Eq. (7.6) would be $w_0 \approx$ 1.411 μm. This gives a ratio of $\frac{w_0}{\lambda_{SiC}} \approx 3$. Clearly, we close to the assumption of non-paraxiality ($\lambda \approx w_0$) when the light is focused on the flat mirror, but for larger R, this geometry trends towards the regime where we can assume the electric field is paraxial. This gives us confidence that our optical simulations in COMSOL will be physically relevant according to the paraxial approximation.

7.4.1 Distributed Bragg reflectors

This section introduces the structures that act as the mirrors for the Fabry-Perot cavity. We propose distributed Bragg reflectors (DBR) as the natural choice for adding reflecting layers with tunable reflectivities, as we want the flat edge mirror to be overcoupled and the dome mirror to have close to maximal reflectance at the two optical frequences relevant for the transduction scheme. The

basic structure of a DBR is alternating layers of two dielectric materials with refractive indices n_1 and n_2, where the relative magnitude of the indices and number of pair-layers can provide a customizable reflection spectrum over a wide range of wavelengths. The interaction between reflected and transmitted waves produces destructive interference at certain wavelengths of light, designated the stopband, incident on the DBR. The thickness, t, of each layer must be:

$$t_i = \frac{\lambda_c}{4n_i}. \tag{7.8}$$

To produce a cavity with resonance at λ_c where n_i is the index of refraction of each of the dielectric materials. Commercial design and fabrication of Bragg mirrors has led to very high reflectivities being achievable, as high as 99.98% for NIR wavelengths using oxide material stacks [137]. For this cavity design, it is not necessary to have such perfect confinement of the light, as the collection of the out-coupling photons is an important feature. DBRs are a good choice for this because the number of pairs of layers, N, can be different on one mirror to adjust the reflectivity and thus the average decay rate through that end of the cavity. The total measured optical losses do increase for each added pair, so there is an optimal number of layer pairs to use. The DBR structures investigated in the simulations will be composed of SiO_2 and Ta_2O_5 to produce band stop ranges for the necessary optical wavelengths for the optical cavities needed in the transduction device.

Introducing the DBR allows us to discuss the first major demarcation between the ideal cavities discussed in Section 7.4 and begin tackling the trade-offs necessary to simulate this system in a finite-element environment. Increasing the number of layer pairs in a DBR changes the effective cavity length, L, an optical mode interacts with due to the leakage of the mode into the first few layers of the DBR. This leakage is characterized by an exponential decay of the light field into the DBR.

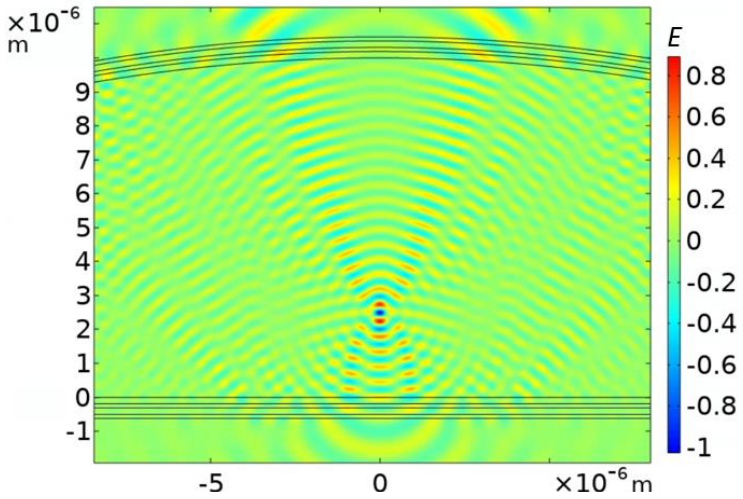

Figure 7.4. **Divacancy dipole field simulated in COMSOL.** Shown here is a close-up of the normalized electric field, *E*, for the divacancy dipole evaluated at a wavelength of 1100 nm used to calculate the modal overlap between the dipole and optical cavity fields.

This "penetration depth" can be estimated for a Fabry-Perot cavity with flat mirrors simply from the difference in the indexes of refraction [138] when the index difference is small. The problem of analytically defining the exact depth is more difficult. This same reference states no one penetration length can mimic every reflection property of a hard mirror, and three different lengths are needed [138]. For the device geometry at hand though, there are further difficulties defining the penetration depth when one of the mirrors is curved. Being able to arbitrarily define the effective *L* of the cavity is important because a simulation with an arbitrary *L* and *R* in the mph sweep experiment might not find an eigenmode of the TEM00 mode close to the divacancy frequency we are interested in analyzing. We apply a zeroth-order correction to *L* we will call L_{corr} that will be added to the parameter that COMSOL uses to seed the eigenmode search:

$$L_{COMSOL} = L + L_{corr} \, . \tag{7.9}$$

The rationale of this choice is that over moderate changes in the cavity geometry, the light field interacting with the DBR will be mostly similar, and thus will have a constant penetration depth associated with it.

7.4.2 Modeling divacancy dipole

The optical cavity simulations include information about the emitter that the light field mode interacts with. The divacancy defect in SiC will be modeled as an electric dipole positioned near the flat DBR stack, where the field is plotted in Figure 7.4. The magnitude of the dipole interaction strength with this resonant light field is necessary to calculate the emitter-field coupling strength, as discussed in Section 6.2.1. This value can be input into COMSOL to generate an electric field plot to simulate the spontaneous-emission of the divacancy at a certain wavelength. This enables us to estimate the modal overlap between the TEM00 optical mode of the plano-convex cavity and that of the dipole. The overlap magnitude can be thought of as reducing the coupling between the dipole and optical field due to photons emitted that are lost into the bulk of the SiC. The equation for the overlap, ϵ, is:

$$\epsilon = \frac{\int \left(E_{dipole} E_{cavity}\right)^2 dv}{\int \left(E_{dipole}\right)^2 dv \int \left(E_{cavity}\right)^2 dv}. \tag{7.10}$$

Here we take real components of the electric fields from both the dipole and the TEM00 cavity mode in the direction along the cavity axis. The integrals are simply taken over the entire cavity + DBR volume. We will use Γ_0 = 15 ns, DWF = 0.05, RE = 0.3, at 1100 nm to obtain 2.82×10^{-30} for the divacancy dipole magnitude in Eq. (6.11). [139,140]

7.4.3 COMSOL model of optical cavity

The 2D representation of the transduction device, including the plano-convex SiC cavity, surrounding air domains above and below the slab, and SiO2/Ta2O5 DBR mirror on the flat edge is shown in Figure 7.5 with the fundamental TEM00 mode simulated. PML domains of both SiC, DBR, and air make up the border domains to ensure the edge of the simulation domain does not

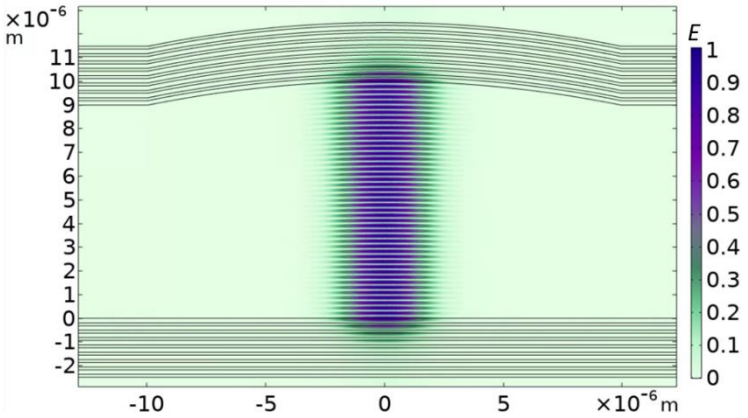

Figure 7.5. **Optical cavity eigenmode simulated in COMSOL.** Shown here is a close-up of the normalized electric field, *E*, (V/m) for the TEM00 Gaussian mode of the hybrid device with L = 10 μm, R = 50 μm, h = 9.25 μm. The wavelength is at 1100 nm. The Bragg layers have 8 layers on each face of the 4H-SiC, showing the leakage of the electric field leading to an effective increase in the cavity length we parameterize as $L_{eff} = L + L_{corr}$, by adding an additive length correction in the autonomous COMSOL simulation study for the emitter-cavity coupling detailed in Section 7.4.4.

act as a spurious reflecting boundary. Eigenmode scans will be the primary experiment done to investigate the quality of the optical modes that this design will produce over a range of geometric dimensions. A sweep over a range of cavity length, L, and radius of curvature of the dome, R, is done to produce values for the emitter-cavity coupling $g_{e,o}$ (Eq. (6.8)) of a dipole placed ~2.5 um above the flat cavity mirror. This coupling is found by calculating the mode volume (Eq. (6.9)) of the optical cavity along with other calculated constants. The mode shapes simulated will also produce values of the estimated modal overlap ϵ from Eq. (7.10) between the dipole and cavity field.

The optical and dipole cavity simulations were first fine-tuned for high-quality simulations individual cavity geometries on the edge cases of the dimensional ranges for L and R. Then the autonomous COMSOL simulation generation workflow described in Section B.1.2 was used to generate eigenmode simulations for 54 differently sized cavities to calculate the emitter-cavity coupling. This sub-section will describe the optical cavity simulations in detail and the next sub-section discusses the conclusions from the results.

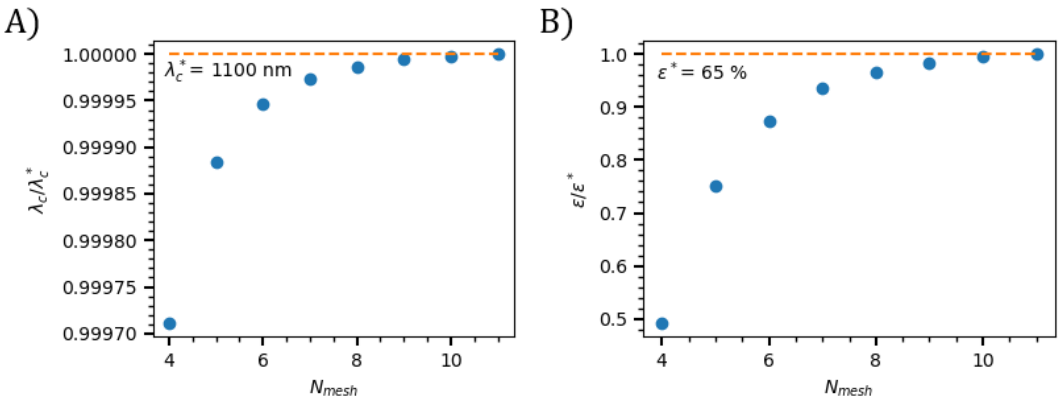

Figure 7.6. **Convergence of simulated optical and dipole field parameters. (A)** Plot of λ_c, the optical cavity TEM00 mode wavelength (Figure 7.5), vs. N_{mesh}. As the mesh density of the COMSOL optical mode simulation is increased (Eq. (7.11)), we should expect for a physically relevant estimation of the parameter a smooth convergence. **(B)** Plot of ϵ, the divacancy dipole field overlap (Eq. (7.10)) at 1130 nm (PL2 optical line), vs. N_{mesh}. For the MPh sweeps of the height and radius of the cavity geometry in Section 7.4.4, we use N_{mesh} = 8.

We describe the method to produce the optical cavity field in COMSOL. The Electromagnetic Waves, Frequency Domain interface of the Wave Optics module [135] was employed. This interface has an Eigenfrequency study type that solves the time-harmonic wave equation for the electric field to find the eigenmodes of resonant cavities. To reduce the overall complexity of the dimension scan, there is one major simplification. We represent the DBR layer on the curved surface as a perfect electric conductor boundary, as this will mimic the desired behavior of the final device having the curved mirror with high reflectance. A DBR of sufficient number of layers will approximate such a boundary condition. The PML boundary conditions ensure that energy is conserved globally. Given an initial seed frequency, COMSOL will attempt to find a prescribed number of eigenmode solutions near the seed frequency given the indexes of refraction of all domains and the boundary conditions supplied.

A critical part of the simulation is deciding the density of mesh elements in each domain. Too low of density can lead to non-physical volatility of cavity parameters due to spurious elements in the simulated electric field values at certain mesh elements. For these simulations, we

used a free triangular mesh everywhere the TEM00 mode had vanishing amplitude. In order to correct for what we designated spurious electric field features when using the free triangular mesh where there was non-zero amplitude, we used a square mesh of variable density, where the linear density for an edge was given by:

$$\frac{\frac{edge\ length}{\left(\frac{\lambda_0}{n_{domain}}\right)}}{N_{mesh}}, \tag{7.11}$$

where $\lambda_0 = 1100\,nm$, n_{domain} is the index of refraction of the domain, and N_{mesh} was a parameter chosen to represent the number of mesh elements per wavelength to be chosen. Upon calculating the TEM00 mode frequency and optical mode volume for few cavity dimensions, there was > 0.3% change in both values for N_{mesh} between 4 and 11, as shown in a convergence graphs in Figure 7.6. Thus, we chose $N_{mesh} = 6$ to represent the minimum mesh density that gave consistent values while minimizing the simulation times. This is on the rising edge of convergence, but due to the small percent errors in the wavelength we make this concession.

The dipole field in the simulation was made using the same Electromagnetic Waves, Frequency Domain interface with a frequency domain study that produced the corresponding electric field of a dipole placed at a certain position along the optical axis of the cavity. In order to obtain a high estimate of the emitter-cavity coupling, the dipole would be placed at a local maximum of the cavity eigenmode closest to 2.5 um above the flat DBR mirror. This position would give the greatest electric field density to increase the emitter-cavity coupling but would not be too close to the surface of the SiC to avoid disruption of its optical and spin properties [30]. Using $N_{mesh} = 6$ for a few values of the cavity dimensions showed a stabilizing value for the calculated field overlap (Figure 7.6) between dipole and cavity fields.

7.4.4 Simulated emitter-optical cavity coupling

Using the mph COMSOL interface, the optical cavity eigenmodes of the TEM00 gaussian mode as well as corresponding dipole mode were simulated with dimensions L = [5.0, 17.5] μm with 2.5 μm steps and R = [20.0, 100.0] μm with 10.0 μm steps. The dipole-cavity mode overlap was calculated to be 60-70% over the range of cavity dimensions studied showing high mode matching for this cavity design. The emitter-cavity coupling calculated using the divacancy dipole magnitude and the calculated optical mode volume, V_{mode}, from the electric field eigenmodes (Eq. (6.9)) gave a range of $\frac{g_{e,o}}{2\pi}$ that reduced by a factor of three between the smallest and largest cavity geometries considered as shown in Figure 7.7. This indicates a modest effect of the cavity dimensions on this coupling, giving more flexibility on the cavity design to improving the mechanical cavity performance, but minimizing the cavity dimensions will lead to larger emitter-cavity couplings and Purcell factor. We now calculate the emitter-cavity coupling (Eq. (6.8)) for the hybrid device dimensions deemed best regarding the mechanical cavity simulations (Section 7.5): L = 10 μm, R = 50 μm, h = 9.25 μm (mode shown in Figure 7.5). In a single eigenmode simulation involving both flat and circular DBR layers and a free-triangular mesh everywhere, we estimate $\frac{g_{e,o}}{2\pi} \approx$ 16.1 MHz. The meshing was made extremely dense, with the minimum size allowed to be $\frac{\lambda_0}{(n_{SiC}*24)}$.

With this coupling, we can estimate the Purcell enhancement for a divacancy defect situated inside the cavity at a spatial position to maximize the overlap and coupling. We assume dominant optical losses due to scattering from SiC root-mean-square (RMS) surface roughness

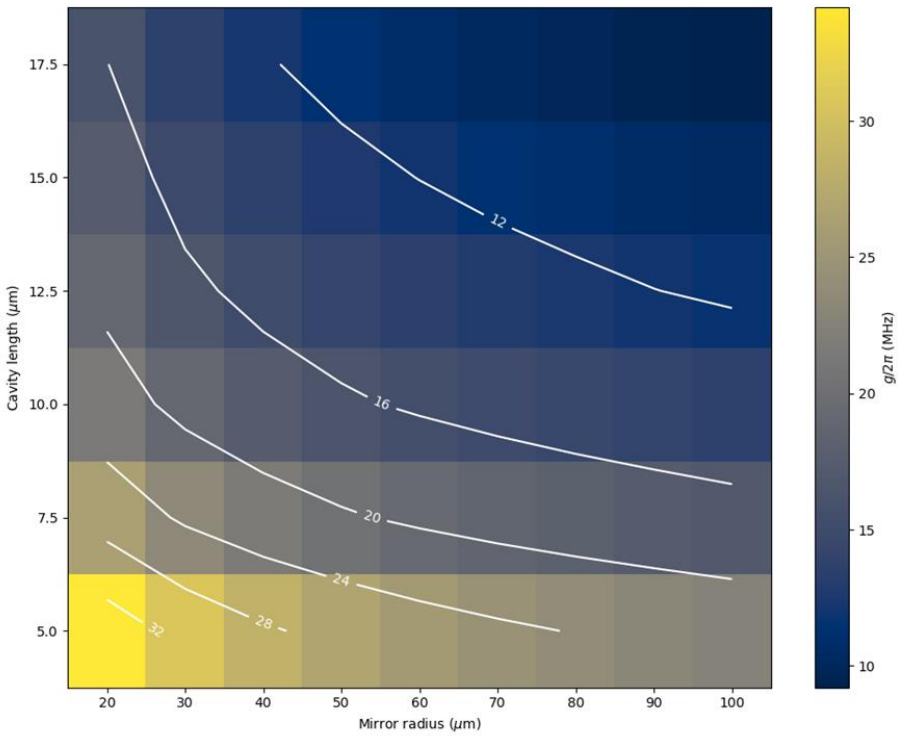

Figure 7.7. **Emitter-cavity coupling vs. cavity radius vs. cavity length MPh sweep.** Plot of $g_{e,o}$ vs. R vs. L for the MPh autonomous COMSOL simulation sweep. The divacancy dipole position was adjusted to be at the closest electric field maximum to ~2.5 μm above the flat mirror edge of the 4H-SiC to simulate the coupling to those divacancies situated far from any fabricated edges that could impact their optical and spin linewidths.

below 0.3 nm (see Section 6.3.3). The Purcell factor of emission enhancement from the divacancy gives us an estimate of F = 100 from Eq. (6.29) for this cavity geometry at 1100 nm with an optical quality factor, estimated from the surface roughness (Eq. (6.17)), Q_o~1×10^6 and simulated V_{mode} of ~2.41×10^{-17}. Using estimates from an investigation of the Purcell enhancement of the divacancy in nanobeam, it should be possible to achieve single-shot readout from the divacancy's spin-photon interface when collecting light from this optical cavity. In the configuration where there is now a mechanical cavity coupled in using OMIT, the ability to perform deterministic storage of an optical excitation in the mechanical mode and readout at telecom wavelengths will be aided by this increase in the divacancy ZPL emission. We can conclude that from the standpoint

of realistic optical cavity parameters, the proposed cavity design has an optimistic outlook as a transduction device.

7.5 Mechanical resonance modes

In this section, we will present the investigation of mechanical modes in the proposed monolithic plano-convex hybrid transduction device to determine the optimal geometric dimensions for having stable longitudinal mechanical modes with maximized optomechanical properties. We are interested in simulating longitudinal "breathing" modes where the cavity length, L, modulates as the top and bottom boundaries undergo displacement of opposite signs. This is in contrast to modes where L stays constant as the entire SiC slab undergoes motion, and we will not obtain an optomechanical backaction effect when driving the device with a laser tone. The nth longitudinal breathing mode will be described by the number the number of longitudinal anti-nodes plus one. The breathing modes then have odd n.

The wavelength of such a mode will be found from COMSOL eigenmode simulations. The practical frequency range for the mechanical oscillator resonance, Ω_m, is above the divacancy magnetic sub-level transitions (1-2 GHz) but higher frequencies decrease the optomechanical cooperativity, as will be discussed in Section 7.6. It turns out that Ω_m ~ 6-10 GHz might be within a bandgap for the DBR mirrors (Section 7.5.3).

In regards to the transverse direction, we are interested in longitudinal breathing modes that have maximum displacement in the center of the hemisphere and no transverse anti-nodes. We would want the waist of the mechanical mode to match that of the optical mode to ensure we have minimum mode volume for both simultaneously. We will thus restrict ourselves to longitudinal breathing modes with no transverse anti-nodes. Investigations of high-Q mechanical

modes in this plano-convex geometry in x-cut silicon show that mechanical mode waist, w_m, on the flat mirror to be [134]:

$$w_m{}^2 = \frac{\lambda L}{\chi\pi}\sqrt{\frac{g_1 g_2(1-g_1 g_2)}{(g_1+g_2-2g_1 g_2)^2}}. \tag{7.12}$$

Here λ is the phonon mode wavelength. The g_i are defined in the convention of plano-convex Fabry-Perot cavities as $g_1 = 1$ and $g_2 = 1 - \frac{1}{\chi R}$. Here, χ is an "anisotropy-constant" that encodes the effect the anisotropic point group symmetry of the 4H-SiC crystal lattice has on propagating acoustic beams with certain velocities. Its value of $\chi_{4H-SiC} = 1.96$ depends on the values of the fourth-rank compliance tensor for SiC expressed in Voigt notation as a 6x6 matrix with 12 non-zero elements [141] and the 4H-SiC density of ρ_{4H-SiC} = 3.216 kg/m^3. This allows us to define the range of stable mechanical cavities to be $R \geq \frac{L}{\chi_{SiC}}$ [134]. The stability criteria does not conflict with results from the optical cavity simulations, as it was determined $R \geq 3 * L$ was the preferred dimension relation (Section 7.4). The waist of the two modes will be within 10% for the range of cavity dimensions considered in Section 7.4.4.

7.5.1 COMSOL model of 3D mechanical cavity

The development of the 3D simulation of the mechanical oscillator in the monolithic hybrid device built in COMSOL will be described in this section. The 5th harmonic of the longitudinal breathing mode is shown in Figure 7.8. The relation between the cavity length, L, the radius of curvature of the dome, R, and the height of the 4H-SiC membrane, h, are defined similarly for the optical cavity and shown in Figure 7.3. The domains of this simulation are composed entirely of SiC with the main demarcations being a portion containing the hemispherical structure, a flat intermediate

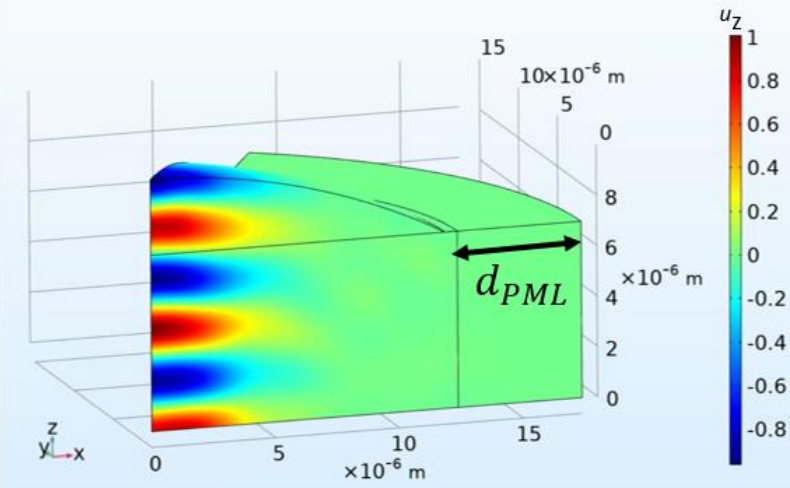

Figure 7.8. **Mechanical cavity eigenmode simulated in COMSOL.** Shown here is the normalized displacement field for the 5th harmonic of the longitudinal breathing mode with ω_c of 3.38 GHz. The hybrid device here has dimensions L = 10 μm, R = 25 μm, h = 7 μm. The z-axis is aligned with the 4H-SiC c-axis. The breathing mode has opposite signed z-displacements at the top and bottom of the cavity. In 7.5.2, the simulation dimension d_{PML}, representing the width of the PML region for the mechanical mode will be relevant when trying to identify mechanical loss mechanisms. Here, the PML domain width is d_{PML}= 4*$\lambda_c$$\mu$m.

region, and the remaining outside portion being a PML. Air domains are not needed in this simulation due to the vanishing coupling of phonon modes that propagate in the bulk of SiC into low density air found in our cryostat. A simplification we introduce is not including any mirror structures, allowing the top and bottom boundary conditions to act as them. In Sections 7.5.3-5, we will support the claim that we can consider calculating the mechanical cavity parameters without including the mechanically lossy DBR stacks by showing we can operate within a bandgap that has the DBR stacks act as highly-reflection mirrors for the phonon modes.

The intermediate flat region is necessary to add a buffer between the mechanical resonance mode tails interacting with the PML regions. Without this buffer, the mechanical mode waist will "clip" against the lip of the hemi-spherical region. This clipping of the mechanical mode is a main focus in understanding the quality factor of this cavity and trying to accurately describe mechanical loss sources in Section 7.5.2.

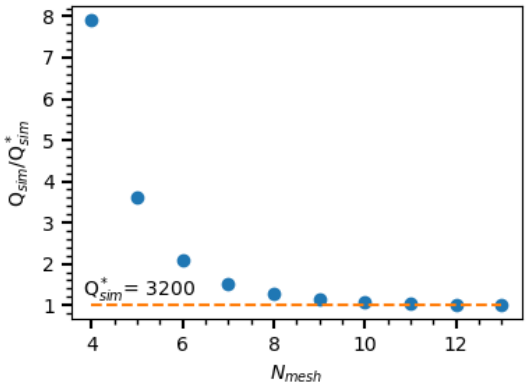

Figure 7.9. **Convergence of simulated mechanical quality factor.** Plot of $Q_{simulated}$ vs. N_{mesh} for the 5th harmonic of the longitudinal breathing mode (Figure 7.8) with cavity dimensions of with L = 10 μm, R = 50 μm, h = 9.25 μm showing smooth convergence as the meshing density is increased. For the MPh sweeps of the height and radius of the cavity geometry in Section 7.5.2, we use N_{mesh} = 9.

The anisotropy of the SiC point group symmetry demands we simulate the mechanical modes in 3D to capture the elastic response of the cavity in the most physically relevant way. This enters in the simulation by denoting the elasticity matrix, written in Voight notation [141] using the values of the fourth-rank compliance tensor of 4H-SiC already mentioned. This term represents the full behavior of the Young's modulus for 4H-SiC. Simulations in 3D are much more computationally demanding, but we exploit the six-fold hexagonal point group symmetry of 4H-SiC by simulating only a $\frac{\pi}{6}$ slice of the full plano-convex geometry, as shown in Figure 7.8.

Both the eigenmode and driven frequency studies of the mechanical modes are done using the Solid Mechanics interface of the Structural Mechanics module in COMSOL. The top and bottom surfaces are given the free boundary condition, as this represents the breathing mode motion we want to study. The outside edge of the PML is given a fixed boundary condition. The two sides are then given symmetry boundary conditions to impose the hexagonal symmetry without costing extra computation time.

The mesh density in the non-PML region is made free tetrahedral due to the wavelength of the phonons being a considerable fraction of the cavity size. The PML region is defined by a

mapped quadrilateral mesh to try and reduce the noticed spurious mode shapes seen frequently in the mechanical simulation PMLs. Section 7.5.2 addresses in more detail the spurious PML modes and how we reduced them. The meshing line densities are parameterized by a factor, N_{mesh}, in the equation:

$$\frac{edge\ length}{\left(\frac{v_l}{harm * f_0 * N_{mesh}}\right)}. \tag{7.13}$$

Here v_l is the phonon propagation speed in the direction along the axis of the cavity, defined from the elasticity matrix [141]. The variable $harm$ is an integer that denotes which harmonic of the longitudinal breathing mode a simulation is investigating and is equal to the number of anti-nodes plus one. Assignment of the meshing line densities can become trickier the smaller the boundary. It is imperative that for all dimension sweeps to prevent scalene faces of the tetrahedral meshing elements. Such perturbations from equilateral triangles are known to give less physically relevant results, and this meshing density accomplished that.

After a certain eigenmode of a harmonic of the fundamental longitudinal breathing mode has been identified, as in Figure 7.8, the quality factor, Q, for the mode and effective mass, m_{eff}, can be calculated from the simulation. The effective mass, m_{eff}, can be calculated as the integral over all the mass that is oscillating for a given vibrational mode [142]:

$$m_{eff} = \rho \int \left(\frac{u_z}{u_{z,max}}\right)^2 dz, \tag{7.14}$$

where u_z is z-axis displacement.

For the results of Sections 7.5.2, the focus was on the 5th harmonic due to it being the first with frequency above 2 GHz. Lower frequencies allowed more rapid iterations of simulation and analysis due to less mesh elements being needed. The stabilization of the calculated of these two variables with respect to the meshing parameterization, N_{mesh}, is the first method used to investigate the simulation quality. At this stage, the utilization of a PML allows to define a $Q_{simulation}$ that takes into account the amount of losses the eigenmode sees in the simulation. The equation used is:

$$Q_{simulation} = \frac{real(f)}{imag(f)}, \tag{7.15}$$

where $f = real(f) + i * imag(f)$ is the eigenfrequency of a harmonic of the fundamental longitudinal breathing mode. The trends in Figure 7.9 show N_{mesh} smoothly leading to convergence for $Q_{simulation}$. We present in the next two sections results that attempt to produce improvements to this the 3D simulation of the mechanical mode described in this section. These improvements will inform us how mechanical dampening is handled in the Structural Mechanics module in COMSOL and how we can be more confident the simulations give physically relevant information.

7.5.2 Mechanical mode density and clipping loss

The criteria for choosing the size of the transduction device from the standpoint of the estimated mechanical cavity mode density will be explored in this sub-section. The quality factor of the breathing mode should be made as high as possible to maximize the quantum cooperativity of the transduction device. We want to investigate the mechanical mode density near the mechanical modes of interest because if the radiation pressure force excites other modes, then the total

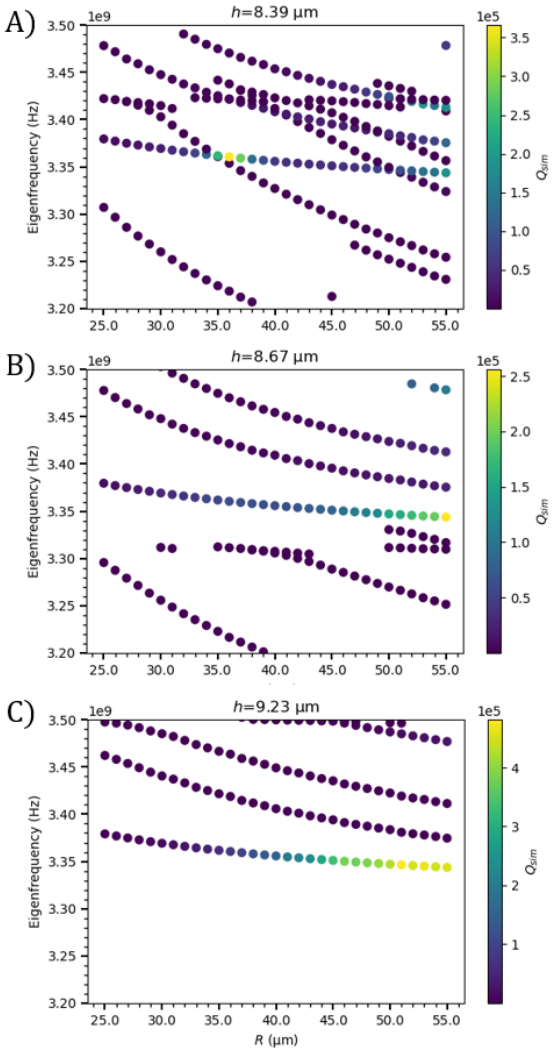

Figure 7.10. **Mechanical eigenmode density for various 4H-SiC bulk heights.** Plot of $Q_{sim.}$ vs. eigenfrequency vs. R for the MPh autonomous COMSOL simulation sweep of various bulk heights, h. Eigenfrequency range is in the vicinity of the 5th harmonic of the longitudinal breathing mode. The predominant bands that are seen for all heights are composed mostly of those for h=9.23 μm (C). Several additional bands seen for (A) and (B) disappear for larger h. The dispersion curve for all h with the highest $Q_{sim.}$ is the breathing mode shown in Figure 7.8. The minimum quality factor plotted on these graphs was 180.

optomechanical coupling could suffer. This could be measured in the form of reducing Q_m of the breathing mode of interest.

We investigate the effect the residual SiC height, h, has on the mechanical mode density sampled by a series of eigenmode studies COMSOL. In order to not preselect the orientation of modes, we return to an eigenfrequency study where we will use the MPh autonomous simulation workflow (Section B.1.2) to vary both R and h and calculate the $Q_{simulation}$ for all the eigenmodes found. R was varied between 25 and 55 um with 1 um steps and the h distribution was sampled with a small variation, where we choose 8 values between 8.25 and 9.25 um. Also, the size of the

PML domain will be set to four mechanical wavelengths unless otherwise state (). The cavity length will be kept constant. The eigenmode dispersion maps indicate that the smaller hemisphere supports less modes of moderate $Q_{simulation}$ in the vicinity of the fundamental mode, as indicated by the progression over three of the h values plotted in Figure 7.10. The highest $Q_{simulation}$ in all these sweeps occurs for the 5th harmonic of the longitudinal breathing mode for higher R values, with some indication of plateauing. All other modes have significantly lower $Q_{simulation}$. Another way to visualize this trend is by graphing only the breathing mode for each R vs. h (Figure 7.11), again keeping the cavity length, L, constant. Included in these graphs is an analytical estimate of the mechanical quality factor we call $Q_{clipping}$ and now define.

The trend in Figure 7.11 where the larger radii giving better mechanical quality factors can be partially explained by modeling the only energy losses present in the cavity as "clipping losses" from considering the mechanical cavity motion as a Gaussian beam passing back and forth through a circular aperture of radius D (defined in Figure 7.3), which in this case is the base of the hemisphere protruding out of the bulk of the 4H-SiC. We consider a Gaussian mode having power P_0 with an intensity I defined in Eq. (7.5). After traveling perpendicularly through a circular aperture of radius $D/2$, some of the power is "clipped off" and is considered lost to scattering. The remaining power in the beam, P_f, is given by [143]:

$$P_f = \int_0^{2\pi} \int_0^{D} I(r,z) r dr d\theta = P_0\left(1 - e^{(-2R^2/w^2)}\right). \tag{7.16}$$

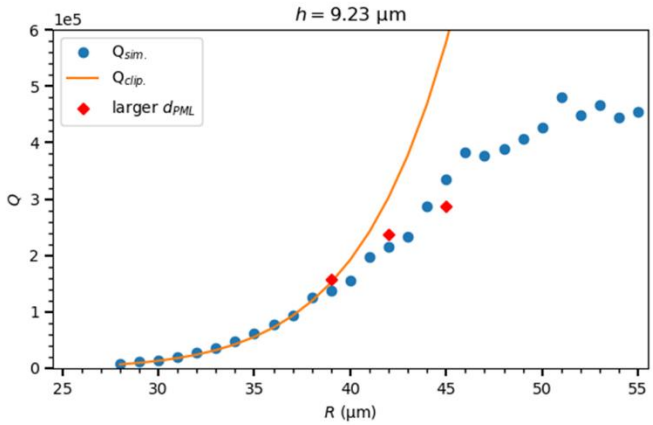

Figure 7.11. **Mechanical quality factor estimate comparison.** The matching of the mechanical quality factor estimated by the COMSOL simulation PML to the estimate from a clipping loss model in Eq.(7.17) for the mechanical mode in Figure 7.8. Red diamonds are points done with significantly more PML and incurred significant computation time. d_{PML}= 12*λ_c μm was used. Only a few points of this larger PML were included due to super-cubic simulation time-costs incurred when adding additional meshing elements for the 3D simulation.

This allows us to define a new estimate for the mechanical quality factor:

$$Q_{clipping} = \frac{P_f}{P_0}. \tag{7.17}$$

With this model for mechanical losses, we can explain the trends shown in Figure 7.11. Clipping loss follows the COMSOL quality factor estimates up to a certain R, before diverging from the clipping model. Also, after the divergence from clipping losses for h = 9.23 μm, $Q_{simulation}$ appears to slow its increase per radius. This suggests that another dominant source of mechanical loss takes over as the aperture becomes wide enough that clipping losses are a small effect and $Q_{clipping}$ begins to rapidly increase. We can look at the trend in Figure 7.10, showing lower h values for the cavities showing higher mode densities to try and explain the origin of the dominant source of mechanical losses for large R. These trends can be summarized as larger R and smaller h lead to more non-clipping losses. These trends both increase the volume of material enclosed in the dome structure, so we posit that the larger the volume of the dome, the more potential loss

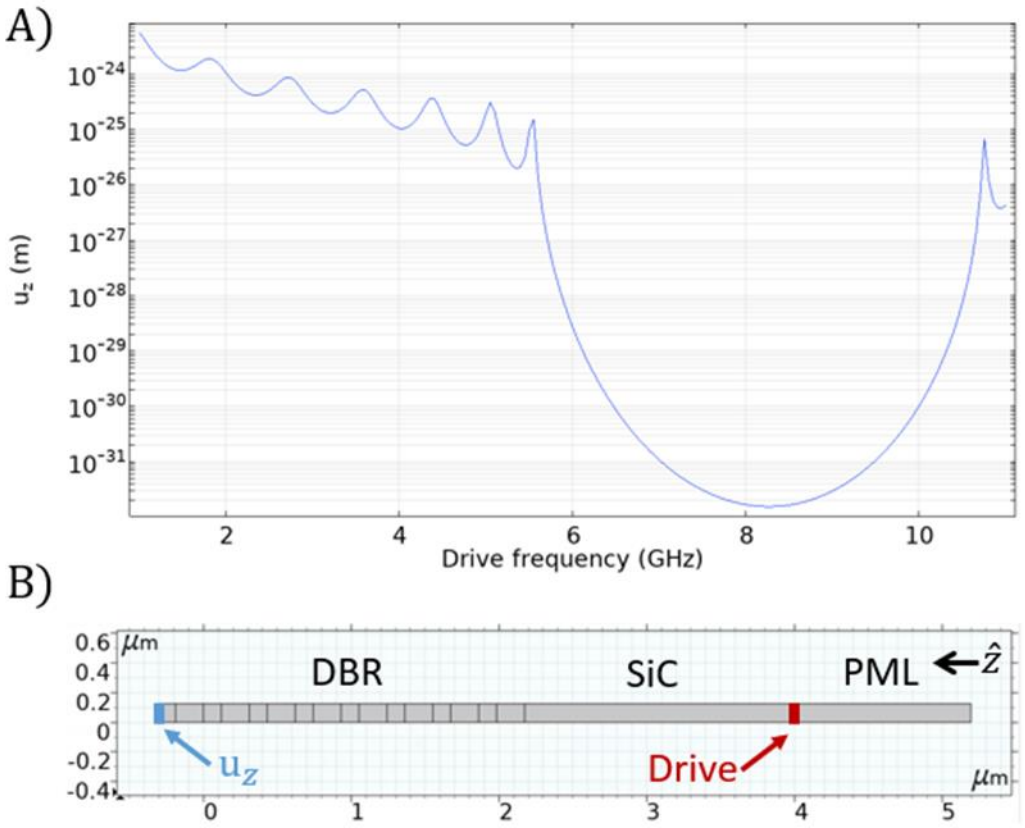

Figure 7.12. **Driven frequency bandgap response of 1D DBR mirror. (A)** Displacement u_z vs. driven frequency sweep of a 0.1 N force applied at location denoted in (B). The frequency of the applied drive on the left-most Ta_2O_5 edge is swept in COMSOL and reveals a more than 7 dB reduction in the lateral movement of the right SiO_2 edge showing that this DBR supercell acts to destructively interfere phonon modes between 5.5 and 10.5 GHz. **(B)** The COMSOL domains from right to left are: PML, SiC, and then 8 bilayers of SiO_2 (thicker layer) and Ta_2O_5.

channels exist for mechanical vibrations. Increasing the radius further appears to plateau the quality factor, so we can say that larger R and larger h lead to larger mechanical quality factors to use for estimating the maximum estimated optomechanical cooperativity for the hybrid device.

7.5.3 DBRs as mechanical mirrors

The 3D mechanical cavity simulation described in Section 7.5.1 has so far been simulated without including the DBR stack that is present in the optical simulations, and in this section, we will discuss the potential of utilizing the DBR as a phonon reflector in addition to a photon reflector. The number of interfaces and higher mechanical losses in the glass DBR stack threatens to sharply

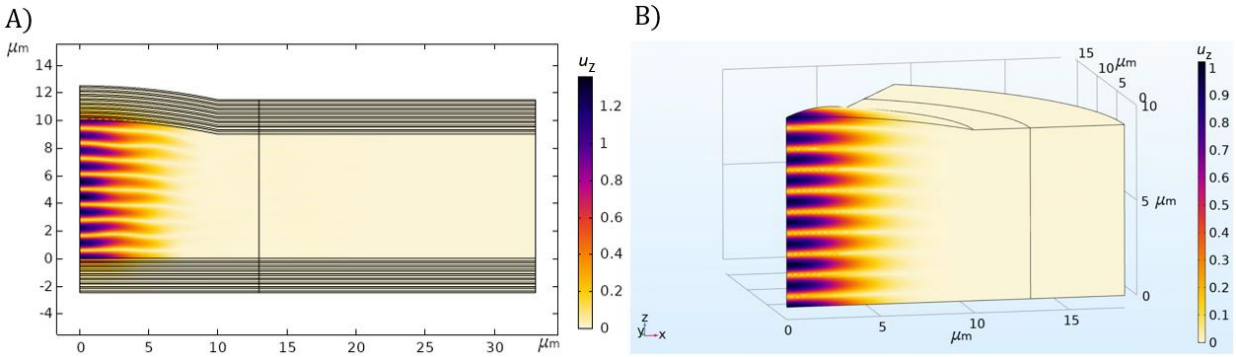

Figure 7.13. **Eigenmodes of 2D and 3D 9th harmonic of mechanical mode. (A)** Eigenmode of normalized displacement field, u_z, of 9th harmonic of longitudinal breathing mode at 6.12 GHz with 8 DBR bi-layers on top and bottom surface. Completing this eigenmode analysis with 2D axial symmetry allowed convergence of simulation compared to attempts to simulate DBR in 3D. See a vanishing penetration of the displacement field after ~1 bi-layer of the DBR, indicating deep phonon bandgap seen in a 1D model (Figure 7.12) can exist for plano-convex geometry. **(B)** Co-normalized mode of same mechanical mode at 5.98 GHz simulated without DBR stack in 3D with full anisotropy of 4H-SiC lattice. The cavity dimensions for (A) and (B) are L = 10 μm, R = 50 μm, h = 9.23 μm, the same as for the optical mode in Figure 7.5.

reduce the maximum mechanical quality factors our device could reach, as the mechanical mode volume will be much larger if it is not contained to the 4H-SiC cavity. We investigate the possibility of using a harmonic of the longitudinal breathing mode that treats the optical DBR as high-reflectivity mirrors as well. The identification of a mechanical stopband for the DBR layers at frequencies relevant for our mechanical device would compactify the transducer design and allow increased optomechanical coupling. Mechanical stopbands have been explored for acoustic devices in similar monolithic cavity geometries [144,145].

We perform a driven frequency study in a one dimensional supercell of eight alternating layers of SiO_2 and Ta_2O_5. When driving the left edge of the simulation with a force of 0.1 N at a range of frequencies relevant to the mechanical cavity, 1 to 11 GHz, we plot the displacement, u, of the other edge of the bi-layer cell as a function of the driving frequency. This driven frequency sweep reveals a drastic reduction in the boundary movement between 5.5 and 10 GHz (Figure 7.12), indicating that this DBR cell might act as a mirror in the 3D simulation, containing the displacement field to the 4H-SiC domain.

Unfortunately, adding the necessary DBR bi-layers (eight or more) utilized in the 2D axial symmetric optical cavity simulations lead to a drastic increase in the simulation convergence time for the 3D mechanical simulations. The total meshing elements needed to accurately compute the FEM of the phononic modes balloons by an order of magnitude. This is an unfortunate reality for high-frequency simulations in three dimensions, as there were similar super-cubic increases in simulation time when increasing PML domain size when simulating the mechanical quality factors in Figure 7.11. The end result is adding sufficient DBR layers to observe the bandgap in 3D to observe with the full anisotropic elasticity matrix causes COMSOL to not converge to a solution on the available hardware. We present in Figure 7.13 a realization of the bandgap in a 2D axial symmetric model of the mechanical eigenmode. This sacrifices the ability to model the anisotropy of SiC's crystal lattice and it simplifies down to using a single-valued Young's modulus. Nevertheless, the 9th harmonic of the longitudinal mechanical breathing mode shows a similar eigenfrequency compared to a full 3D simulation of the same mode. This indicates to us that our DBR design can indeed contain the mechanical displacements of interest and we can calculate the optomechanical cooperativity using the eigenmode of Figure 7.13B

7.5.4 Simulated optomechanical cavity coupling

From the results of the mechanical eigenmode studies completed in Section 7.5, we are now able to estimate the maximum optomechanical cooperativity using $g_{o,m} = Gx_{ZPF}$ (Eq. (6.40)). The final choice for the device dimensions will be L = 10 μm, R = 50 μm, h = 9.25 μm. The radius was made this size to maximize the mechanical quality factor to Q_m ~ 1e6, while not overly reducing the emitter-cavity coupling by increasing the optical mode volume. The height was chosen to reduce the mechanical mode density as smaller heights were seen to have more non-breathing modes of moderate quality factors. The optical mode simulated with these dimensions in Figure

7.5 gave a frequency shift per boundary displacement, G, of 26.19 GHz/nm (Eq. (6.34)). By integrating over the displacement field of the mechanical eigenmode at Ω_m = 5.977 GHz (Figure 7.8) gave an effective mass, m_{eff}, of 2.55 ng, which was used to calculate the mechanical ground-state zero point fluctuations, x_{ZPF} (Eq. (6.37)), to give a final estimated maximum value of the optomechanical coupling, $\frac{g_{o,m}}{2\pi} \approx 6$ *khz* for the hybrid device.

7.6 Conclusion

In this chapter, we used FEM simulation in COMSOL to estimate various cavity parameters to describe two of the three co-localized optical and mechanical modes necessary to induce NIR-to-telecom transduction in the proposed plano-convex geometry. The geometry proved to be able to satisfy the stability criteria and produce stable eigenmodes of photons at λ_c = 1100 nm and phonons of frequency Ω_m = 5.977 GHz in the cavity with at least eight bi-layers of a DBR composed of SiO_2 and Ta_2O_5 containing the modes inside the 4H-SiC where they can address a divacancy spin qubit ~2.5 μm off the flat mirror.

These simulations allow us to determine the feasibility of operating this structure under realistic loss conditions in a fabricated device. The main source of loss in the optical cavity comes from scattering losses due to non-uniformity of the 4H-SiC surfaces, characterized by their root-mean-square roughness. From our understanding of the photoresist reflow that could produce the minimum roughness for these dome structures [134], we believe σ_{RMS} ~ 0.35 nm is achievable for cavity dimensions studied in this thesis. Details on the material platform we considered best for fabricating the structures presented in this result are in Section B.2. The total optical cavity losses, characterized by its linewidth, κ, can be calculated using plot the range of realistic roughness, σ_{RMS}, vs. the overcoupling parameter of the optical cavity, η_c. Overcoupling ratio describes the

amount of power leaking out of the cavity vs. the amount reflected off the input-port mirror (see Section 6.3.4) and can be fully tuned by tuning the reflectivity of the DBR mirrors. If we make a graph of the cavity linewidth vs. roughness and overcoupling (Figure 3.1A), we can identify a region of overcoupling operation mode with a linewidth of κ ~ 0.4 GHz calculated with overcoupling of η_c = 70% and σ_{RMS} ~ 0.35 nm as a realistic target for the cavity operation (Section B.2).

For the goal of observing higher ZPL count rates from the divacancy defect coupled to the optical cavity, the Purcell factor gives us an estimate of $F \approx 170$ from Eq. (6.29) for this cavity geometry at 1100 nm with an optical quality factor, estimated from the surface roughness (Eq. (6.17)), Q_o~1×10^6 and simulated V_{mode} of ~2.41×10^{-17}. The represents a large increase in the counts from the divacancy that can assist in reaching the single-shot readout rate for photons carrying spin information. The deep placement of the divacancy due to the monolithic design, could enable obtain this Purcell enhancement without incurring a broadening of the divacancy optical linewidth to ~GHz values, above the ~200 MHz in non-fabricated 4H-SiC, in order to retain high spin-contrast of Rabi driving of divacancy spin qubits [47]. Implementing this ZPL emission enhancement would be a major step forwards for the divacancy as a quantum communication platform, and our simulation of the optical mode tells us it is feasible. The count rate will also assist the transduction scheme, explained below, to produce more on-demand photons to store as a mechanical resonance and possibly convert to telecom wavelengths.

In the regime κ ~ 0.4 GHz, estimated single phonon cooperativity (Eq. (6.44)) calculated using $Q_m = \frac{\Omega_m}{\Gamma_m} \sim 1\times10^6$ and $\frac{g_{o,m}}{2\pi} \approx 6\ khz$, is in the range $C_0 \approx 1\times10^{-5}$. This value is a respectable value compared to similar resonator designs. [99] For this realistic optical cavity linewidth, we

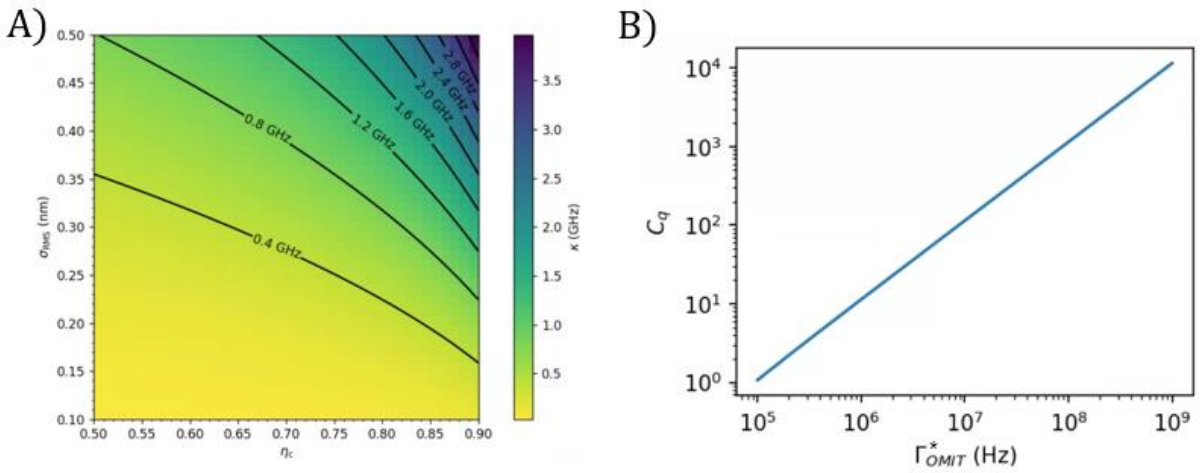

Figure 7.14. **Estimation of optomechanical performance for hybrid device. (A)** Plot of the optical cavity linewidth vs. RMS surface roughness on the 4H-SiC cavity vs. the overcoupling ratio. The realistic range of 0.35-0.30 nm for fabricated cavities corresponding to an overcoupling of 70%. **(B)** Plot of the quantum optomechanical cooperativity at 4.2 K phonon occupation in the mechanical mode vs. the bandwidth of the OMIT window imparted on the optical cavity linewidth, set by choosing a certain laser power addressing the optical cavity with a certain number of intracavity photons. For experimentally relevant bandwidths matching the optical lines of divacancies, ~100 MHz, $C_q \approx 1000$. This indicates the cavity can achieve thresholds for the proposed transduction scheme.

also should gain access to ground-state cooling of the mechanical resonator to being in the side-band resolved regime with a mechanical frequency of Ω_m = 5.977 GHz much larger than the optical cavity linewidth. We must also have quantum optomechanical cooperativity satisfying $C_q > 1$. This will depend on how many intracavity photons we can drive the cavity with before reaching the bistability regime for the optomechanical system (see Section 6.4.3). To assess this, we will plug in the maximum photon number allows by the bistability criteria (Eq. (6.46)) into the equation for the quantum optomechanical cooperativity (Eq. (6.45):

$$C_q = \frac{4{g_{o,m}}^2}{\kappa \Gamma_m n_{th}} \bar{n}_{cav,max} = \frac{4{g_{o,m}}^2}{\kappa \Gamma_m n_{th}} \left(6\sqrt{3}\frac{{g_{o,m}}^2}{\Omega_m \kappa}\right)^{-1}. \tag{7.18}$$

After canceling terms, and assuming 4.2 K operation in our cryostat, to obtain the average thermal phonon occupation of the cavity, n_{th} ~ 15 and using $Q_m = \frac{\Omega_m}{\Gamma_m} \sim 1{\times}10^6$, we obtain:

$$C_q \sim \frac{4Q_m}{6\sqrt{3} * 15} \sim 5{,}000. \tag{7.19}$$

Thus, we can say we have an optomechanical system operating at the sideband-resolved regime that can be cooled to its mechanical ground state, and the conditions to perform OMIT driving to store a divacancy photon as a mechanical excitation, as laid out in Figure 7.1. There is one more caveat, being that this driving at the maximum photon occupancy in the optical mode of $\bar{n}_{cav} \sim 1{\times}10^{10}$ would lead to rather broad OMIT bandwidth due to the effective mechanical damping being increased by $\frac{4{g_{o,m}}^2}{\kappa}\bar{n}_{cav} \sim 5$ GHz. Also, this is a relatively large cavity photon occupation that could lead to signification heat load in a realistic fabricated device with finite heat dissipation for the membrane through the employed cooling power of the cryostat. Both of these experimental limits mean we should consider a lower laser drive power for the optical cavity.

The discussion in Section 7.2 said that the OMIT bandwidth might vary depending on the exact species of divacancy studied in the cavity, between *kh* and *hh* configurations, where ~ GHz bandwidth would lead to lower transduction efficiencies or low spin readout contrast. If we set the OMIT bandwidth to be a desired value, Γ^*_{OMIT}, Eq. (6.52), we have:

$$\Gamma^*_{OMIT} = \Gamma_m + \frac{4{g_{o,m}}^2}{\kappa}\bar{n}_{cav}, \tag{7.20}$$

where $\Gamma_m = \frac{\Omega_m}{Q_m}$ and plugging this into the equation for the quantum cooperativity and canceling terms, we get:

$$C_q = \frac{(\Gamma^*_{OMIT} - \Gamma_m)}{\Gamma_m n_{th}}. \tag{7.21}$$

The graph in Figure 7.14B shows that the quantum optomechanical cooperativity dips down to around ~1000 for an OMIT bandwidth of ~ 100 MHz, which would be sufficient to match stabilized divacancy optical linewidths near 50 MHz [27]. Overall, these parameter estimations obtained from eigenmode simulations of electric and displacement fields in the plano-convex hybrid device show that it is feasible to reach the necessary thresholds to perform Purcell enhancement of the divacancy ZPL photons and storage of those photons as mechanical excitations via OMIT, paving the way for potential transduction to an optical cavity at telecom wavelengths with the proposed transduction readout scheme.

Appendix A

UNIVERSAL COHERENCE PROTECTION IN A SOLID-STATE SPIN QUBIT: DETAILS

A.1 Floquet Hamiltonian of dressed state levels

With the application of a dressing drive, the Hamiltonian under which we entered the RWA for the electron spin system of the divacancy is no longer valid. A different Hamiltonian describes the new energies for the dressed divacancy triplet manifold, with selection rules that restrict operation within a new 3-level system analogous to the manifold described in Section 3.2.3. Floquet theory allows us to invoke certain tools given that our divacancy groundstate Hamiltonian satisfies time evolution symmetry:

$$\widehat{H}(t) \;=\; \widehat{H}(t + t_o). \tag{A.1}$$

Floquet's theorem says the new quantum states will take on a form similar to our general solution for a TLS, but with a basis state where $|\psi(t)\rangle_n = |\psi(t + t_o)\rangle_n$ so we write:

$$|\psi(t)\rangle \;=\; \sum_{n=1}^{N} c_n \, |\psi(t)\rangle_n e^{-iEt}. \tag{A.2}$$

Then since we are interested in writing the Hamiltonian in a closed-form representation for all times, we utilize the result of reference [146] and substitute $\omega = 2\pi/T$ to begin to construct the Floquet Hamiltonian, $\widehat{\mathcal{H}}_F(t)$. The matrix decomposition has time-dependent components built from the Fourier components, $\widehat{H}_f(t)$, of the original Hamiltonian, $\widehat{H}(t)$, and we write first the first nine matrix elements denoted by their Floquet mode index, f:

$$\widehat{\mathcal{H}}_F(t) = \begin{pmatrix} \widehat{H}_0 + \omega f & \widehat{H}_1 & \widehat{H}_2 \\ \widehat{H}_{-1} & \widehat{H}_0 & \widehat{H}_1 \\ \widehat{H}_{-2} & \widehat{H}_{-1} & \widehat{H}_0 - \omega f \end{pmatrix}, \tag{A.3}$$

where the individual matrices are defined by:

$$\widehat{H}(t) = \sum_{f=1}^{N\to\infty} \widehat{H}_f(t)\, e^{-if\omega t}. \tag{A.4}$$

The H_n make up an infinite-dimensional matrix of the Hilbert space as N goes to infinity. The new Floquet Hamiltonian, $\widehat{\mathcal{H}}_F(t)$ can be written in closed form to find quasienergies of the system. We are able to pick diagonalizable elements of this matrix as branches of the dressed states produced by the Autler-Townes splitting of both of the *kh* divacancy states $|\pm\rangle$ we induced by turning on the dressing drive. We then will perform the RWA again (Section 2.4) to return to a closed-form expression for our divacancy Hamiltonian. Under a unitary transformation to diagonalize our base

divacancy Hamiltonian from Section 3.2.3, we start with the matrix components that allow us to construct the Floquet Hamiltonian:

$$H_0 = \begin{pmatrix} D+E & 0 & 0 \\ 0 & 0 & 0 \\ 0 & 0 & D-E \end{pmatrix}, H_{\pm 1} = \begin{pmatrix} 0 & 0 & \frac{\Omega}{2} \\ 0 & 0 & 0 \\ \frac{\Omega}{2} & 0 & 0 \end{pmatrix}. \quad \text{(A.5)}$$

The RWA is implemented by taking the lowest order regions of the infinite matrix space such that we get a diagonal matrix representation for the four dressed states. Extending the Floquet mode number to higher order would yield terms with higher multiples of the drive frequency, which we ignore under the approximation. Writing out the six elements denoted in Eq. (A.5) in the block matrix of Eq. (A.3), we identify the first 3x3 sub-matrix along the block matrix diagonal which we identify to correspond to the upper branch of states split from $|+\rangle$ by the Autler-Townes process at low magnetic field conditions:

$$\hat{H}_{F,RWA}^{u(pper)} = \begin{pmatrix} D-E+\frac{\omega}{2} & \frac{\Omega}{2} & 0 \\ \frac{\Omega}{2} & D+E-\frac{\omega}{2} & 0 \\ 0 & 0 & -\frac{\omega}{2} \end{pmatrix} + \frac{\omega}{2}\hat{1}. \quad \text{(A.6)}$$

Similarly, there is another matrix we identify as the lower branch of states split from $|-\rangle$ that we write as:

$$\widehat{H}_{F,RWA}^{l(ower)} = \begin{pmatrix} -\frac{\omega}{2} & 0 & 0 \\ 0 & D+E-\frac{\omega}{2} & \frac{\Omega}{2} \\ 0 & \frac{\Omega}{2} & D-E+\frac{\omega}{2} \end{pmatrix} + \frac{\omega}{2}\hat{1}. \tag{A.7}$$

Here $\hat{1}$ is the identity matrix. Here we make a critical assumption that the transverse ZFS will not change on the timescales of the experiments so we will always have the continuous microwave dressing drive on resonance. This means that $\omega = 2E$ at all times, and we obtain:

$$\begin{aligned} \widehat{H}_{F,RWA}^{u(pper)} &= \begin{pmatrix} D+E & \frac{\Omega}{2} & 0 \\ \frac{\Omega}{2} & D+E & 0 \\ 0 & 0 & 0 \end{pmatrix} \\ \widehat{H}_{F,RWA}^{l(ower)} &= \begin{pmatrix} 0 & 0 & 0 \\ 0 & D-E & \frac{\Omega}{2} \\ 0 & \frac{\Omega}{2} & D-E \end{pmatrix}. \end{aligned} \tag{A.8}$$

We note that the lower right of the upper branch and upper left of the lower branch elements (in this case simply the matrix element 0) are identically the center element of the entire block matrix of Eq. (A.3). That property will be shared in all the Floquet approximations we will make with the RWA when choosing sub-matrices. Now we make an assumption based on the primary direction of the lithographically patterned magnetic field drive in our experiment. The S_x dipole proportional to the field is responsible for driving spin into the $|+\rangle$ state in the non-dressed basis, and also now what is the pair of states whose evolution is controlled by $\widehat{H}_{F,RWA}^{u}$ above. The *kh* divacancy

selection rules are governed by linear polarization at zero magnetic field, so we can now say spin population prepared in $|0\rangle$ can only be driven into $|+\rangle$ character states at reasonable powers. This is due to the crystal alignment of the S_y dipole, which governs spin population transfer between $|0\rangle$ and $|-\rangle$, would take an unreasonable amount of power given the magnetic field alignment accessible by a drive wire parallel to the SiC surface would address non-S_y components leading to incoherent population transfer of TLS dynamics, where we avoid treatment of the full three-level-system dynamics that would result.

There is also a second assumption that further solidifies our treatment of the states $|\pm 1\rangle$ and $|0\rangle$, defined below, as a robust three-level quantum system that can be operated within the infinite allowable space due to the higher order Floquet modes. We take the weak driving case where $\Omega \ll E$ and here the states, $|f_n\rangle$, with unequal Floquet mode will not couple [147]. The expectation values for S_x between the undriven state and the lower branch vanish, while we retain non-zero components for the upper branch that allow us to perform qubit gate rotations in a chosen TLS of the basis $\{|0\rangle, |-1\rangle , |+1\rangle\}$.

Diagonalizing the upper branch term we can read off the energies for the two states of the Autler-Townes complex:

$$\widehat{H}_{F,RWA}^{u(pper)} = \begin{pmatrix} D + E + \frac{\Omega}{2} & 0 & 0 \\ 0 & D + E - \frac{\Omega}{2} & 0 \\ 0 & 0 & 0 \end{pmatrix}. \tag{A.9}$$

We see there is a Autler-Townes splitting of exactly half the drive amplitude, Ω. The top row is denoted by Floquet mode $f = +1$, while the middle row is $f = -1$. The bottom row, $f = 0$, is simply the undriven state with $m_s = 0$. The dressed states eigenvectors turn out to simply be linear

combinations of the *kh* divacancy states at zero magnetic field, and these will be the states investigated in Chapter 5

A.2 Dressed basis readout

This section describes a protocol for reading out the population of the dressed states, which contains a linear combination of the undressed states of the *kh* divacancy ground-state spin levels, so we can readout in a situation where the spin population information is only encoded in the states $|0\rangle$ and $|+\rangle$ as typically our 4H-SiC samples, including the one measured in this result, have optical linewidths around 200-300 MHz that makes this the only high-contrast readout basis [25].

We will take an arbitrary superposition in the dressed basis for the spin qubit defined by $|0\rangle$ and $|+1\rangle$:

$$|\psi\rangle = \alpha|0\rangle + \beta|+1\rangle. \tag{A.10}$$

If we now shut off the dressing drive on the scale of nanoseconds, we assume the system on average undergoes a non-adiabatic transition because the root mean square of the energy of the system does not change relative to the applied drive energy. We choose to ignore the probability of adiabatic dynamics, which is below 1%. This greatly simplifies the necessary treatment of the dynamics as the non-adiabatic conditions dictate a simple substitution of the undressed basis:

$$|\psi\rangle = \alpha|0\rangle + \frac{\beta}{\sqrt{2}}(|-\rangle + |+\rangle). \tag{A.11}$$

We want to remove the character of $|-\rangle$ specifically because the optical fine structure of the *kh* divacancy places the transition with $|-\rangle$ character only ~130 MHz away from the $|0\rangle$ character

transition while for $|+\rangle$ and $|0\rangle$ there is around 1 GHz of separation. This triples the signal to noise ratio for the readout contrast. So, after a $\frac{-\pi}{2}$ rotation about the z-axis of the Bloch sphere, we obtain:

$$|\psi\rangle = \alpha|0\rangle + \beta|+\rangle, \tag{A.12}$$

which contains the full information content of the dressed basis superposition but can be readout using the highest contrast readout procedure possible for this divacancy configuration with broadened optical lines from electrical and strain fields in the sample.

One additional complication involves superpositions in the $|\pm 1\rangle$ basis. Our procedure involves reading out only the PLE signal from one transition, with $|0\rangle$ spin character, but we would then have no contrast given we are mapping two states to that single observable. If we take the arbitrary state:

$$|\psi\rangle = \alpha|-1\rangle + \beta|+1\rangle, \tag{A.13}$$

and perform a π rotation to return to the situation of Eq. (A.10) above, and the coefficients can be measured due to optical contrast again. Thus, we can perform what we call the contrast recovery sequence to readout any arbitrary superposition in our three-level dressed basis.

A.3 Z-axis magnetic field fluctuations

In this section, we will write the dispersion curve that describes the dressed basis energy levels of $|\pm 1\rangle$ for z-axis perturbations of the magnetic field we simply write as B_z. We take the zero-field

Hamiltonian and add the Zeeman and microwave frequency drive terms from Section 3.2, setting $\gamma = 1$ for the Zeeman term for simplicity:

$$\widehat{H} = D\left({S_z}^2\right) + E\left({S_x}^2 - {S_y}^2\right) + B_z S_z + \Omega\cos(\omega t) S_z. \tag{A.14}$$

We apply a periodic, continuous drive with amplitude Ω to enter the dressed state picture, so we can proceed with the Floquet analysis procedure already utilized first in Section A.1. We will see how the energy levels change with the magnetic field perturbation. The diagonalized Fourier components of this Hamiltonian are:

$$H_0 = \begin{pmatrix} D+G & 0 & 0 \\ 0 & 0 & 0 \\ 0 & 0 & D-G \end{pmatrix}, H_{\pm 1} = \begin{pmatrix} -\frac{\Omega B_z}{2G} & 0 & -\frac{\Omega E}{2G} \\ 0 & 0 & 0 \\ -\frac{\Omega E}{2G} & 0 & -\frac{\Omega B_z}{2G} \end{pmatrix}. \tag{A.15}$$

The term G is defined as $G^2 = {B_z}^2 + E^2$ for compactness, as well as allowing a form where the diagonal elements of $H_{\pm 1}$ vanish if we assume the magnetic perturbations are small compared to the energy scale of the transverse ZFS. This is an assumption we can make due to the relatively large E of the *kh* divacancy system. We also again focus only on the upper Autler-Townes branch because it is the only branch we can experimentally access with our magnetic drive wire. We can write out and select from the Floquet block-matrix (Eq. (A.3)) a 3x3 diagonal matrix representing

the Hamiltonian of that upper branch due to the RWA constraining us to lowest order in the Floquet parameter:

$$\widehat{H}_{F,RWA}^{u(pper)} = \begin{pmatrix} D - G + \frac{\omega}{2} & -\frac{\Omega E}{2G} & 0 \\ -\frac{\Omega E}{2G} & D + G + \frac{\omega}{2} & 0 \\ 0 & 0 & -\frac{\omega}{2} \end{pmatrix} + \frac{\omega}{2}\hat{1}. \tag{A.16}$$

Here $\hat{1}$ is the identity matrix. The dispersion relation will be the difference in the energy eigenvalues of this matrix that correspond to the states of $|\pm 1\rangle$ inside the decoherence protected subspace. We assume that the dressing drive is exactly on resonance so $\omega = 2E$, and, after diagonalizing, the dispersion relation for z-axis magnetic field noise, $\Delta_z(B_z)$, is written as:

$$\Delta_z(B_z) = 2\sqrt{\left(\frac{\Omega E}{2G}\right)^2 + \left(G - \frac{\omega}{2}\right)^2}. \tag{A.17}$$

To obtain a tractable equation in the experimental parameters, we invoke the small perturbation assumption for B_z once more and write the Maclaurin series expansion in the ratio $\frac{B_z}{E}$ to write:

$$\Delta_z(B_z) \approx \Omega - \frac{\Omega}{2}\left(\frac{B_z}{E}\right)^2 + \left(\frac{3\Omega}{8} + \frac{E^2}{2\Omega}\right)\left(\frac{B_z}{E}\right)^4. \tag{A.18}$$

The approximation suppresses terms of order of our small parameter raised to the sixth power, which are not relevant to the energy scales we have access to given the magnitude of the transverse ZFS.

A.4 X-axis magnetic fluctuations

In this section we consider small perturbations of the dispersion relation for the dressed energy levels $|\pm 1\rangle$ for x-direction magnetic field perturbations, B_x, and write the Hamiltonian again with the modified Zeeman term as in Section A.3:

$$\widehat{H} = D\left(S_z{}^2\right) + E\left(S_x{}^2 - S_y{}^2\right) + B_x S_x + \Omega \cos(\omega t) S_z. \tag{A.19}$$

A critical property of this Hamiltonian is that it is rotationally invariant along the z-axis. Therefore, the B_y fluctuation Hamiltonian would simply become equivalent to B_x fluctuation, after a change of basis equal to a 90 degree rotation where $S_x \to S_y$ and $S_y \to -S_x$:

$$\widehat{H} = D\left(S_z{}^2\right) + E\left(S_x{}^2 - S_y{}^2\right) - B_y S_y + \Omega \cos(\omega t) S_z. \tag{A.20}$$

We can absorb the sign of the perturbation and have the same Hamiltonian. This allows us to use the dispersion relation under perturbation B_x as the dispersion relation for any perturbation applied orthogonal to the z-axis.

We proceed again through the Floquet analysis procedure of the previous section. The lowest order diagonalized Fourier components of this Hamiltonian is:

$$H_0 = \begin{pmatrix} \frac{F+J}{2} & 0 & 0 \\ 0 & \frac{F-J}{2} & 0 \\ 0 & 0 & F-2E \end{pmatrix}, \tag{A.21}$$

and the higher order Floquet term is:

$$H_{\pm 1} = \begin{pmatrix} 0 & 0 & \frac{-\Omega B_x}{\sqrt{4{B_x}^2 - (F-J)^2}} \\ 0 & 0 & \frac{-\Omega B_x}{\sqrt{4{B_x}^2 + (F+J)^2}} \\ \frac{-\Omega B_x}{\sqrt{4{B_x}^2 - (F-J)^2}} & \frac{-\Omega B_x}{\sqrt{4{B_x}^2 + (F+J)^2}} & 0 \end{pmatrix} \quad \text{(A.22)}$$

This time the simplifying constants are $F = D + E$ and $J^2 = {B_x}^2 + 2F^2$. Again, we set to zero $H_{\pm 1}$ elements containing $F + J$ because for small perturbations we have $B_x \ll F + J$. Writing out the block matrix and invoking the RWA to consider the first diagonal matrix with Floquet mode below 1, we write out the Hamiltonian for the dynamics of the upper branch:

$$\widehat{H}_{F,RWA}^{u(pper)} = \begin{pmatrix} F - \frac{\omega}{2} & \frac{-\Omega B_x}{\sqrt{4{B_x}^2 - (F-J)^2}} & 0 \\ \frac{-\Omega B_x}{\sqrt{4{B_x}^2 - (F-J)^2}} & \frac{F+J}{2} & 0 \\ 0 & 0 & \frac{F-J}{2} - E \end{pmatrix} + \frac{\omega}{2}\hat{1} \quad \text{(A.23)}$$

The dispersion relation describing the energy difference, Δ_x, of the $|\pm 1\rangle$ states when driven on resonance ($\omega = 2E$) in the decoherence protected subspace after solving the eigenvalue equation is:

$$\Delta_x(B_x) = 2\sqrt{\left(\frac{F-J}{16}\right)^2 + \left(\frac{\Omega^2 {B_x}^2}{4{B_x}^2 - (F-J)}\right)^2} \tag{A.24}$$

We perform a similar Maclaurin series expansion as the previous section in the small ratio $\frac{B_x}{F}$ to write, with terms of the small ratio to the sixth power or higher suppressed:

$$\Delta_x(B_x) \approx \Omega - \frac{\Omega}{2}\left(\frac{B_x}{F}\right)^2 + \frac{1}{2}\left(\frac{11\Omega}{4} + \frac{F^2}{\Omega}\right)\left(\frac{B_x}{F}\right)^4 \tag{A.25}$$

A.5 Electrical and thermal fluctuations

In this section we will revisit our derivation of the energy levels produced by Autler-Townes splitting (with no magnetic noise terms) from the dressing drive, where we cannot simply say $\omega = 2E$, as we did in Section A.1. This will give us insight into how electrical noise effects the dressed

state energy levels, which encodes electrical and temperature fluctuations as they enter into the Hamiltonian as the longitudinal and transverse ZFSs. For the upper branch, we write:

$$\widehat{H}^{u}_{F,RWA} = \begin{pmatrix} D - E + \frac{\omega}{2} & \frac{\Omega}{2} & 0 \\ \frac{\Omega}{2} & D + E - \frac{\omega}{2} & 0 \\ 0 & 0 & -\frac{\omega}{2} \end{pmatrix} + \frac{\omega}{2}\hat{1} \tag{A.26}$$

Keeping the drive frequency here and introducing the dressing drive detuning, $\delta_\omega = E - \frac{\omega}{2}$, we simply diagonalize the matrix to find the energy splitting between $|\pm 1\rangle$ to be:

$$\Delta_\omega = 2\sqrt{\left(\frac{\Omega}{2}\right)^2 + {\delta_\omega}^2} \tag{A.27}$$

This shows that D will not couple into this energy difference, Δ_ω, but the first-order sensitivity to electric field noise that the undressed basis experiences will manifest in E fluctuations [25].

Appendix B

DESIGN OF A MONOLITHIC HYBRID OPTOMECHANICAL RESONATOR COUPLED TO A SPIN QUBIT: DETAILS

B.1 Finite element modeling

In this section, we will discuss the operation of the modeling software used to simulate the proposed cavity device. The analytical solutions of the optical and mechanical modes inside an arbitrary cavity structure are unwieldy due to the boundary conditions imposed by the SiC plano-convex shape and DBR layers that contain the fields. For planar Fabry-Perot cavities, with two flat mirrors composing the boundaries, there are techniques for analytical modeling of the behavior of the cavity as a 1D system, such as the transfer matrix model. There are a two reasons why we do not want to restrict the analysis to one dimension. The first is we want to have a cavity that is well mode matched to the gaussian beam of our laser excitation that will address a single divacancy, so capturing the behavior of the modes in 2D (when axial symmetry can be assumed) or 3D is important. The second reason is that we want to investigate the range of dimensions the cavity can be fabricated in given the proposed SICOI platform, which mainly is determined by utilizing 20 micron thick epitaxial layers of i-type SiC, that must be polished down to thicknesses around ~15 microns. Observe the mode shapes of optical and mechanical resonances under changing

geometric parameters is far more insightful when not restricted to 1D calculations along the primary axis of the cavities.

B.1.1 Overview of simulation components

We will be using COMSOL Multiphysics that uses the finite element method (FEM) to solve for the cavity modes, represented by either electric fields or displacement fields, given a number of initial conditions provided by the user. These conditions include primarily assigning domains to have sizes and material properties to represent the parts of the real system. The properties assigned are those relevant to the physical equations being solved when using the FEM. For example, there will be domains of air and SiC that have their respective indexes of refraction during optical mode studies. The extent to which the simulations can be assumed to give physically relevant data can be difficult to determine during initial attempts at capturing the behavior of a system. Many successive simulations with tweaks to the initial conditions are usually needed to build an understanding of how the simulation behaves. Successive alteration of the initial conditions and analyzing the results allows building inferences towards the behavior of an actual optomechanical device.

The FEM is a method of solving partial differential equations that represent physical relations by finding approximations within a chosen discretization. The approximation is one that can be solved numerically within a small subset of the total spatial or temporal domain of the problem. The power of the method comes from the flexibility of the choice of discretization, where the simplest example is to have more approximations done in regions where the variables are

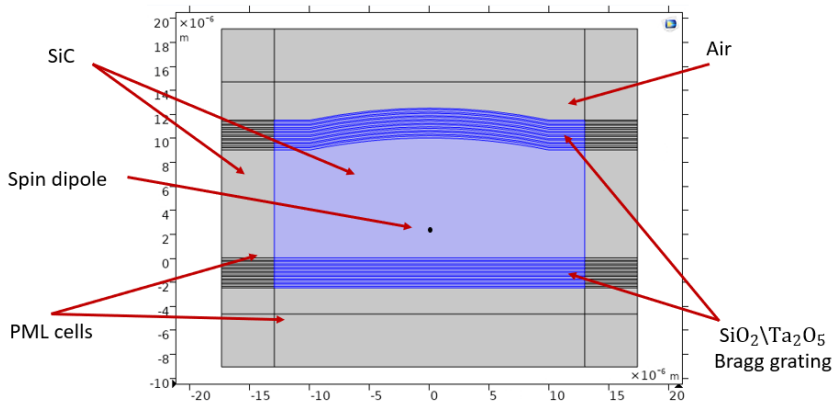

Figure B.1. **Major components of COMSOL simulation.** Representation of hybrid device structure as rendered in COMSOL showing SiC domains in the middle, enclosed by DBR domains, and then the remaining are air domains. The outside domains are labeled as perfectly matched layer (PML) domains for the three listed material domains. The PML simulates the material of their domain stretching to infinity to save computational resources when avoiding hard walls in the resonant structure simulations.

changing more rapidly. The discretization over an area is usually called the mesh. For cavities, the fields will be fluctuating at the resonance frequency, so we will restrict ourselves to analyzing the steady state solution with a chose spatial discretization. A rule of thumb for COMSOL is that five cells per wavelength is the minimum density to use. Increasing this density is usually necessary, and the parameter vs. mesh density should be checked to observe asymptotic behavior with increasing density. Discrete jumps or oscillations in a convergence graph usually indicates non-physical results due to poorly chosen meshing density.

The guiding principles when doing any FEM simulations is to be mindful of the tradeoff between the complexity of the model and the time a simulation produces a result. A 2D slice of an optical dipole's electric field can take less than a minute, but a full 3D render of an SiC slab's response to mechanical driving can take tens of hours, or even fail to converge. One could say the insight gained per unit time must be maximized. Complex simulations give more information but in return take longer to complete, so concessions on both the numerator and denominator of this ratio must be made.

A typical simulation is built off of designating domains as different materials that make up the real geometry of the device. The material domains of the hybrid device are shown in Figure B.1. It consists of a silicon carbide membrane with the hemispherical structure atop it, created by an etching process. Air boundaries encapsulate it to give the Gaussian optical mode space to travel towards the cavity from infinity, which is represented by a pseudo-infinite boundary condition defined in the next paragraph. The cavity resonant condition is created by using layers of glassy oxides that make up a distributed Bragg reflector mirror at chosen optical frequencies (Section 7.4.1). For the mechanical simulations, air and DBR domains are not employed because we chose to work with a simulation where the vibrational modes do not extend very far outside of the silicon carbide due to a proposed usage of the optical DBR mirrors simultaneously as mechanical mirrors (Section 7.5.3).

Perhaps the most important component of a COMSOL simulation is the definition of the external boundary conditions that connect the system under study to the rest of the environment. This concept is similar to that from introductory thermodynamics, where a system's thermal response is considered when in contact with a large reservoir of constant temperature. The internal dynamics of such a system is drastically different when not connected to the reservoir. In our case, we want to be simulating cavity excitations where the edges of our simulation in software act as if that edge is at infinity in real space, where the field amplitude dissipates to zero. Incorrect boundaries can lead to spurious reflections off those edges, leading to erroneous calculations of the loss channels and corresponding quality factors of the cavities. In COMSOL, this infinite boundary is implemented in what are called perfectly matched layers (PMLs). PMLs are used to designate a domain as an open and nonreflecting boundary of infinite extent. To obtain physically

relevant results, correct meshing is important when transitioning away from a region near the modes of interest to the outskirts of the domain where the PML cells are. There should be no eigenmode solutions that show non-dissipating structure inside a correctly implemented PML layer.

The two major methods used to characterize steady-state cavity modes using FEM are eigenmode simulations and frequency domain simulations. The goal of an eigenmode simulation, or study, in the COMSOL terminology, is to solve a matrix equation representing the given initial conditions and boundary conditions for the chosen fields (electric fields for optical modes for example). The major user input choice here is given the COMSOL solver an initial guess of the frequency of the resonance that is trying to be modeled. For example, an initial guess for the optical cavity TEM00 gaussian mode could assume a linear Fabry-Perot cavity of the same length. The eigenmode study would then proceed to find steady-state solutions matching that frequency, but there is no guarantee that the mode of interest will be found due to the number of other, low-quality-factor modes that the geometry can support. The density of states can be combed through finer by telling the study to find tens or hundreds of eigenmode solutions. Sifting through all these can be a tall order, and the next subsection describes a way to autonomously handle some of the tedious work. The frequency domain simulation can be considered the inverse of the eigenmode simulation in some ways. Here a range of frequencies the user wishes to see steady-state solutions for are given, but instead of seeing all possible resonances the geometry can support, the initial conditions require some forcing function, and the resonance modes that result from that force are evaluated in the given frequency range. This is an important tool to focus on a particular mode shape given the force can be defined. For example, the radiation pressure force from a Gaussian light-field acting on a mechanical cavity could be investigated at various frequencies. This can

allow gaining insight on other modes besides the longitudinal standing waves along the primary cavity axis could be excited from the force and have a reasonable quality factor. We will utilize both eigenmode or driven frequency studies in our investigation of the hybrid device.

B.1.2 Autonomous simulation analysis

Once a cavity simulation has been initialized and defined in the COMSOL software GUI, there are many possible ways to analyze the resulting field solutions, either in the GUI or after exporting the raw data. This process can become tedious for a study involving tracking the changes of certain properties of the mode shapes given changes in the cavity geometry simulated. COMSOL does have several functional ways to handle changes in initial conditions and compute the simulations for all values considered. These functions were not applicable to all the parameter sweeps we wished to complete for the hybrid device, so another solution was found. A workflow was developed to autonomize the entire process of building a COMSOL model in an executable instance of the program and then exporting the results of a COMSOL study to a python data stream for saving the findings of analysis code. A python library called MPh [148] allows interfacing the Java source code that COMSOL is built from with the Python language is utilized in a scheme to perform autonomous simulation analysis. This technique also allowed parallelized launching of several simulations that resulted in much faster overall simulation hours when carefully allocating computing resources to not overwhelm the simulation computer.

Each instance of a COMSOL simulation launched as a separate instance from a python command line consumed a certain average amount of computer RAM and CPU operating percentage. Launching a different amount of instances all solving the same simulation until convergence was found allowed optimization of our simulation computer's parallel solving bandwidth. This varied depending on the average number of cells an implementation of the

autonomous solver used. The mechanical simulations in 3D demanded about two to three orders of magnitude more cells than the 2D axial symmetric optical mode simulations, millions vs. several thousand cells. Thus, deciding the allocation of computing resources each time an autonomous simulation experiment was performed took several iterations fine-tuning using small batches of the parameters that ultimately would be swept. Starting a large batch of parameters, which could take several days to complete, with unoptimized allocation would result in wasted computation time from unconverging COMSOL simulations due to computing resource starvation or under-resolved simulation parameters in the analysis step from not sweeping the parameters at fine enough resolution.

B.2 Proposed fabrication methods for monolithic 4H-SiC cavity

The proposed material platform for the hybrid device that informed decisions for the simulations of the optical and mechanical modes consists of three major fabrication processes with 4H-SiC. Implementation of these fabrication steps to create a real device would take a significant time investment, but the goal was to consider processes that have been previously developed and used to make other devices already. This section serves as an example of the most straightforward and feasible collection of processes that could be utilized but makes no claims that these processes solve every potential problem that one could encounter when fabricating a real device.

B.2.1 4H-SiC-on-insulator polished membranes

We begin with a 4H-SiC chip that has an epi-layer containing the desired density of divacancies after electron irradiation and annealing of thickness at or more than 20 microns. There is a technique where the epi-layer can be bonded to a different material as a substrate, which will allow undercutting of the 4H-SiC slab to create a free-standing membrane. The final product is called

SiC-on-insulator (or SiCOI) [149] where it is bonded to silicon and then ground down to approximately 10-17.5 μm using a polishing technique that yields surface roughness much lower than will result from creation of the hemispherical structure.

Presented here is an overview of the SiCOI creation process. The 4H-SiC chip, which is composed of the thin epi-layer and few hundred micron high-impurity bulk, is first bonded to a silicon chip of larger surface area using Hydrogen silsesquioxane (HSQ), an inorganic compound often used in photolithography processes. After coating with 200-300 nm of HSQ, a strong bond to a 500 μm thick Si wafer is formed by thermal annealing. The 4H-SiC slab is then ground mechanically to remove the high-impurity bulk, revealing the underside of the epi-layer. Chemical and mechanical polishing followed by a reactive-ion etching process results in a roughness of the flat, exposed 4H-SiC surface to approximately 2-3 Å.

This process results in three very important features for the hybrid device. 1) Bonding the thin epi-layer to a silicon chip will allow undercutting the silicon using etching processes that do not remove 4H-SiC, which would increase the error in the cavity length, which is set by the membrane thickness. 2) That membrane thickness can be carefully controlled by varying the steps in the polishing process. 3) This process yields a roughness on both the top and bottom 4H-SiC surfaces on order of 2-3 Å, which gives us the best starting point to yield low surface roughness on the hemispherical surface described below.

B.2.2 Photoresist reflow etched hemispheres

Now we will outline the steps and advantageous of a fabrication process for creating the hemispherical structures that will form the cavities that support optical and mechanical Gaussian modes. A photoresist reflow process can be used that exploits surface tensions to coax photoresist layers to form structures described by circular arcs on top of the 4H-SiC surface where that shape

can be transferred during etching to remove exactly the 4H-SiC material to reveal hemispherical structures of precise radius of curvature and remaining bulk height of the 4H-SiC membrane [134].

Here we outline the reflow procedure. The final roughness of non-flat surfaces can be heavily impacted by surface contaminants, so the 4H-SiC sample is cleaned using a three-step organic sonication procedure, then ablated in oxygen plasma, and then finally baked at high temperatures. Disks of photoresist of precisely calibrated diameters are created on the surface using a lithographic photomask. The 4H-SiC surface and disks are primed with an organosilicon compound, hexamethyldisilazane (HMDS), to increase the retention of the disc's height and radius as defined by the photomask. Next the sample is inverted, and the disks are exposed to heated propylene glycol monomethyl ether acetate (PGMEA) vapor so that the initially solid photoresist disks will soften to allow the forces of surface tension to shape them, allowing the edges to slope and create hemispheres. The now hemispherical photoresist structures are baked until only trace PGMEA concentrations remain to re-solidify the photoresist. The shape of the photoresist structures is then transferred to the 4H-SiC membrane using a reactive-ion etching process. Through trials utilizing the above techniques performed to create the devices in [134] on our own chips of SiCOI containing divacancies, we saw surface roughness on order of 3 Å.

This process results also results in three very important features for the hybrid device. 1) This technique is compatible with the silicon substrate the 4H-SiC is chemically bonded to in the SiCOI creation step. 2) Through careful optimization of all the reflow parameters, the radius of curvature and height of the remaining SiC membrane can be precisely controlled to create hemispherical structures that match our best estimation of what cavity dimensions will have the best quality factors, as well as other performance factors outlined in Chapter 7. 3) This technique produced low surface roughness on the non-flat structures, a very difficult goal in fabrication of

semiconductors like 4H-SiC. We identified the surface roughness to be one of the most important factors to enable the cavity to reach high Purcell factors and operation of its optomechanical cavity at its mechanical groundstate to enable the proposed transduction scheme. After removal of the silicon layer at a precise location in the center of the 4H-SiC chip corresponding to the location of the hemispherical structures, the optical and mechanical performance of the hybrid spin-opto-mechanical device can be explored to see if our estimations of the feasible thresholds for these applications involving the divacancy in 4H-SiC can be realized.

Bibliography

[1] M.A. Nielsen, I.L. Chuang, Quantum Computation and Quantum Information: 10th Anniversary Edition, Quantum Computation and Quantum Information (2010). https://doi.org/10.1017/CBO9780511976667.

[2] L. Bassman, M. Urbanek, M. Metcalf, J. Carter, A.F. Kemper, W.A. De Jong, Simulating quantum materials with digital quantum computers, Quantum Sci Technol 6 (2021) 043002. https://doi.org/10.1088/2058-9565/AC1CA6.

[3] F.F. Flöther, The state of quantum computing applications in health and medicine, Research Directions: Quantum Technologies 1 (2023) e10. https://doi.org/10.1017/QUT.2023.4.

[4] N. Sharma, R. Ketti Ramachandran, The Emerging Trends of Quantum Computing Towards Data Security and Key Management, Archives of Computational Methods in Engineering 28 (2021) 5021–5034. https://doi.org/10.1007/S11831-021-09578-7/TABLES/3.

[5] M. Allende, D.L. León, S. Cerón, A. Pareja, E. Pacheco, A. Leal, M. Da Silva, A. Pardo, D. Jones, D.J. Worrall, B. Merriman, J. Gilmore, N. Kitchener, S.E. Venegas-Andraca, Quantum-resistance in blockchain networks, Scientific Reports 2023 13:1 13 (2023) 1–23. https://doi.org/10.1038/s41598-023-32701-6.

[6] F. Arute, K. Arya, R. Babbush, D. Bacon, J.C. Bardin, R. Barends, R. Biswas, S. Boixo, F.G.S.L. Brandao, D.A. Buell, B. Burkett, Y. Chen, Z. Chen, B. Chiaro, R. Collins, W. Courtney, A. Dunsworth, E. Farhi, B. Foxen, A. Fowler, C. Gidney, M. Giustina, R. Graff, K. Guerin, S. Habegger, M.P. Harrigan, M.J. Hartmann, A. Ho, M. Hoffmann, T. Huang,

T.S. Humble, S. V. Isakov, E. Jeffrey, Z. Jiang, D. Kafri, K. Kechedzhi, J. Kelly, P. V. Klimov, S. Knysh, A. Korotkov, F. Kostritsa, D. Landhuis, M. Lindmark, E. Lucero, D. Lyakh, S. Mandrà, J.R. McClean, M. McEwen, A. Megrant, X. Mi, K. Michielsen, M. Mohseni, J. Mutus, O. Naaman, M. Neeley, C. Neill, M.Y. Niu, E. Ostby, A. Petukhov, J.C. Platt, C. Quintana, E.G. Rieffel, P. Roushan, N.C. Rubin, D. Sank, K.J. Satzinger, V. Smelyanskiy, K.J. Sung, M.D. Trevithick, A. Vainsencher, B. Villalonga, T. White, Z.J. Yao, P. Yeh, A. Zalcman, H. Neven, J.M. Martinis, Quantum supremacy using a programmable superconducting processor, Nature 2019 574:7779 574 (2019) 505–510. https://doi.org/10.1038/s41586-019-1666-5.

[7] H. Sen Zhong, H. Wang, Y.H. Deng, M.C. Chen, L.C. Peng, Y.H. Luo, J. Qin, D. Wu, X. Ding, Y. Hu, P. Hu, X.Y. Yang, W.J. Zhang, H. Li, Y. Li, X. Jiang, L. Gan, G. Yang, L. You, Z. Wang, L. Li, N. Le Liu, C.Y. Lu, J.W. Pan, Quantum computational advantage using photons, Science (1979) 370 (2020) 1460–1463. https://doi.org/10.1126/SCIENCE.ABE8770/SUPPL_FILE/ABE8770_ZHONG_SM.PDF.

[8] E. Schrödinger, Die gegenwärtige Situation in der Quantenmechanik, Naturwissenschaften 23 (1935) 807–812. https://doi.org/10.1007/BF01491891/METRICS.

[9] H. Bernien, B. Hensen, W. Pfaff, G. Koolstra, M.S. Blok, L. Robledo, T.H. Taminiau, M. Markham, D.J. Twitchen, L. Childress, R. Hanson, Heralded entanglement between solid-state qubits separated by three metres, Nature 2013 497:7447 497 (2013) 86–90. https://doi.org/10.1038/nature12016.

[10] G. Kurizki, P. Bertet, Y. Kubo, K. Mølmer, D. Petrosyan, P. Rabl, J. Schmiedmayer, Quantum technologies with hybrid systems, Proc Natl Acad Sci U S A 112 (2015) 3866–

3873. https://doi.org/10.1073/PNAS.1419326112/ASSET/33DDFB11-77D3-425F-8940-BC283445FFFF/ASSETS/GRAPHIC/PNAS.1419326112FIG04.JPEG.

[11] D.P. DiVincenzo, IBM, The Physical Implementation of Quantum Computation, Fortschritte Der Physik 48 (2000) 771–783. https://doi.org/10.1002/1521-3978(200009)48:9/11<771::AID-PROP771>3.0.CO;2-E.

[12] A. Gruber, A. Dräbenstedt, C. Tietz, L. Fleury, J. Wrachtrup, C. Von Borczyskowski, Scanning Confocal Optical Microscopy and Magnetic Resonance on Single Defect Centers, Science (1979) 276 (1997) 2012–2014. https://doi.org/10.1126/SCIENCE.276.5321.2012.

[13] G. Wolfowicz, F.J. Heremans, C.P. Anderson, S. Kanai, H. Seo, A. Gali, G. Galli, D.D. Awschalom, Quantum guidelines for solid-state spin defects, Nature Reviews Materials 2021 6:10 6 (2021) 906–925. https://doi.org/10.1038/s41578-021-00306-y.

[14] S.K. Parthasarathy, B. Kallinger, F. Kaiser, P. Berwian, D.B.R. Dasari, J. Friedrich, R. Nagy, Scalable Quantum Memory Nodes Using Nuclear Spins in Silicon Carbide, Phys Rev Appl 19 (2023) 034026. https://doi.org/10.1103/PHYSREVAPPLIED.19.034026/FIGURES/6/THUMBNAIL.

[15] D.M. Toyli, C.F. De Las Casas, D.J. Christle, V. V. Dobrovitski, D.D. Awschalom, Fluorescence thermometry enhanced by the quantum coherence of single spins in diamond, Proc Natl Acad Sci U S A 110 (2013) 8417–8421. https://doi.org/10.1073/PNAS.1306825110/SUPPL_FILE/SAPP.PDF.

[16] P. V. Klimov, A.L. Falk, D.J. Christle, V. V. Dobrovitski, D.D. Awschalom, Quantum entanglement at ambient conditions in a macroscopic solid-state spin ensemble, Sci Adv 1 (2015). https://doi.org/10.1126/SCIADV.1501015/SUPPL_FILE/1501015_SM.PDF.

[17] W.F. Koehl, B.B. Buckley, F.J. Heremans, G. Calusine, D.D. Awschalom, Room temperature coherent control of defect spin qubits in silicon carbide, Nature 2011 479:7371 479 (2011) 84–87. https://doi.org/10.1038/NATURE10562.

[18] E.D. Herbschleb, H. Kato, Y. Maruyama, T. Danjo, T. Makino, S. Yamasaki, I. Ohki, K. Hayashi, H. Morishita, M. Fujiwara, N. Mizuochi, Ultra-long coherence times amongst room-temperature solid-state spins, Nature Communications 2019 10:1 10 (2019) 1–6. https://doi.org/10.1038/s41467-019-11776-8.

[19] P.C. Maurer, G. Kucsko, C. Latta, L. Jiang, N.Y. Yao, S.D. Bennett, F. Pastawski, D. Hunger, N. Chisholm, M. Markham, D.J. Twitchen, J.I. Cirac, M.D. Lukin, Room-temperature quantum bit memory exceeding one second, Science (1979) 336 (2012) 1283–1286. https://doi.org/10.1126/SCIENCE.1220513/SUPPL_FILE/MAURER.SM.PDF.

[20] G. Balasubramanian, P. Neumann, D. Twitchen, M. Markham, R. Kolesov, N. Mizuochi, J. Isoya, J. Achard, J. Beck, J. Tissler, V. Jacques, P.R. Hemmer, F. Jelezko, J. Wrachtrup, Ultralong spin coherence time in isotopically engineered diamond, Nature Materials 2009 8:5 8 (2009) 383–387. https://doi.org/10.1038/nmat2420.

[21] A. Bourassa, C.P. Anderson, K.C. Miao, M. Onizhuk, H. Ma, A.L. Crook, H. Abe, J. Ul-Hassan, T. Ohshima, N.T. Son, G. Galli, D.D. Awschalom, Entanglement and control of single nuclear spins in isotopically engineered silicon carbide, Nature Materials 2020 19:12 19 (2020) 1319–1325. https://doi.org/10.1038/s41563-020-00802-6.

[22] F. Dolde, H. Fedder, M.W. Doherty, T. Nöbauer, F. Rempp, G. Balasubramanian, T. Wolf, F. Reinhard, L.C.L. Hollenberg, F. Jelezko, J. Wrachtrup, Electric-field sensing

using single diamond spins, Nature Physics 2011 7:6 7 (2011) 459–463. https://doi.org/10.1038/nphys1969.

[23] L. Robledo, L. Childress, H. Bernien, B. Hensen, P.F.A. Alkemade, R. Hanson, High-fidelity projective read-out of a solid-state spin quantum register, Nature 2011 477:7366 477 (2011) 574–578. https://doi.org/10.1038/nature10401.

[24] A.L. Falk, P. V. Klimov, B.B. Buckley, V. Ivády, I.A. Abrikosov, G. Calusine, W.F. Koehl, Á. Gali, D.D. Awschalom, Electrically and mechanically tunable electron spins in silicon carbide color centers, Phys Rev Lett 112 (2014) 187601. https://doi.org/10.1103/PHYSREVLETT.112.187601/FIGURES/4/MEDIUM.

[25] K.C. Miao, A. Bourassa, C.P. Anderson, S.J. Whiteley, A.L. Crook, S.L. Bayliss, G. Wolfowicz, G. Thiering, P. Udvarhelyi, V. Ivády, H. Abe, T. Ohshima, Á. Gali, D.D. Awschalom, Electrically driven optical interferometry with spins in silicon carbide, Sci Adv 5 (2019). https://doi.org/10.1126/SCIADV.AAY0527/SUPPL_FILE/AAY0527_SM.PDF.

[26] S.J. Whiteley, G. Wolfowicz, C.P. Anderson, A. Bourassa, H. Ma, M. Ye, G. Koolstra, K.J. Satzinger, M. V. Holt, F.J. Heremans, A.N. Cleland, D.I. Schuster, G. Galli, D.D. Awschalom, Spin–phonon interactions in silicon carbide addressed by Gaussian acoustics, Nature Physics 2019 15:5 15 (2019) 490–495. https://doi.org/10.1038/s41567-019-0420-0.

[27] C.P. Anderson, A. Bourassa, K.C. Miao, G. Wolfowicz, P.J. Mintun, A.L. Crook, H. Abe, J. Ul Hassan, N.T. Son, T. Ohshima, D.D. Awschalom, Electrical and optical control of single spins integrated in scalable semiconductor devices, Science (1979) 366 (2019) 1225–1230. https://doi.org/10.1126/SCIENCE.AAX9406/SUPPL_FILE/AAX9406-ANDERSON-SM.PDF.

[28] C.P. Anderson, E.O. Glen, C. Zeledon, A. Bourassa, Y. Jin, Y. Zhu, C. Vorwerk, A.L. Crook, H. Abe, J. Ul-Hassan, T. Ohshima, N.T. Son, G. Galli, D.D. Awschalom, Five-second coherence of a single spin with single-shot readout in silicon carbide, Sci Adv 8 (2022). https://doi.org/10.1126/SCIADV.ABM5912/SUPPL_FILE/SCIADV.ABM5912_SM.PDF.

[29] Y. Kubo, F.R. Ong, P. Bertet, D. Vion, V. Jacques, D. Zheng, A. Dréau, J.F. Roch, A. Auffeves, F. Jelezko, J. Wrachtrup, M.F. Barthe, P. Bergonzo, D. Esteve, Strong coupling of a spin ensemble to a superconducting resonator, Phys Rev Lett 105 (2010) 140502. https://doi.org/10.1103/PHYSREVLETT.105.140502/FIGURES/3/MEDIUM.

[30] A.L. Crook, C.P. Anderson, K.C. Miao, A. Bourassa, H. Lee, S.L. Bayliss, D.O. Bracher, X. Zhang, H. Abe, T. Ohshima, E.L. Hu, D.D. Awschalom, Purcell enhancement of a single silicon carbide color center with coherent spin control, Nano Lett 20 (2020) 3427–3434. https://doi.org/10.1021/ACS.NANOLETT.0C00339/ASSET/IMAGES/LARGE/NL0C00339_0004.JPEG.

[31] B. Hensen, H. Bernien, A.E. Dreaú, A. Reiserer, N. Kalb, M.S. Blok, J. Ruitenberg, R.F.L. Vermeulen, R.N. Schouten, C. Abellán, W. Amaya, V. Pruneri, M.W. Mitchell, M. Markham, D.J. Twitchen, D. Elkouss, S. Wehner, T.H. Taminiau, R. Hanson, Loophole-free Bell inequality violation using electron spins separated by 1.3 kilometres, Nature 2015 526:7575 526 (2015) 682–686. https://doi.org/10.1038/nature15759.

[32] A. Einstein, No Title, Phys. Z. 10 (1909).

[33] S. Stenholm, The semiclassical theory of laser cooling, Rev Mod Phys 58 (1986) 699. https://doi.org/10.1103/RevModPhys.58.699.

[34] M. Underwood, D. Mason, D. Lee, H. Xu, L. Jiang, A.B. Shkarin, K. Børkje, S.M. Girvin, J.G.E. Harris, Measurement of the motional sidebands of a nanogram-scale oscillator in the quantum regime, Phys Rev A 92 (2015). https://doi.org/10.1103/PHYSREVA.92.061801.

[35] R.W. Peterson, T.P. Purdy, N.S. Kampel, R.W. Andrews, P.L. Yu, K.W. Lehnert, C.A. Regal, Laser Cooling of a Micromechanical Membrane to the Quantum Backaction Limit, Phys Rev Lett 116 (2016) 063601. https://doi.org/10.1103/PHYSREVLETT.116.063601/FIGURES/3/THUMBNAIL.

[36] M. Rossi, D. Mason, J. Chen, Y. Tsaturyan, A. Schliesser, Measurement-based quantum control of mechanical motion, Nature 2018 563:7729 563 (2018) 53–58. https://doi.org/10.1038/s41586-018-0643-8.

[37] Y. Chu, S. Gröblacher, A perspective on hybrid quantum opto- and electromechanical systems, Appl Phys Lett 117 (2020). https://doi.org/10.1063/5.0021088.

[38] B.M. Brubaker, J.M. Kindem, M.D. Urmey, S. Mittal, R.D. Delaney, P.S. Burns, M.R. Vissers, K.W. Lehnert, C.A. Regal, Optomechanical Ground-State Cooling in a Continuous and Efficient Electro-Optic Transducer, Phys Rev X 12 (2022) 021062. https://doi.org/10.1103/PHYSREVX.12.021062/FIGURES/10/MEDIUM.

[39] D.J. Christle, A.L. Falk, P. Andrich, P. V. Klimov, J.U. Hassan, N.T. Son, E. Janzén, T. Ohshima, D.D. Awschalom, Isolated electron spins in silicon carbide with millisecond coherence times, Nat Mater 14 (2015) 160–163. https://doi.org/10.1038/nmat4144.

[40] D.J. Christle, P. V. Klimov, C.F. de las Casas, K. Szász, V. Ivády, V. Jokubavicius, J.U. Hassan, M. Syväjärvi, W.F. Koehl, T. Ohshima, N.T. Son, E. Janzén, ádám Gali, D.D. Awschalom, Isolated spin qubits in SiC with a high-fidelity infrared spin-to-photon interface, Phys Rev X 7 (2017) 021046. https://doi.org/10.1103/PHYSREVX.7.021046/FIGURES/4/MEDIUM.

[41] A.L. Falk, B.B. Buckley, G. Calusine, W.F. Koehl, V. V. Dobrovitski, A. Politi, C.A. Zorman, P.X.L. Feng, D.D. Awschalom, Polytype control of spin qubits in silicon carbide, Nat Commun 4 (2013). https://doi.org/10.1038/ncomms2854.

[42] N.T. Son, C.P. Anderson, A. Bourassa, K.C. Miao, C. Babin, M. Widmann, M. Niethammer, J. Ul Hassan, N. Morioka, I.G. Ivanov, F. Kaiser, J. Wrachtrup, D.D. Awschalom, Developing silicon carbide for quantum spintronics, Appl Phys Lett 116 (2020). https://doi.org/10.1063/5.0004454.

[43] N.T. Son, P. Carlsson, J. Ul Hassan, E. Janzén, T. Umeda, J. Isoya, A. Gali, M. Bockstedte, N. Morishita, T. Ohshima, H. Itoh, Divacancy in 4H-SiC, Phys Rev Lett 96 (2006). https://doi.org/10.1103/PhysRevLett.96.055501.

[44] D.J. Christle, P. V. Klimov, C.F. de las Casas, K. Szász, V. Ivády, V. Jokubavicius, J.U. Hassan, M. Syväjärvi, W.F. Koehl, T. Ohshima, N.T. Son, E. Janzén, ádám Gali, D.D. Awschalom, Isolated spin qubits in SiC with a high-fidelity infrared spin-to-photon interface, Phys Rev X 7 (2017). https://doi.org/10.1103/PhysRevX.7.021046.

[45] S. Castelletto, L. Rosa, B.C. Johnson, S. Castelletto, L. Rosa, B.C. Johnson, Silicon Carbide for Novel Quantum Technology Devices, Advanced Silicon Carbide Devices and Processing (2015). https://doi.org/10.5772/61166.

[46] J.R. Weber, W.F. Koehl, J.B. Varley, A. Janotti, B.B. Buckley, C.G. Van De Walle, D.D. Awschalom, Quantum computing with defects, Proc Natl Acad Sci U S A 107 (2010) 8513–8518. https://doi.org/10.1073/PNAS.1003052107/SUPPL_FILE/PNAS.1003052107_SI.PDF.

[47] A.L. Crook, C.P. Anderson, K.C. Miao, A. Bourassa, H. Lee, S.L. Bayliss, D.O. Bracher, X. Zhang, H. Abe, T. Ohshima, E.L. Hu, D.D. Awschalom, Purcell enhancement of a single silicon carbide color center with coherent spin control, Nano Lett 20 (2020) 3427–3434. https://doi.org/10.1021/ACS.NANOLETT.0C00339/SUPPL_FILE/NL0C00339_SI_001.PDF.

[48] D.O. Bracher, X. Zhang, E.L. Hu, Selective Purcell enhancement of two closely linked zero-phonon transitions of a silicon carbide color center, Proc Natl Acad Sci U S A 114 (2017) 4060–4065. https://doi.org/10.1073/PNAS.1704219114/ASSET/23BBF33B-E5B8-4FAA-A47A-920E522F2E0E/ASSETS/GRAPHIC/PNAS.1704219114FIG05.JPEG.

[49] G. Calusine, A. Politi, D.D. Awschalom, Cavity-Enhanced Measurements of Defect Spins in Silicon Carbide, Phys Rev Appl 6 (2016). https://doi.org/10.1103/PhysRevApplied.6.014019.

[50] X. Lu, J.Y. Lee, P.X.L. Feng, Q. Lin, High Q silicon carbide microdisk resonator, Appl Phys Lett 104 (2014). https://doi.org/10.1063/1.4875707/24141.

[51] J.Y. Lee, X. Lu, Q. Lin, High-Q silicon carbide photonic-crystal cavities, Appl Phys Lett 106 (2015). https://doi.org/10.1063/1.4906923/13824622/041106_1_ACCEPTED_MANUSCRIPT.PDF.

[52] J. Cardenas, C.T. Phare, B. Guha, M. Lipson, C.B. Poitras, M. Zhang, S.Y. Shah, High Q SiC microresonators, Optics Express, Vol. 21, Issue 14, Pp. 16882-16887 21 (2013) 16882–16887. https://doi.org/10.1364/OE.21.016882.

[53] X. Guo, Q. Xun, Z. Li, S. Du, Silicon Carbide Converters and MEMS Devices for High-temperature Power Electronics: A Critical Review, Micromachines 2019, Vol. 10, Page 406 10 (2019) 406. https://doi.org/10.3390/MI10060406.

[54] C.A. Zorman, R.J. Parro, Micro- and nanomechanical structures for silicon carbide MEMS and NEMS, Physica Status Solidi (b) 245 (2008) 1404–1424. https://doi.org/10.1002/PSSB.200844135.

[55] A.A. Lebedev, Radiation Effects in Silicon Carbide, (2017). https://doi.org/10.21741/9781945291111.

[56] Z. Zolnai, Irradiation-induced crystal defects in silicon carbide Ph.D. Thesis, (2005).

[57] P. V. Klimov, A.L. Falk, D.J. Christle, V. V. Dobrovitski, D.D. Awschalom, Quantum entanglement at ambient conditions in a macroscopic solid-state spin ensemble, Sci Adv 1 (2015). https://doi.org/10.1126/SCIADV.1501015/SUPPL_FILE/1501015_SM.PDF.

[58] J.R. Maze, A. Gali, E. Togan, Y. Chu, A. Trifonov, E. Kaxiras, M.D. Lukin, Properties of nitrogen-vacancy centers in diamond: the group theoretic approach, New J Phys 13 (2011) 025025. https://doi.org/10.1088/1367-2630/13/2/025025.

[59] S. Meiboom, D. Gill, Modified Spin-Echo Method for Measuring Nuclear Relaxation Times, Review of Scientific Instruments 29 (1958) 688–691. https://doi.org/10.1063/1.1716296.

[60] L. Kevan, Electron paramagnetic resonance: Elementary theory and practical applications, Foundations of Physics 1997 27:6 27 (1997) 959–960. https://doi.org/10.1007/BF02550350.

[61] Y. Chu, M.D. Lukin, Quantum optics with nitrogen-vacancy centers in diamond, Quantum Optics and Nanophotonics (2015) 229–270. https://doi.org/10.1093/oso/9780198768609.003.0005.

[62] M.L. Goldman, M.W. Doherty, A. Sipahigil, N.Y. Yao, S.D. Bennett, N.B. Manson, A. Kubanek, M.D. Lukin, State-selective intersystem crossing in nitrogen-vacancy centers, Phys Rev B Condens Matter Mater Phys 91 (2015) 165201. https://doi.org/10.1103/PHYSREVB.91.165201/FIGURES/9/MEDIUM.

[63] M.L. Goldman, A. Sipahigil, M.W. Doherty, N.Y. Yao, S.D. Bennett, M. Markham, D.J. Twitchen, N.B. Manson, A. Kubanek, M.D. Lukin, Phonon-induced population dynamics and intersystem crossing in nitrogen-vacancy centers, Phys Rev Lett 114 (2015) 145502. https://doi.org/10.1103/PHYSREVLETT.114.145502/FIGURES/4/MEDIUM.

[64] H.Y. Carr, E.M. Purcell, Effects of Diffusion on Free Precession in Nuclear Magnetic Resonance Experiments, Physical Review 94 (1954) 630. https://doi.org/10.1103/PhysRev.94.630.

[65] A. Barfuss, J. Teissier, E. Neu, A. Nunnenkamp, P. Maletinsky, Strong mechanical driving of a single electron spin, Nature Physics 2015 11:10 11 (2015) 820–824. https://doi.org/10.1038/nphys3411.

[66] H.Y. Chen, E.R. MacQuarrie, G.D. Fuchs, Orbital State Manipulation of a Diamond Nitrogen-Vacancy Center Using a Mechanical Resonator, Phys Rev Lett 120 (2018) 167401. https://doi.org/10.1103/PHYSREVLETT.120.167401/FIGURES/4/MEDIUM.

[67] E. Bauch, C.A. Hart, J.M. Schloss, M.J. Turner, J.F. Barry, P. Kehayias, S. Singh, R.L. Walsworth, Ultralong Dephasing Times in Solid-State Spin Ensembles via Quantum Control, Phys Rev X 8 (2018) 031025. https://doi.org/10.1103/PHYSREVX.8.031025/FIGURES/4/MEDIUM.

[68] H. Seo, A.L. Falk, P. V. Klimov, K.C. Miao, G. Galli, D.D. Awschalom, Quantum decoherence dynamics of divacancy spins in silicon carbide, Nature Communications 2016 7:1 7 (2016) 1–9. https://doi.org/10.1038/ncomms12935.

[69] D.M. Toyli, C.F. De Las Casas, D.J. Christle, V. V. Dobrovitski, D.D. Awschalom, Fluorescence thermometry enhanced by the quantum coherence of single spins in diamond, Proc Natl Acad Sci U S A 110 (2013) 8417–8421. https://doi.org/10.1073/PNAS.1306825110/SUPPL_FILE/SAPP.PDF.

[70] K.M. Itoh, H. Watanabe, Isotope engineering of silicon and diamond for quantum computing and sensing applications, MRS Communications 2014 4:4 4 (2014) 143–157. https://doi.org/10.1557/MRC.2014.32.

[71] N. Bar-Gill, L.M. Pham, C. Belthangady, D. Le Sage, P. Cappellaro, J.R. Maze, M.D. Lukin, A. Yacoby, R. Walsworth, Suppression of spin-bath dynamics for improved coherence of multi-spin-qubit systems, Nature Communications 2012 3:1 3 (2012) 1–6. https://doi.org/10.1038/ncomms1856.

[72] E.R. Macquarrie, T.A. Gosavi, S.A. Bhave, G.D. Fuchs, Continuous dynamical decoupling of a single diamond nitrogen-vacancy center spin with a mechanical resonator, Phys Rev B Condens Matter Mater Phys 92 (2015) 224419. https://doi.org/10.1103/PHYSREVB.92.224419/FIGURES/10/MEDIUM.

[73] J. Teissier, A. Barfuss, P. Maletinsky, Hybrid continuous dynamical decoupling: a photon-phonon doubly dressed spin, Journal of Optics 19 (2017) 044003. https://doi.org/10.1088/2040-8986/AA5F62.

[74] X. Xu, Z. Wang, C. Duan, P. Huang, P. Wang, Y. Wang, N. Xu, X. Kong, F. Shi, X. Rong, J. Du, Coherence-protected quantum gate by continuous dynamical decoupling in diamond, Phys Rev Lett 109 (2012) 070502. https://doi.org/10.1103/PHYSREVLETT.109.070502/FIGURES/4/MEDIUM.

[75] J.M. Cai, B. Naydenov, R. Pfeiffer, L.P. McGuinness, K.D. Jahnke, F. Jelezko, M.B. Plenio, A. Retzker, Robust dynamical decoupling with concatenated continuous driving, New J Phys 14 (2012) 113023. https://doi.org/10.1088/1367-2630/14/11/113023.

[76] A. Laucht, R. Kalra, S. Simmons, J.P. Dehollain, J.T. Muhonen, F.A. Mohiyaddin, S. Freer, F.E. Hudson, K.M. Itoh, D.N. Jamieson, J.C. McCallum, A.S. Dzurak, A. Morello, A dressed spin qubit in silicon, Nature Nanotechnology 2016 12:1 12 (2016) 61–66. https://doi.org/10.1038/nnano.2016.178.

[77] A. Stark, N. Aharon, A. Huck, H.A.R. El-Ella, A. Retzker, F. Jelezko, U.L. Andersen, Clock transition by continuous dynamical decoupling of a three-level system, Scientific Reports 2018 8:1 8 (2018) 1–8. https://doi.org/10.1038/s41598-018-31984-4.

[78] T. Van Der Sar, Z.H. Wang, M.S. Blok, H. Bernien, T.H. Taminiau, D.M. Toyli, D.A. Lidar, D.D. Awschalom, R. Hanson, V. V. Dobrovitski, Decoherence-protected quantum gates for a hybrid solid-state spin register, Nature 2012 484:7392 484 (2012) 82–86. https://doi.org/10.1038/nature10900.

[79] T.H. Taminiau, J.J.T. Wagenaar, T. Van Der Sar, F. Jelezko, V. V. Dobrovitski, R. Hanson, Detection and control of individual nuclear spins using a weakly coupled electron

spin, Phys Rev Lett 109 (2012) 137602. https://doi.org/10.1103/PHYSREVLETT.109.137602/FIGURES/4/MEDIUM.

[80] G. De Lange, Z.H. Wang, D. Ristè, V. V. Dobrovitski, R. Hanson, Universal dynamical decoupling of a single solid-state spin from a spin bath, Science (1979) 330 (2010) 60–63. https://doi.org/10.1126/SCIENCE.1192739/SUPPL_FILE/DELANGE.SOM.PDF.

[81] M. Lucamarini, G. Di Giuseppe, S. Damodarakurup, D. Vitali, P. Tombesi, Suppression of polarization decoherence for traveling light pulses via bang-bang dynamical decoupling, Phys Rev A 83 (2011) 032320. https://doi.org/10.1103/PHYSREVA.83.032320/FIGURES/15/MEDIUM.

[82] M. Onizhuk, K.C. Miao, J.P. Blanton, H. Ma, C.P. Anderson, A. Bourassa, D.D. Awschalom, G. Galli, Probing the Coherence of Solid-State Qubits at Avoided Crossings, PRX Quantum 2 (2021) 010311. https://doi.org/10.1103/PRXQUANTUM.2.010311/FIGURES/17/MEDIUM.

[83] Z. Mu, S.A. Zargaleh, H.J. Von Bardeleben, J.E. Fröch, M. Nonahal, H. Cai, X. Yang, J. Yang, X. Li, I. Aharonovich, W. Gao, Coherent Manipulation with Resonant Excitation and Single Emitter Creation of Nitrogen Vacancy Centers in 4H Silicon Carbide, Nano Lett 20 (2020) 6142–6147. https://doi.org/10.1021/ACS.NANOLETT.0C02342/SUPPL_FILE/NL0C02342_SI_001.PDF.

[84] H.H. Vallabhapurapu, I. Hansen, C. Adambukulam, R. Stöhr, A. Denisenko, C.H. Yang, A. Laucht, High-fidelity control of a nitrogen-vacancy-center spin qubit at room temperature using the sinusoidally modulated, always rotating, and tailored protocol, Phys

Rev A (Coll Park) 108 (2023) 022606. https://doi.org/10.1103/PHYSREVA.108.022606/FIGURES/5/MEDIUM.

[85] R. Babar, G. Barcza, A. Pershin, H. Park, O. Bulancea Lindvall, G. Thiering, Ö. Legeza, J.H. Warner, I.A. Abrikosov, A. Gali, V. Ivády, Low-symmetry vacancy-related spin qubit in hexagonal boron nitride, Npj Computational Materials 2024 10:1 10 (2024) 1–9. https://doi.org/10.1038/s41524-024-01361-z.

[86] K.J. Morse, P. Dluhy, J. Huber, J.Z. Salvail, K. Saeedi, H. Riemann, N. V. Abrosimov, P. Becker, H.J. Pohl, S. Simmons, M.L.W. Thewalt, Zero-field optical magnetic resonance study of phosphorus donors in 28-silicon, Phys Rev B 97 (2018) 115205. https://doi.org/10.1103/PHYSREVB.97.115205/FIGURES/4/MEDIUM.

[87] G. Wolfowicz, A.M. Tyryshkin, R.E. George, H. Riemann, N. V. Abrosimov, P. Becker, H.J. Pohl, M.L.W. Thewalt, S.A. Lyon, J.J.L. Morton, Atomic clock transitions in silicon-based spin qubits, Nature Nanotechnology 2013 8:8 8 (2013) 561–564. https://doi.org/10.1038/nnano.2013.117.

[88] S.L. Bayliss, D.W. Laorenza, P.J. Mintun, B.D. Kovos, D.E. Freedman, D.D. Awschalom, Optically addressable molecular spins for quantum information processing, Science (1979) 370 (2020) 1309–1312. https://doi.org/10.1126/SCIENCE.ABB9352/SUPPL_FILE/ABB9352_BAYLISS_SM.PDF.

[89] C. Grezes, B. Julsgaard, Y. Kubo, M. Stern, T. Umeda, J. Isoya, H. Sumiya, H. Abe, S. Onoda, T. Ohshima, V. Jacques, J. Esteve, D. Vion, D. Esteve, K. Mølmer, P. Bertet, Multimode storage and retrieval of microwave fields in a spin ensemble, Phys Rev X 4 (2014) 021049. https://doi.org/10.1103/PHYSREVX.4.021049/FIGURES/5/MEDIUM.

[90] N. Kalb, A.A. Reiserer, P.C. Humphreys, J.J.W. Bakermans, S.J. Kamerling, N.H. Nickerson, S.C. Benjamin, D.J. Twitchen, M. Markham, R. Hanson, Entanglement distillation between solid-state quantum network nodes, Science (1979) 356 (2017) 928–932. https://doi.org/10.1126/SCIENCE.AAN0070/SUPPL_FILE/AAN0070_KALB_SM.PDF.

[91] P.C. Humphreys, N. Kalb, J.P.J. Morits, R.N. Schouten, R.F.L. Vermeulen, D.J. Twitchen, M. Markham, R. Hanson, Deterministic delivery of remote entanglement on a quantum network, Nature 2018 558:7709 558 (2018) 268–273. https://doi.org/10.1038/s41586-018-0200-5.

[92] A.A. Clerk, K.W. Lehnert, P. Bertet, J.R. Petta, Y. Nakamura, Hybrid quantum systems with circuit quantum electrodynamics, Nature Physics 2020 16:3 16 (2020) 257–267. https://doi.org/10.1038/s41567-020-0797-9.

[93] A. Reiserer, G. Rempe, Cavity-based quantum networks with single atoms and optical photons, Rev Mod Phys 87 (2015) 1379–1418. https://doi.org/10.1103/REVMODPHYS.87.1379/FIGURES/24/MEDIUM.

[94] M. Pelton, Modified spontaneous emission in nanophotonic structures, Nature Photonics 2015 9:7 9 (2015) 427–435. https://doi.org/10.1038/nphoton.2015.103.

[95] J. Vuckovic, Quantum optics and cavity QED with quantum dots in photonic crystals, Quantum Optics and Nanophotonics (2014) 365–406. https://doi.org/10.1093/oso/9780198768609.003.0008.

[96] D. Huang, A. Abulnaga, S. Welinski, M. Raha, J.D. Thompson, N.P. de Leon, Hybrid III-V diamond photonic platform for quantum nodes based on neutral silicon vacancy centers in diamond, Opt Express 29 (2021) 9174. https://doi.org/10.1364/OE.418081.

[97] J. Yang, M.M. Fejer, K.Y. Yang, A. Markosyan, D.M. Lukin, M.A. Guidry, J. Vučković, Optical parametric oscillation in silicon carbide nanophotonics, Optica, Vol. 7, Issue 9, Pp. 1139-1142 7 (2020) 1139–1142. https://doi.org/10.1364/OPTICA.394138.

[98] R. Flaminio, J. Degallaix, L. Pinard, N. Straniero, G. Cagnoli, Realistic loss estimation due to the mirror surfaces in a 10 meters-long high finesse Fabry-Perot filter-cavity, Optics Express, Vol. 23, Issue 16, Pp. 21455-21476 23 (2015) 21455–21476. https://doi.org/10.1364/OE.23.021455.

[99] M. Aspelmeyer, T.J. Kippenberg, F. Marquardt, Cavity optomechanics, Rev Mod Phys 86 (2014) 1391–1452. https://doi.org/10.1103/REVMODPHYS.86.1391/FIGURES/46/MEDIUM.

[100] A. Dorsel, J.D. McCullen, P. Meystre, E. Vignes, H. Walther, Optical Bistability and Mirror Confinement Induced by Radiation Pressure, Phys Rev Lett 51 (1983) 1550. https://doi.org/10.1103/PhysRevLett.51.1550.

[101] T.J. Kippenberg, K.J. Vahala, Cavity Optomechanics: Back-Action at the Mesoscale, Science (1979) 321 (2008) 1172–1176. https://doi.org/10.1126/SCIENCE.1156032.

[102] C. Genes, D. Vitali, P. Tombesi, S. Gigan, M. Aspelmeyer, Ground-state cooling of a micromechanical oscillator: Comparing cold damping and cavity-assisted cooling schemes, Phys Rev A 77 (2008) 033804. https://doi.org/10.1103/PHYSREVA.77.033804/FIGURES/4/THUMBNAIL.

[103] S. Weis, R. Rivière, S. Deléglise, E. Gavartin, O. Arcizet, A. Schliesser, T.J. Kippenberg, Optomechanically induced transparency, Science (1979) 330 (2010) 1520–1523. https://doi.org/10.1126/SCIENCE.1195596/SUPPL_FILE/WEIS_SOM.PDF.

[104] M. Schleier-Smith, Editorial: Hybridizing Quantum Physics and Engineering, Phys Rev Lett 117 (2016) 100001. https://doi.org/10.1103/PhysRevLett.117.100001.

[105] D. Awschalom, K.K. Berggren, H. Bernien, S. Bhave, L.D. Carr, P. Davids, S.E. Economou, D. Englund, A. Faraon, M. Fejer, S. Guha, M. V. Gustafsson, E. Hu, L. Jiang, J. Kim, B. Korzh, P. Kumar, P.G. Kwiat, M. Lončar, M.D. Lukin, D.A.B. Miller, C. Monroe, S.W. Nam, P. Narang, J.S. Orcutt, M.G. Raymer, A.H. Safavi-Naeini, M. Spiropulu, K. Srinivasan, S. Sun, J. Vučković, E. Waks, R. Walsworth, A.M. Weiner, Z. Zhang, Development of Quantum Interconnects (QuICs) for Next-Generation Information Technologies, PRX Quantum 2 (2021) 017002. https://doi.org/10.1103/PRXQUANTUM.2.017002/FIGURES/1/MEDIUM.

[106] R. Acharya, I. Aleiner, R. Allen, T.I. Andersen, M. Ansmann, F. Arute, K. Arya, A. Asfaw, J. Atalaya, R. Babbush, D. Bacon, J.C. Bardin, J. Basso, A. Bengtsson, S. Boixo, G. Bortoli, A. Bourassa, J. Bovaird, L. Brill, M. Broughton, B.B. Buckley, D.A. Buell, T. Burger, B. Burkett, N. Bushnell, Y. Chen, Z. Chen, B. Chiaro, J. Cogan, R. Collins, P. Conner, W. Courtney, A.L. Crook, B. Curtin, D.M. Debroy, A. Del Toro Barba, S. Demura, A. Dunsworth, D. Eppens, C. Erickson, L. Faoro, E. Farhi, R. Fatemi, L. Flores Burgos, E. Forati, A.G. Fowler, B. Foxen, W. Giang, C. Gidney, D. Gilboa, M. Giustina, A. Grajales Dau, J.A. Gross, S. Habegger, M.C. Hamilton, M.P. Harrigan, S.D. Harrington, O. Higgott, J. Hilton, M. Hoffmann, S. Hong, T. Huang, A. Huff, W.J. Huggins, L.B. Ioffe, S. V. Isakov, J. Iveland, E. Jeffrey, Z. Jiang, C. Jones, P. Juhas, D. Kafri, K. Kechedzhi, J. Kelly, T. Khattar, M. Khezri, M. Kieferová, S. Kim, A. Kitaev, P. V. Klimov, A.R. Klots, A.N. Korotkov, F. Kostritsa, J.M. Kreikebaum, D. Landhuis, P. Laptev, K.M. Lau, L. Laws, J. Lee, K. Lee, B.J. Lester, A. Lill, W. Liu, A. Locharla, E.

Lucero, F.D. Malone, J. Marshall, O. Martin, J.R. McClean, T. McCourt, M. McEwen, A. Megrant, B. Meurer Costa, X. Mi, K.C. Miao, M. Mohseni, S. Montazeri, A. Morvan, E. Mount, W. Mruczkiewicz, O. Naaman, M. Neeley, C. Neill, A. Nersisyan, H. Neven, M. Newman, J.H. Ng, A. Nguyen, M. Nguyen, M.Y. Niu, T.E. O'Brien, A. Opremcak, J. Platt, A. Petukhov, R. Potter, L.P. Pryadko, C. Quintana, P. Roushan, N.C. Rubin, N. Saei, D. Sank, K. Sankaragomathi, K.J. Satzinger, H.F. Schurkus, C. Schuster, M.J. Shearn, A. Shorter, V. Shvarts, J. Skruzny, V. Smelyanskiy, W.C. Smith, G. Sterling, D. Strain, M. Szalay, A. Torres, G. Vidal, B. Villalonga, C. Vollgraff Heidweiller, T. White, C. Xing, Z.J. Yao, P. Yeh, J. Yoo, G. Young, A. Zalcman, Y. Zhang, N. Zhu, Suppressing quantum errors by scaling a surface code logical qubit, Nature 2023 614:7949 614 (2023) 676–681. https://doi.org/10.1038/s41586-022-05434-1.

[107] N. Lauk, N. Sinclair, S. Barzanjeh, J.P. Covey, M. Saffman, M. Spiropulu, C. Simon, Perspectives on quantum transduction, Quantum Sci Technol 5 (2020) 020501. https://doi.org/10.1088/2058-9565/AB788A.

[108] M. Guha Majumdar, Quantum Transduction Using Optoelectromechanical Systems: Conversion of Quantum Information Between Optical and Microwave Systems, Resonance 27 (2022) 1703–1717. https://doi.org/10.1007/S12045-022-1465-4/METRICS.

[109] R. Stockill, M.J. Stanley, L. Huthmacher, E. Clarke, M. Hugues, A.J. Miller, C. Matthiesen, C. Le Gall, M. Atatüre, Phase-Tuned Entangled State Generation between Distant Spin Qubits, Phys Rev Lett 119 (2017) 010503. https://doi.org/10.1103/PHYSREVLETT.119.010503/SUPPLEMENTARY.PDF.

[110] J. Hofmann, M. Krug, N. Ortegel, L. Gérard, M. Weber, W. Rosenfeld, H. Weinfurter, Heralded entanglement between widely separated atoms, Science (1979) 336 (2012) 72–75. https://doi.org/10.1126/SCIENCE.1221856/SUPPL_FILE/HOFMANN.SM.PDF.

[111] D.L. Moehring, P. Maunz, S. Olmschenk, K.C. Younge, D.N. Matsukevich, L.M. Duan, C. Monroe, Entanglement of single-atom quantum bits at a distance, Nature 2007 449:7158 449 (2007) 68–71. https://doi.org/10.1038/nature06118.

[112] R. Stockill, M.J. Stanley, L. Huthmacher, E. Clarke, M. Hugues, A.J. Miller, C. Matthiesen, C. Le Gall, M. Atatüre, Phase-Tuned Entangled State Generation between Distant Spin Qubits, Phys Rev Lett 119 (2017) 010503. https://doi.org/10.1103/PHYSREVLETT.119.010503/SUPPLEMENTARY.PDF.

[113] L.J. Stephenson, D.P. Nadlinger, B.C. Nichol, S. An, P. Drmota, T.G. Ballance, K. Thirumalai, J.F. Goodwin, D.M. Lucas, C.J. Ballance, High-Rate, High-Fidelity Entanglement of Qubits Across an Elementary Quantum Network, Phys Rev Lett 124 (2020) 110501. https://doi.org/10.1103/PHYSREVLETT.124.110501/AB-PAPER-SUPPLEMENTAL.PDF.

[114] V. Krutyanskiy, M. Galli, V. Krcmarsky, S. Baier, D.A. Fioretto, Y. Pu, A. Mazloom, P. Sekatski, M. Canteri, M. Teller, J. Schupp, J. Bate, M. Meraner, N. Sangouard, B.P. Lanyon, T.E. Northup, Entanglement of Trapped-Ion Qubits Separated by 230 Meters, Phys Rev Lett 130 (2023) 050803. https://doi.org/10.1103/PHYSREVLETT.130.050803/SUPP_MAT.PDF.

[115] A. Tchebotareva, S.L.N. Hermans, P.C. Humphreys, D. Voigt, P.J. Harmsma, L.K. Cheng, A.L. Verlaan, N. Dijkhuizen, W. De Jong, A. Dréau, R. Hanson, Entanglement between a Diamond Spin Qubit and a Photonic Time-Bin Qubit at Telecom Wavelength, Phys Rev

Lett 123 (2019) 063601. https://doi.org/10.1103/PHYSREVLETT.123.063601/FIGURES/4/MEDIUM.

[116] A.J. Stolk, K.L. van der Enden, M.-C. Slater, I. te Raa-Derckx, P. Botma, J. van Rantwijk, B. Biemond, R.A.J. Hagen, R.W. Herfst, W.D. Koek, A.J.H. Meskers, R. Vollmer, E.J. van Zwet, M. Markham, A.M. Edmonds, J.F. Geus, F. Elsen, B. Jungbluth, C. Haefner, C. Tresp, J. Stuhler, S. Ritter, R. Hanson, Metropolitan-scale heralded entanglement of solid-state qubits, Sci Adv 10 (2024). https://doi.org/10.1126/sciadv.adp6442.

[117] Z. Bao, S. Xu, Z. Song, K. Wang, L. Xiang, Z. Zhu, J. Chen, F. Jin, X. Zhu, Y. Gao, Y. Wu, C. Zhang, N. Wang, Y. Zou, Z. Tan, A. Zhang, Z. Cui, F. Shen, J. Zhong, T. Li, J. Deng, X. Zhang, H. Dong, P. Zhang, Y.-R. Liu, L. Zhao, J. Hao, H. Li, Z. Wang, C. Song, Q. Guo, B. Huang, H. Wang, Creating and controlling global Greenberger-Horne-Zeilinger entanglement on quantum processors, Nature Communications 2024 15:1 15 (2024) 1–7. https://doi.org/10.1038/s41467-024-53140-5.

[118] C.E. Bradley, J. Randall, M.H. Abobeih, R.C. Berrevoets, M.J. Degen, M.A. Bakker, M. Markham, D.J. Twitchen, T.H. Taminiau, A Ten-Qubit Solid-State Spin Register with Quantum Memory up to One Minute, Phys Rev X 9 (2019) 031045. https://doi.org/10.1103/PHYSREVX.9.031045/FIGURES/8/THUMBNAIL.

[119] A.J. Stolk, K.L. van der Enden, M.-C. Slater, I. te Raa-Derckx, P. Botma, J. van Rantwijk, B. Biemond, R.A.J. Hagen, R.W. Herfst, W.D. Koek, A.J.H. Meskers, R. Vollmer, E.J. van Zwet, M. Markham, A.M. Edmonds, J.F. Geus, F. Elsen, B. Jungbluth, C. Haefner, C. Tresp, J. Stuhler, S. Ritter, R. Hanson, Metropolitan-scale heralded entanglement of solid-state qubits, Sci Adv (2024). https://doi.org/10.1126/SCIADV.ADP6442/SUPPL_FILE/SCIADV.ADP6442_SM.PDF.

[120] D. Riedel, I. Söllner, B.J. Shields, S. Starosielec, P. Appel, E. Neu, P. Maletinsky, R.J. Warburton, Deterministic enhancement of coherent photon generation from a nitrogen-vacancy center in ultrapure diamond, Phys Rev X 7 (2017) 031040. https://doi.org/10.1103/PHYSREVX.7.031040/FIGURES/4/MEDIUM.

[121] M. Ruf, M.J. Weaver, S.B. Van Dam, R. Hanson, Resonant Excitation and Purcell Enhancement of Coherent Nitrogen-Vacancy Centers Coupled to a Fabry-Perot Microcavity, Phys Rev Appl 15 (2021) 024049. https://doi.org/10.1103/PHYSREVAPPLIED.15.024049/FIGURES/12/MEDIUM.

[122] W. Hease, A. Rueda, R. Sahu, M. Wulf, G. Arnold, H.G.L. Schwefel, J.M. Fink, Bidirectional Electro-Optic Wavelength Conversion in the Quantum Ground State, PRX Quantum 1 (2020) 020315. https://doi.org/10.1103/PRXQUANTUM.1.020315/FIGURES/12/MEDIUM.

[123] M. Forsch, R. Stockill, A. Wallucks, I. Marinković, C. Gärtner, R.A. Norte, F. van Otten, A. Fiore, K. Srinivasan, S. Gröblacher, Microwave-to-optics conversion using a mechanical oscillator in its quantum ground state, Nature Physics 2019 16:1 16 (2019) 69–74. https://doi.org/10.1038/s41567-019-0673-7.

[124] W. Fu, M. Xu, X. Liu, C.L. Zou, C. Zhong, X. Han, M. Shen, Y. Xu, R. Cheng, S. Wang, L. Jiang, H.X. Tang, Cavity electro-optic circuit for microwave-to-optical conversion in the quantum ground state, Phys Rev A (Coll Park) 103 (2021) 053504. https://doi.org/10.1103/PHYSREVA.103.053504/SM.PDF.

[125] R. Stockill, M. Forsch, F. Hijazi, G. Beaudoin, K. Pantzas, I. Sagnes, R. Braive, S. Gröblacher, Ultra-low-noise microwave to optics conversion in gallium phosphide, Nature Communications 2022 13:1 13 (2022) 1–12. https://doi.org/10.1038/s41467-022-34338-x.

[126] D. Najer, I. Söllner, P. Sekatski, V. Dolique, M.C. Löbl, D. Riedel, R. Schott, S. Starosielec, S.R. Valentin, A.D. Wieck, N. Sangouard, A. Ludwig, R.J. Warburton, A gated quantum dot strongly coupled to an optical microcavity, Nature 2019 575:7784 575 (2019) 622–627. https://doi.org/10.1038/s41586-019-1709-y.

[127] Y. Chu, P. Kharel, T. Yoon, L. Frunzio, P.T. Rakich, R.J. Schoelkopf, Creation and control of multi-phonon Fock states in a bulk acoustic-wave resonator, Nature 2018 563:7733 563 (2018) 666–670. https://doi.org/10.1038/s41586-018-0717-7.

[128] S. Ghaffari, S.A. Chandorkar, S. Wang, E.J. Ng, C.H. Ahn, V. Hong, Y. Yang, T.W. Kenny, Quantum Limit of Quality Factor in Silicon Micro and Nano Mechanical Resonators, Scientific Reports 2013 3:1 3 (2013) 1–7. https://doi.org/10.1038/srep03244.

[129] J. Hasson, A. Many, Observation of Akhiezer and Landau-Rumer Regimes in the Frequency Dependence of Shear-Wave Lattice Attenuation in CdS, Phys Rev Lett 35 (1975) 792. https://doi.org/10.1103/PhysRevLett.35.792.

[130] B. Hamelin, J. Yang, A. Daruwalla, H. Wen, F. Ayazi, Monocrystalline Silicon Carbide Disk Resonators on Phononic Crystals with Ultra-Low Dissipation Bulk Acoustic Wave Modes, Scientific Reports 2019 9:1 9 (2019) 1–8. https://doi.org/10.1038/s41598-019-54278-9.

[131] D.O. Bracher, X. Zhang, E.L. Hu, Selective Purcell enhancement of two closely linked zero-phonon transitions of a silicon carbide color center, Proc Natl Acad Sci U S A 114 (2017) 4060–4065. https://doi.org/10.1073/PNAS.1704219114/ASSET/23BBF33B-E5B8-4FAA-A47A-920E522F2E0E/ASSETS/GRAPHIC/PNAS.1704219114FIG05.JPEG.

[132] B.S. Song, S. Jeon, H. Kim, D.D. Kang, T. Asano, S. Noda, High-Q-factor nanobeam photonic crystal cavities in bulk silicon carbide, Appl Phys Lett 113 (2018). https://doi.org/10.1063/1.5058194/36377.

[133] D.M. Lukin, M.A. Guidry, J. Vučković, Integrated Quantum Photonics with Silicon Carbide: Challenges and Prospects, PRX Quantum 1 (2020) 020102. https://doi.org/10.1103/PRXQUANTUM.1.020102/FIGURES/6/MEDIUM.

[134] P. Kharel, Y. Chu, M. Power, W.H. Renninger, R.J. Schoelkopf, P.T. Rakich, Ultra-high-Q phononic resonators on-chip at cryogenic temperatures, APL Photonics 3 (2018). https://doi.org/10.1063/1.5026798/14568230/066101_1_ACCEPTED_MANUSCRIPT.PDF.

[135] Comsol multiphysicstle, (n.d.). www.comsol.com.

[136] W. Nagourney, Quantum Electronics for Atomic Physics and Telecommunication, Quantum Electronics for Atomic Physics and Telecommunication (2014). https://doi.org/10.1093/ACPROF:OSO/9780199665488.001.0001.

[137] Layertech, (n.d.). https://www.layertec.de/en/.

[138] C. Koks, M.P. van Exter, Microcavity resonance condition, quality factor, and mode volume are determined by different penetration depths, Opt Express 29 (2021) 6879. https://doi.org/10.1364/OE.412346.

[139] C. P. Anderson, Spin Qubits in Silicon Carbide Electronic Devices, University of Chicago, 2020.

[140] M. Bockstedte, F. Schütz, T. Garratt, V. Ivády, A. Gali, Ab initio description of highly correlated states in defects for realizing quantum bits, Npj Quantum Materials 2018 3:1 3 (2018) 1–6. https://doi.org/10.1038/s41535-018-0103-6.

[141] J. F. Nye, Physical Properties of Crystals, Oxford University Press, 1986.

[142] Yeghishe Tsaturyan, Ultracoherent soft-clamped mechanical resonators for quantum cavity optomechanics, University of Copenhagen, 2019.

[143] C.B. Møller, Quantum Back-Action Evasion in a Hybrid Spin-Optomechanical System, University of Copenhagen, 2018.

[144] L. Thomas, G.N. Aliev, P.A. Snow, Hypersonic rugate filters based on porous silicon, Appl Phys Lett 97 (2010). https://doi.org/10.1063/1.3506582/121382.

[145] D. Schneider, F. Liaqat, E.H. El Boudouti, Y. El Hassouani, B. Djafari-Rouhani, W. Tremel, H.J. Butt, G. Fytas, Engineering the hypersonic phononic band gap of hybrid Bragg stacks, Nano Lett 12 (2012) 3101–3108. https://doi.org/10.1021/NL300982D.

[146] S.K. Son, S. Han, S.I. Chu, Floquet formulation for the investigation of multiphoton quantum interference in a superconducting qubit driven by a strong ac field, Phys Rev A 79 (2009) 032301. https://doi.org/10.1103/PHYSREVA.79.032301/FIGURES/7/THUMBNAIL.

[147] K.I. Seetharam, Thermalization in Periodically-Driven Interacting Quantum Systems, California Institute of Technology, 2018.

[148] MPh, (n.d.). https://pypi.org/project/MPh/.

[149] D.M. Lukin, C. Dory, M.A. Guidry, K.Y. Yang, S.D. Mishra, R. Trivedi, M. Radulaski, S. Sun, D. Vercruysse, G.H. Ahn, J. Vučković, 4H-silicon-carbide-on-insulator for integrated quantum and nonlinear photonics, Nature Photonics 2019 14:5 14 (2019) 330–334. https://doi.org/10.1038/s41566-019-0556-6.